Multispectral Imaging of Meat Quality - Color and Texture

Trinderup, Camilla Himmelstrup

Publication date:
2015

Document Version
Publisher's PDF, also known as Version of record

Multispectral Imaging of Meat Quality - Color and Texture

Camilla Himmelstrup Trinderup

Kongens Lyngby 2014
PHD-2014-358

Technical University of Denmark
Department of Applied Mathematics and Computer Science
Richard Petersens Plads, building 324,
2800 Kongens Lyngby, Denmark
Phone +45 4525 3351
compute@compute.dtu.dk
www.compute.dtu.dk PHD-2014-358

Summary (English)

The use of computer vision systems in food production and development is increasing. Computer vision systems offer fast, reliable, objective and non-invasive methods for assessment of wanted quality traits.

This thesis investigates the applicability of computer vision systems in the assessment of meat quality parameters, especially with regards to meat color and texture. Several image modalities have been applied, all considering multi- or hyper spectral imaging.

The work demonstrates the use of computer vision systems for meat color measurements. The color is assessed by suitable transformations to the CIELAB color space, the common color space within food science. The results show that meat color assessment with a multispectral imaging is a great alternative to the traditional colorimeter, i.e. the vision system meets some of the limitations that the colorimeter possesses. To mention one, it is possible to assess color of very complicated structures, such as salamis, with a vision system. More importantly though, the vision system embraces the complicated scattering properties of meat.

The images can also lead to other analyses, e.g. image texture analysis relating to the structure of the meat. In the thesis it is presented how simple texture measures can be used for characterizing the texture changes in fermented salamis. Moreover, it was investigated if it was possible to relate structure in images to chemical compounds in lard from boars.

Summary (Danish)

Brugen af visionsystemer i fødevareproduktion og -udvikling bliver mere og mere udbredt. Disse systemer tilbyder hurtig og objektiv måling af flere parametre inden for fødevarekvalitet. Vigtigst af alt, så er visionsystemer en metode, som ikke inficerer eller ændrer på produktet ved evaluering.

Denne afhandling undersøger mulighederne for brug af visionsystemer til vurdering af kvalitetsparametre inden for kødproduktion- og udvikling, særligt med henblik på evaluering af kødfarve og -tekstur. Både et RGB, et multispektralt og et hyperspektralt visionsystem har været brugt i studierne.

Studierne viser brugen af computer visionsystemer til kødfarvemålinger ved en passende transformation af de multispektrale billeder til CIELAB farverummet - det meget udbredte farverum benyttet i fødevareforskning. Resultaterne viste, at det multispektrale visionsystem er et godt alternativ til det traditionelle colorimeter, da visionsystemet ikke besidder de samme begrænsninger som colorimeteret. For bare at nævne én, så er visionsystemet i stand til at måle farve af selv meget komplekst sammensatte produkter, som f.eks. salami. Dog er den vigtigste fordel ved visionsystemet, at det automatisk tager højde for den komplicerede struktur i kød og dets deraf varierende spredningsegenskaber.

Billeder kan også lede til andre analyser end bare farve. F.eks. kunne det være en analyse af billedteksturer. I afhandlingen vises det, hvordan strukturændringen i fermenteringsprocessen af spegepølser kan blive beskrevet ved et simpelt teksturmål. Derudover er det også blevet undersøgt, om det var muligt at relatere strukturændringer til de kemiske stoffer, som giver anledning til fænomenet ornelugt.

Preface

This thesis was prepared at the Image Analysis and Computer Graphics Section at Department of Applied Mathematics and Computer Science at the Technical University of Denmark (DTU). It was done in fulfillment of the requirements for obtaining a *doctor of philosophy* degree (PhD) within the topic of image analysis.

The work presented in the thesis was financed by the Centre for Imaging Food Quality, a project funded by the Danish Council for Strategic Research (contract no. 09-067039) within the Programme Commission on Health, Food and Welfare.

The thesis presents research on the issue of using image analysis for meat quality assessment, mainly concerning color and texture. The first part of the thesis presents the theoretical background for meat quality and the applied instruments and methodologies. Hereafter the major findings are put into context of the methodologies presented, and the thesis is concluded on the basis of this. Following the conclusion are six manuscripts that were prepared during the course of the PhD study.

The project has been supervised by Professor Knut Conradsen and co-supervised by Associate Professor Anders Bjorholm Dahl. The research has been carried out at DTU, but with collaborative work with the Danish Meat Research Institute and Dupont Nutritional Biosciences. Moreover, the external research was conducted under supervision of Dr. Brad Kim at Department of Animal Sciences at Purdue University.

Lyngby, 23-December-2014

Camilla Himmelstrup Trinderup

Acknowledgements

First of all I would like to thank my supervisors, Knut Conradsen and Anders Bjorholm Dahl, for their motivational and encouraging support throughout the project – both professionally and personally. Moreover, thanks also goes to Brad Kim at Purdue University at the people of the Meatlab for hosting me in the Indiana winter – it made the stay a little warmer to feel welcome.

My collaborators at the Danish Meat Research Institute, Kirsten Jensen, Lene Meinert, Susanne Støier, and Claus Borggard, and Flemming Møller at Dupont. Thank you for providing the experimental basis for the studies in this thesis.

Aknowledgements also goes to my former and current colleagues at the Image Analysis and computer Graphics section. Especially Jacob Lerche Skytte and Otto H. Atterman Abildgaard for collaboration within the CIFQ group and for ad hoc discussions in the office. Also thanks to Jannik Boll Nielsen for feedback on the thesis. A special thanks to Hildur Einarsdottir for professional feedback and girly gossip.

Finally I would like to thank my friends and family for being supportive, even though you do not always understand my problems. Finally a great appreciation to Frede for always being there - supportive, patient, and understanding.

Contributions

Papers included in this thesis

Paper A
Camilla H. Trinderup, Anders Bjorholm Dahl, Kirsten Jensen, Jens Michael Carstensen, Knut Conradsen. Comparison of a multispectral vision system and a colorimeter for the assessment of meat color, *Meat Science*, 102(0): 1-7, 2015.

Paper B
Camilla H. Trinderup, Anders Bjorholm Dahl, Jens Michael Carstensen, Kirsten Jensen, Knut Conradsen. Utilization of Multispectral Images for Meat Color Measurements. *Workshop on Farm Animal and Food Quality Imaging*, Helsinki, June 2013.

Paper C
Camilla H. Trinderup, Yuan Brad Kim. Fresh meat color evaluation using a structured light imaging system, *Food Research International*, 71: 100-107, 2015.

Paper D
Camilla H. Trinderup, Anders B. Dahl, Flemming Møller, Knut Conradsen. Longitudinal Studies of Multispectral Images of Salami, *under submission*, 2015.

Paper E
Camilla H. Trinderup, Anders Bjorholm Dahl, Knut Conradsen. *Identifying boar taint with a hyper spectral imaging system*, *Technical report*, 2014. **Paper**

F
Anders B. Dahl, Camilla H. Trinderup, Rasmus Larsen, Knut Conradsen. Food Quality Assessment from Multi-scale Structured Light. *Technical report*, 2014.

Papers and abstract not included in this thesis

Camilla H. Trinderup, Anders Bjorholm Dahl, Kirsten Jensen, Jens Michael Carstensen, Knut Conradsen. A Comparison of Meat Color Measurements From a Colorimeter and Multispectral Images, in *Proceedings of the 16th International Conference on Near Infrared Spectroscopy 2013*, volume 1.

Camilla H. Trinderup, Yuan H. B. Kim. Meat Color Assessment Through a Structured Light Imaging System. Extended abstract at *AMSA Reciprocal Conference*, 2014.

Camilla H. Trinderup, Knut Conradsen, Anders Bjorholm Dahl. SLS characterization of pig lard. Extended abstract and poster at *Farm Animal Imaging conference I*, 2012.

Contents

Chapter 1

Introduction

The work presented in this thesis is a project within the Center for Imaging Food Quality (CIFQ), a center financed by the Danish Council for Strategic Research (contract no 09-067039). The activities within the center aim at assessing food quality parameters by non-invasive and contact-free methods. There are two focus points within these activities; to develop new computer vision based measurement systems and to show the applicability of the systems in food production and development.

The aspect of system development within the center is facilitated by the industrial partners, Videometer A/S and NKT Photonics A/S, whereas the primary food subjects of interest, dairy and meat, are enabled by the partners Arla Foods Amba, Danish Meat Research Institute (DMRI) and Dupont Nutritional Biosciences (formerly known as Danisco A/S). This has set the scope of the work presented in this thesis.

The term food quality covers any aspect of wanted quality traits in food products. These traits can relate to visual parameters such as size, shape, color, and texture, but to a large degree also organoleptic parameters involving flavor and taste. For research purposes, product development, and in some cases also production control, these factors are often assessed by a sensory panel, and despite training of the panel it will still to some degree be a subjective assessment. Therefore it would be extremely useful to have an objective reference method

related to the sensory panel assessment. This could e.g. be a mechanical measure of texture or a chemical analysis for investigating amounts of constituents. Unfortunately, these reference methods are often invasive, slow and can not be performed in-line or on-line during production. Computer vision systems employing suitable image modalities can aid in the process of monitoring production or product development offering fast, non-contact methods for assessing visual, and to some degree chemical, factors.

Within the setting of CIFQ this project aims at measuring meat quality parameters with computer vision systems with different modalities. Meat is a big part of the human nutrition as a great source for proteins. It is also a big industry, e.g. in Denmark 20% of the export income in 2011 derived from food and agricultural products (Landbrug & Fødevarer, 2012). For fresh and processed meat products consumer acceptance is to a large degree determined by the visual quality parameters such as color, freshness, and texture (MacDougall and Hutchings, 2002), since these factors relate to the freshness, flavor and mouthfeel.

In the assessment of meat color an ongoing issue is the traditional instrumental method by a colorimeter (Yagiz et al., 2009; Girolami et al., 2013). The colorimeter only assess meat color in spots across a sample (León et al., 2006), and this can lead to biased results when averaging over spots as a final sample measurement. Moreover, studies have shown that the colorimeter returns colors that do not correlate well with visual perception (Yagiz et al., 2009; Girolami et al., 2013). Applying a computer vision system is one approach for overcoming the limitations of the colorimeter (León et al., 2006; Mendoza et al., 2006; O'Sullivan et al., 2003).

Color measurements by a colorimeter are also difficult when the samples of interest have complex structures. This is for example the case for fermented salamis, where it is impossible to avoid fat parts when the colorimeter is applied for assessment of red meat color. The field of view or aperture size of the colorimeter will not be able to exclude fat. However, in images individual pixels can be classified as e.g. meat or fat and hereby a reliable color measurement of only lean meat can be computed.

Color measurements are important for the purpose of monitoring the fermentation process in an objective manner. As argued above a vision system can help in assessing color of complex structured samples, such as salamis where fat and meat have a close relation. Moreover, this structure can also be described by image texture features, and hence be related to the physical and visual interpretation of the structures in the process of following the fermentation process.

A problem relating to flavor quality of pork is the concept of boar taint. For

non-castrated pigs mainly two chemical compounds, skatole and androstenone, are developed and stored in the meat and lard. When the meat is heated these substances can lead to an unpleasant smell. Androstenone is a hormone, also called a testicular steroid, that develops as the male pig reaches sexual maturity. Skatole is a byproduct of an intestinal bacteria. Partners within the European Union have committed to plan to voluntarily end surgical castration of piglets towards 2018 (European commission, 2011). This rises a need for assessment of the level of skatole and androstenone. Zammerini et al. (2012) describes how alterations of the boars feed can lead to less bad smell. Other studies (Aluwé et al., 2009; Hansen et al., 2006a) have had the same focus and showing the same tendency. But the solution to the problem is not solved only by means of changing the diet of the pigs, and it will therefore be advantageous to have an in-line instrument in the slaughterhouse that can determine the level of chemical compounds. The determination of the chemical constituents have previously been addressed by multi- and hyper spectral imaging within research areas such as pharmaceutical investigations (Gowen et al., 2008), identification of ingredients in powders(Ma and Anderson, 2008), and soil constituents (Adams et al., 1986; Ben-Dor et al., 2009). The different compounds are identified by their absorption and scattering properties, and likewise it would be beneficial to have an instrument that could be able to assess skatole and androstenone levels.

The empirical work in this thesis has been carried out in collaboration with the Danish Meat Research Institute and Dupont Nutritional Sciences. The Meatlab at Purdue University, Indiana, USA, has played a great part as well.

1.1 Laboratory Work

The results of the work presented in this thesis have been obtained on the basis of a great amount of experimental and laboratory work. As a data analyst it is important to be part of an experiment all the way from preparation of samples to the final data analysis. This way an increasing insight on the factors influencing the final results is obtained, which is of great importance when the statistical analysis should be carried out. In the sequel a short outline of the laboratory work done in this project is given.

The subject of instrumental assessment of meat color has been investigated throughout the thesis. Paper A, B, and C concerns the color of fresh meat, whereas Paper D involves the color of fermented sausages. The laboratory work for obtaining the dataset used in Papers A and B involved sample preparations and image acquisition. One of the important observations during the laboratory work was the need for removing condensation from the meat surfaces to avoid

specular reflections.

In Paper C the laboratory work not only involved the muscle samples for that specific study, since the muscle samples were also used in investigation of pH development during aging and protein denaturation. Since the experimental work was on-going for a month, it was hence necessary to consider an optimal workflow ensuring systematical and reproducible results. The images in Figure 1.1 show some of the laboratory work performed.

Figure 1.1: Meat samples before cut-outs for the experiments. From left to right: *Semimembranosus*, *Psoas major*, and *Longissimus dorsi*. In the right image a pH measurements is performed.

The laboratory work of Paper D involved image acquisition, but also participation in the simultaneous sensory panel judgements. This resulted in an understanding of the interaction of physical parameters and the sensory panel's work. The Paper F describes the theoretical part of a structured light imaging system. The implementation and initial tests of the system was also performed as a part of the experimental work.

1.2 Objectives

The main objective of this thesis is to investigate the applicability of computer vision systems and image analysis in the assessment of meat quality parameters. The focus is on color and texture, but the study also presents an explorative analysis related to the issue of boar taint where we try to relate the chemical compounds to image features.

In the context of color the studies wish to investigate the advantages of a computer vision system and image analysis, and how these can contribute to product development and research within meat color. Regarding texture, it is the goal to apply existing image texture approaches to classify the texture of meat products such as salami.

1.3 Thesis Overview

The thesis consists of two parts and appendices presenting the contributions, i.e. the papers and reports representing the findings in the thesis. The first part presents methodology and theory about visual quality parameters of meat, vision systems, image analysis tools, and statistical methods and approaches. This part is meant as an overview of the basics behind the work presented in the contributions. The second part presents how the image analysis tools and statistical methods have been applied in the contributions by focusing on color and texture assessment by image analysis. The second part should be seen as the link between the methodology part and the appendices including the contributions (Part III). The thesis is concluded before the contributions are appended. The contributions are appended in their current layout.

Part I

Methodology

Chapter 2

Visual Meat Quality Parameters

This section will cover the basic theory behind the visual appearance of meat. At first a small introduction to the chemical constituents responsible for meat color is given, along with a description of the reflectance properties for fresh meat. Secondly the concept of boar taint is described briefly.

2.1 Color and Chemical Reactions

Color is an important quality parameter for meat products and it is therefore of critical importance to be able to assess meat color in a consistent, non-invasive and objective manner (MacDougall and Hutchings, 2002). This section gives a short introduction to the chemical and physical reasons for meat color.

Several factors can influence the appearance of the final meat product, and hereby how a customer will appreciate the product. These factors include species and breed dependencies, the pre-slaughter handling of the animals, and the handling of the animal post-mortem (Lawrie, 1998).

The dominant pigment responsible for red color in meat is myoglobin, and the

amount and state of this compound determines the color of a given product (Lawrie, 1998). Myoglobin itself is purplish-red, whereas its oxidized state, oxymyoglobin, is bright red, and the even more oxidized state, metmyoglobin, is brown. These are just the three basic stages of myoglobin. An example where myoglobin shows it stages is at opening of vacuum packaged products. At the time of opening the meat appears dull, but after oxygen exposure from the surrounding air, the myoglobin present at the surface of the product will react, and the meat will bloom, as oxymyglobin is formed. The oxymyglobin is desirable, since it reflects the desired color of products for the consumers (LYNCH et al., 1986). Exposing the meat surfaces to more oxygen will over time result in the formation of metmyoglobin and the meat sample will turn brown and discolored. This is often seen in the counter in supermarkets, where products in oxygen permeable packagings at first will be bright red and then at later display days turn brown. The discoloration rate is though dependent on different muscle types' inherited color stability (Kim et al., 2009).

Since color depends on a lot of factors, both before and after slaughter, it can be used as an important predictor in many research settings as well as production. It is therefore important to be able to assess color in a consistent and objective manner.

2.1.1 Absorption and Scattering in Meat

As described above the color of meat is dependent on the amount of myoglobin and its oxidative states, since it will determine the absorption and scattering properties of the meat. Myoglobin absorbs rays at wavelengths corresponding to green light (around 510 nm), and the light reflected from a meat sample will range from yellow to red, and sometimes purple (Swatland, 2004). Meat is a biological material and therefore have properties as a diffuse or translucent medium (Martelli, 2010). In a diffuse medium light will be scattered multiple times before being detected by e.g. a camera or another sensor. The multiple scattering events occur due to meats' varying refraction indexes (Swatland, 2002). The microstructures of meat consists of both air, liquids, and granules, which gives rise to different refractive indexes through the material (Girolami et al., 2013; Swatland, 2004).

Meat color appearance is dependent on the complex microstructure and the oxidative states of myoglobin. Oxymyoglobin is only present at the very surface ($\sim$ 5 mm) of the meat. Underneath the surface less oxygen is present and it will be brown metmyoglobin, and even further down myoglobin itself will be present (Girolami et al., 2013). Light can scatter deep into the sample it will penetrate through more than the first millimeters of the sample, and the refracted and

reflected light from the lower layers will contribute to the meat color with brown and purple red.

Finally, the visual color impression of a meat sample is also strongly dependent on the illumination. Often the standard illuminant D65 is used in meat color measurements since it resembles daylight well. The A illuminant can also be used – it highlights the redness of the samples (Yancey and Kropf, 2008).

The complex microstructure and varying contributors to meat color makes it a difficult task to measure or assess color in a consistent manner that still reflects human perception of color. The traditional way of assessing color is by a colorimeter, but this instrument has limitations e.g. regarding assessment of the entire surface of a sample (Girolami et al., 2013; Brosnan and Sun, 2004; Lasarte et al., 2006; Yagiz et al., 2009; León et al., 2006). A great part of the limitations and disadvantages of the colorimeter can be met by a computer vision system. But in order to apply the vision systems correctly it is of great importance to take the spectral properties of meat into consideration.

2.2 Boar Taint

Boar taint is caused by certain chemical compounds and it especially arises when meat products are heated. The chemical compounds causing the issue are skatole and androstenone (Banon et al., 2003). Boar taint mainly arises in non-castrated male pigs (boars) - as the name also suggests. Skatole and androstenone will always be present in the pigs, but in much higher amounts for non-castrated male pigs. This rises an issue since the European Union by 2018 will strive to end surgical castration of piglets (European commission, 2011). It is to some extent possible to influence the skatole and androstenone levels by feeding the animals certain diets (Aluwé et al., 2009; Hansen et al., 2006a), but the studies were not explicit, since not all boars reacted the same way to the modified diet. For the above reasons it will be beneficial to predict the skatole and androstenone level at the slaughterhouse by a non-invasive method. The conventional method for assessing the amounts of chemical compounds are by High-performance liquid chromatography (HPLC) (Garcia-Regueiro and Diaz, 1989).

The use of spectral measurements are widely applied within chemometrics, but currently no studies on the use of the method for measuring boar taint are to be found. The two chemical compounds, skatole and androstenone, are found in very small concentrations, and it can therefore be difficult to identify their presence among all other contents.

Chapter 3

Vision Systems

This section gives a short introductions to the vision systems employed in the papers included in the thesis. The image modalities range from RGB, to multi- and hyperspectral images.

3.1 Multispectral Vision System

The multispectral instrument applied is the commercially available VideometerLab. The system is illustrated in Figure 3.1. The instrument has 19-20 spectral bands dependent on the model, ranging from the nearly visible light at 375 nm up to a near infra red band at 970 nm. It has a light integrating sphere, where the LEDs providing the multispectral illumination are placed at the equator. The special coating inside the sphere results in a diffuse illumination of the sample of interest and specular reflectance is to a large degree avoided.

The resolution of the monochrome camera in the instrument is 2056×2056 pixels, which results in a pixel size of $\sim 45\mu$m. With this spatial resolution it is possible to detect even small differences by image analysis techniques.

The instrument has previously been applied in studies investigating issues re-

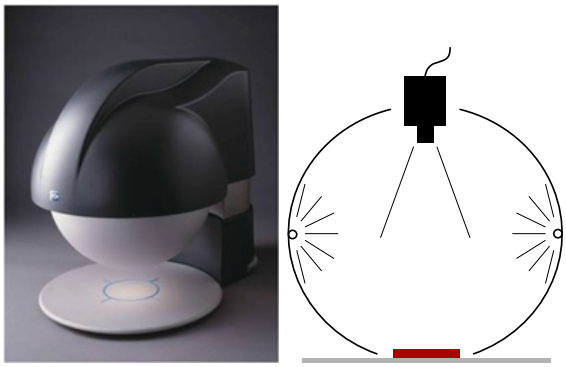

Figure 3.1: Left: The VideometerLab with light integrating sphere. Right: Cross sectional view of the integrating sphere.

garding seeds (Olesen et al., 2011), meat spoilage (Dissing et al., 2013), astaxantin detection in salmon (Ljungqvist et al., 2012) just to mention a few.

3.2 Structured Light System

The RGB vision system is based on structured light. This instrument is a prototype inspired by the work of Nayar et al. (2006). The instrument was developed with the goal of determining the direct and global reflectance of a translucent material. Only directly reflected light, i.e. light that has not been scattered, is contained in the direct component, whereas the rest is in the global component. As a result the global component includes subsurface scattered light, but it can also include light that has been reflected within the scene. Our scene is however a very controlled environment where we have designed the setup to avoid intra-reflections, and the global component will therefore be dominated by subsurface scattering. The structured light system contains an industrial JAI RGB camera and a pico projector from Texas Instruments, which is mounted in a diffuse black closure.

The method for separating the direct and global component of a scene is based on the additive nature of light, such that the total radiance at a camera pixel is a sum of two components, where the i'th pixel is given by adding the direct $L_s(i)$ and global $L_d(i)$ term:

$$L(i) = L_d(i) + L_s(i) \ . \tag{3.1}$$

Using structured light enables us to measure the global and direct components.

By illuminating the scene with a binary pattern, such as a checkerboard pattern, all the unlit checkers will have no direct illumination and therefore measure the global component. The lit checkers will contain both the direct and the global component. We denote the lit pixels as L^+ and the unlit pixels as L^-, and we assume that an unlit source pixel does not emit light. If the lit projector pixels makes up a fraction α of all the projector pixels we obtain these simple relations

$$L^+(i) = L_s(i) + \alpha L_d(i) \ , \tag{3.2}$$
$$L^-(i) = (1-\alpha)L_d(i) \ . \tag{3.3}$$

With only two checkerboard images all pixels can be both lit and unlit, which could make up the basis for separating the direct and global components. But due to edge effects this is not sufficient, so a sequence of images are acquired, each lit by a shifted binary pattern. Based on this it is possible to define

$$L^+(i) = L_{\max}(i) \ , \tag{3.4}$$
$$L^-(i) = L_{\min}(i) \ . \tag{3.5}$$

as the minimum and maximum values in each pixel across the sequence of images. The diffuse and specular components in each pixel i of the captured scene can then be found by

$$L_s(i) = L_{\max}(i) - (1-\alpha)L_d(i) \ , \tag{3.6}$$
$$L_d(i) = \frac{1}{1-\alpha} L_{\min}(i) \ . \tag{3.7}$$

When the system employs structured light in the form of checkerboard patterns, which makes the fraction of lit pixels $\alpha = 1/2$, the specular and diffuse component can be found by

$$L_s(i) = L_{\max} - \frac{1}{2} L_d(i) \ , \tag{3.8}$$
$$L_d(i) = 2L_{\min}(i) \ . \tag{3.9}$$

The above model is very simple and provides very good results by having a sufficient number of projections, and a relatively high pattern frequency in order to obtain a global image with sharp contrast.

In Figure 3.2 the prototype of the computer vision system is seen. An industrial camera from JAI with a resolution of 8M pixels is mounted at the same height as a Texas Instrument Pico projector. To ensure no influence from unknown light sources, the set-up is enclosed in a black box. The acquisition of the image sequence with shifted binary patterns is controlled by a computer.

Figure 3.3 shows a sequence of images lit by shifted checkerboard patterns used for separating the scene into its direct and global component. A second example

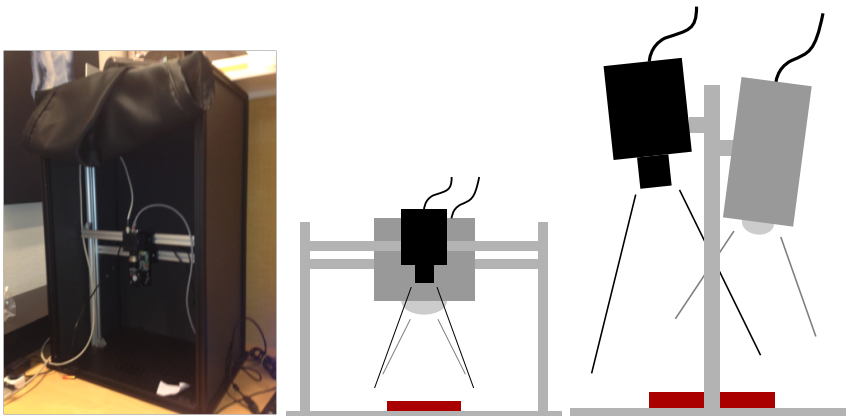

Figure 3.2: Left: Prototype of the structured light set-up. Middle and right: Illustrations of the structured light set-up with projector and camera seen from the front and the side.

with the resulting direct and global component of a hand and a carrot is seen in Figure 3.4.

Other methods for separating the diffuse and specular component of an object have been developed (Tariq et al., 2006; Artusi et al., 2011). They often employ polarization filters to the camera lens. This means that the hardware handles the separation and the systems are therefore less flexible than the approach presented here.

3.2.1 Instrument Development

The structured light system described in this section is a prototype developed within this PhD project. The process of developing a prototype contains several steps starting with a clarification of the system needs with regards to the software (Liou, 2007). After the identification and implementation of the software needs, it was also necessary to consider how the hardware should accompany the software. It was important that the system was flexible and capable of handling objects of different sizes. By mounting the camera and the projector on a rail system it was possible to adjust the distance between the camera, projector and the samples. The rail system was mounted on a heavy metal plate, and surrounded by a black enclosure to avoid illumination from unknown sources.

So far the system employs an RGB camera which gives some limitations. A fur-

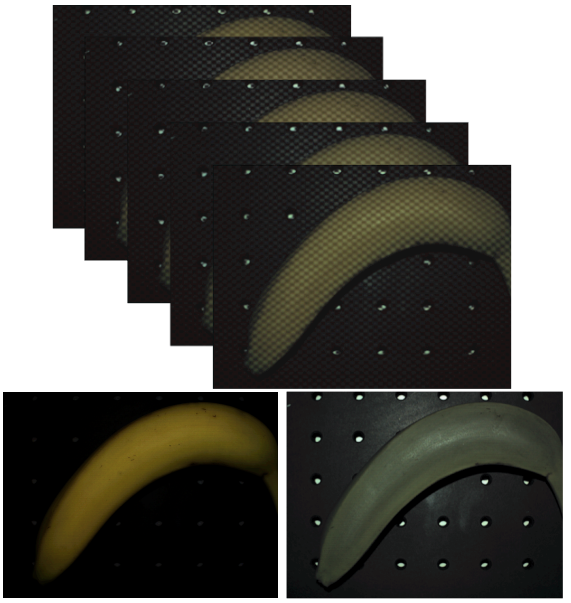

Figure 3.3: Top images: Checkerboard projection. Bottom-left: Diffuse component. Bottom-right: Specular component. The 'dots' in the background are holes in the aluminum plate that the system is mounted on.

ther development of the system could be an extension making it multispectral by illumination from LEDs at specific bandwidths. That would make it possible to extract the diffuse component at different wavelengths, and possibly contribute to a data set with more possibilities. A system like this would differentiate itself from commercialized multispectral systems, e.g. the VideometerLab described above, by its ability to capture both the specular and diffuse component. The VideometerLab ensures diffuse lighting inside the integrating sphere, but this means that distinct specular properties of a material may not be captured.

3.3 Hyperspectral Static Light Scattering System

The hyperspectral imaging system applied is denoted static light scattering (SLS) system. The system set-up is illustrated in Figure 3.5. It shows how a broadband light source with an acousto optical tunable filter (AOTF) shines onto the sample at an oblique incident angle. The diffuse reflectance is captured by a camera mounted vertically above the incident point of the laser. The sys-

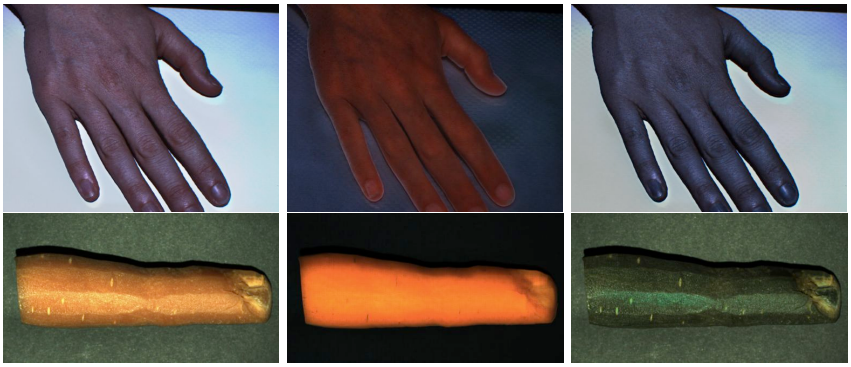

Figure 3.4: Total image, diffuse and specular component of a hand and a carrot.

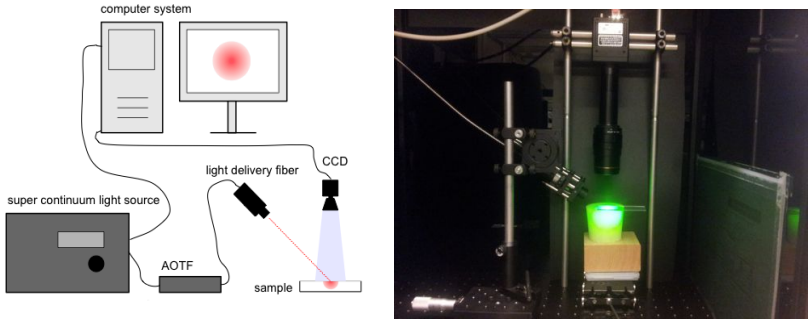

Figure 3.5: Illustration of the SLS system.

tem details are described further by Nielsen (2014) and Skytte et al. (2012). The advantage gained by using hyper spectral imaging, is that the reflectance can be related to both the chemical compounds of the sample under investigation, but also the micro-texture due to absorption and scattering properties of the material. The spectral range of the system is 440 nm to 990 nm with 10 nm intervals, which gives 56 spectral bands. In Figure 3.6 an example of the data obtained at the 650 nm spectral band is shown. For illustration, the image show the logarithm of the original data intensities.

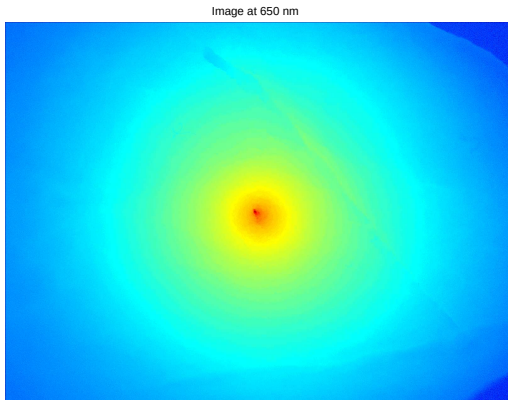

Figure 3.6: Example of image data at 650 nm. This is an image of lard from a boar. Image intensities are mapped to the logarithmic scale.

Chapter 4

Image Analysis

This chapter introduces the image analysis methods applied in the contributions in Part III. The concept of color transformations is introduced in relation to assessing color from both RGB and multispectral images. Several statistical methods are described since they are important in segmentation and classification tasks, but also in the analysis of features extracted from the images. Finally, two methods for characterizing image textures are introduced.

4.1 Color Transformations

As described earlier, color is one of the visual factors influencing the consumers' willingness to buy (MacDougall and Hutchings, 2002). Relating this to research and product development, makes it crucial to be able to assess color in an objective and consistent manner. Vision systems are capable of capturing color of products, but a preprocessing of the image data must happen in order to reach something valuable for the food scientist.

This section will present the general idea of mapping pixel data to a predefined color space. The transformation of image data to other color spaces have been investigated a lot through time (Hardeberg, 2001; Lasarte et al., 2006; Finlayson

and Drew, 1997; Valous et al., 2009).

The CIE XYZ color space, defined by the International Commission on Illumination (CIE), is a tristimulus color description. Tristimulus color values have three parameters stimulating the three cones in the eye and their sensitivities, and in this way the CIEXYZ color space covers all colors that the human eye can sense. Figure 4.1(a) shows how each of the X, Y, and Z, components are defined with respect to wavelength. The tristimulus values depend on the illuminant, and two examples of different illuminations are seen in Figure 4.1(b). Illuminant A represents typical domestic lightning, and illuminant D65 is standard daylight. The CIE XYZ curves under a specific illuminant are denoted *color matching functions* (CMF), and in Figures 4.1(c) and 4.1(d), these functions are plotted for the A and D65 illuminant (ISO 11664 - 1, 2007; ISO 11664 - 2, 1976).

Several color spaces are formulated in terms of the tristimulus CIE XYZ color space, and it is therefore advantageous to transform the color from an image to this space. A common color space used in food science is the CIELAB space due to its correlation with human color perception. The CIELAB color components, L^*, a^*, and b^*, are formulated in terms of the CIEXYZ space. The three components of the color space are defined as:

$$\begin{aligned} L^* &= 116 f(Y/Y_n) - 16 \\ a^* &= 500\left[f(X/X_n) - f(Y/Y_n)\right] \\ b^* &= 200\left[f(Y/Y_n) - f(Z/Z_n)\right], \end{aligned} \tag{4.1}$$

with

$$f(t) = \begin{cases} t^{1/3} & \text{if } t > (\frac{6}{29})^3 \\ \frac{1}{3}\left(\frac{29}{6}\right)^2 t + \frac{4}{29} & \text{otherwise} \end{cases} \tag{4.2}$$

and (X_n, Y_n, Z_n) is the reference white point dependent on illumination temperature. For illuminant D65 the reference white point is defined to be $(X_n, Y_n, Z_n) = (0.9504, 1.0000, 1.0889)$ (ISO/CIE Standard, 1976; ISO 11664 - 3, 1976).

Color difference of two CIELAB measurements is evaluated in terms of the ΔE^*_{ab} parameter, that expresses the total difference in color. It is defined as the Euclidean distance between two measurements (L^*_1, a^*_1, b^*_1) and (L^*_2, a^*_2, b^*_2) in the CIELAB space

$$\Delta E^*_{ab} = \sqrt{(L^*_2 - L^*_1)^2 + (a^*_2 - a^*_1)^2 + (b^*_2 - b^*_1)^2}. \tag{4.3}$$

When applying an RGB system the color outcome from the three channels are dependent on the device and the CCD sensitivity in the camera (Wu and

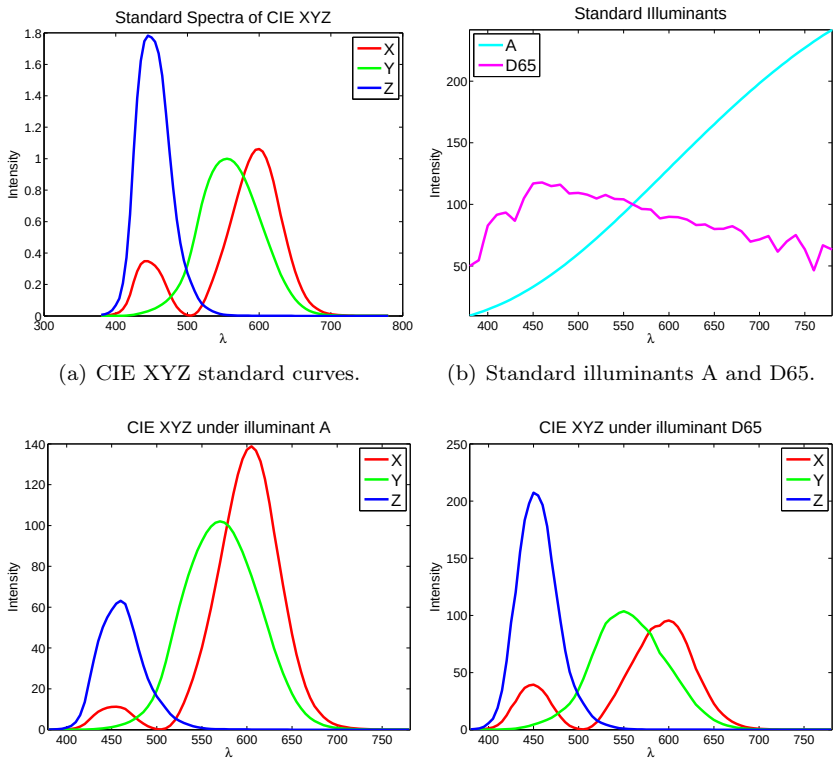

(a) CIE XYZ standard curves.

(b) Standard illuminants A and D65.

(c) CIE XYZ color matching functions under illuminant A.

(d) CIE XYZ color matching functions under illuminant D65.

Figure 4.1: Standard color curves, illuminants, and the resulting color matching functions under these illuminations.

Sun, 2013). Hence it is not always possible to compare the outcome from two RGB systems directly. In a lot of cases we don't know the specifications of the CCD and it is therefore necessary to resort to other ways for determining the relationship between the RGB outcome and the CIE XYZ color space. One way to do it, is by determining a suitable transformation, $\boldsymbol{W}_{\text{opt}}$, by solving a linear, constrained least squares problem of the form

$$\boldsymbol{W}_{\text{opt}} = \min_{\boldsymbol{W}} \|\boldsymbol{A} - \boldsymbol{B}\boldsymbol{W}\|_2^2. \tag{4.4}$$

Here we consider $\boldsymbol{A} \in \mathbb{R}^{m\times 3}$ to be m ground truth values in CIE XYZ coordinates and $\boldsymbol{B} \in \mathbb{R}^{m\times 3}$ to be the m RGB measurements of the ground truth values. The problem can be constrained by demanding equality for the i'th

observation, such that

$$\boldsymbol{A}_{[i]} = \boldsymbol{B}_{[i]}\boldsymbol{W}, \tag{4.5}$$

where $\boldsymbol{A}_{[i]}$ and $\boldsymbol{B}_{[i]}$ are the i'th row of the respective matrices. Often it will be beneficial to constrain the problem for the observations that are closest to white.

In praxis the m ground truth observations for solving the problem in (4.4) could be the 24 squares of a classic color checker. When the transformation $\boldsymbol{W}_{\text{opt}}$ has been established it is possible to convert the colors expressed in CIE XYZ colors to the CIELAB color space by the definitions in (4.1).

We also wish to be able to convert multispectral images to CIELAB values. In case the relative intensities and bandwidth of each illumination source is known, it is somehow easier to map the multispectral information to the color matching functions in Figure 4.1. The color matching functions are sampled equidistant from 400-700 nm in intervals of 5 nm, and collected in $\boldsymbol{A} \in \mathbb{R}^{m\times 3}$, with X, Y, and Z values in the columns. In the same way we can now define $\boldsymbol{B} \in \mathbb{R}^{m\times n}$ as the relative intensities of the n spectral bands on the same sampling grid. Each column of $\boldsymbol{B}$ holds the information about one spectral band. In the same way as above it is then possible to find the mapping between the multispectral information and the CIEXYZ color matching functions by solving a linear problem as in (4.4). Again (4.1) can be used for transformation to CIELAB values. Once the optimal transformation is established, the color checker can be used as a validation of the mapping by e.g. ΔE^*_{ab}. The presented approach is very general and can easily be adjusted to the illuminant dependent color matching functions.

4.2 Segmentation and Classification

Segmentation and classification are powerful tools within image analysis with a lot of application opportunities. In this section some of the traditional methods based on multivariate statistics will be presented, and the formulations of them are therefore quite general. The methods presented here primarily take pixel intensities as inputs and hence, they are supervised methods, i.e. based on training data. In image segmentation this can for example be visual selection of training areas for different classes. This section will give an overview of the segmentation and classification methods applied throughout this thesis.

4.2.1 Discriminant Analysis

The linear discriminant analysis (LDA) is a commonly used method in multivariate statistics. We wish to discriminate observations from k populations, π_1, π_2, ..., π_k based on knowledge about the first order statistics of each of the populations.

In the case of k populations we wish to establish what frequency function, $f_i(\boldsymbol{x})$ an observation, $\boldsymbol{x}$ with p variables belongs to. The prior probability for a population is given by

$$g(\pi_i) = p_i, \quad i = 1, \ldots, k. \tag{4.6}$$

We then define the discriminant score as

$$S_i(\boldsymbol{x}) = p_i f_i(\boldsymbol{x}). \tag{4.7}$$

The observation $\boldsymbol{x}$ belongs to the population, π_ν, resulting in the highest discriminant score, which can be stated as

$$S_\nu \geq S_i \quad \forall i. \tag{4.8}$$

In the case of k normally distributed populations, $\pi_i \sim \mathrm{N}_p(\boldsymbol{\mu}_i, \boldsymbol{\Sigma}_i)$ the frequency function f_i is known as

$$f_i(\boldsymbol{x}) = \frac{1}{\sqrt{2\pi}^p} \frac{1}{\sqrt{\det \boldsymbol{\Sigma}_i}} \exp\left(-\frac{1}{2}(\boldsymbol{x} - \boldsymbol{\mu}_i)' \boldsymbol{\Sigma}_i^{-1} (\boldsymbol{x} - \boldsymbol{\mu}_i)\right). \tag{4.9}$$

The discriminant score in (4.7) then becomes

$$S_i = -\frac{1}{2} \ln(\det \boldsymbol{\Sigma}_i) - \frac{1}{2}(\boldsymbol{x}' - \boldsymbol{\mu}_i)' \boldsymbol{\Sigma}_i^{-1} (\boldsymbol{x} - \boldsymbol{\mu}_i) + \ln p_i \tag{4.10}$$

and is called quadratic discrimination. In case the $\pi_i \sim \mathrm{N}_p(\boldsymbol{\mu}_i, \boldsymbol{\Sigma})$, i.e. all k populations have common variance-covariance matrix, the discriminant score reduces to

$$S_i = \boldsymbol{x}' \boldsymbol{\Sigma}_i^{-1} \boldsymbol{\mu}_i - \frac{1}{2} \boldsymbol{\mu}_i' \boldsymbol{\Sigma}^{-1} \boldsymbol{\mu}_i + \ln p_i \tag{4.11}$$

In order to apply this decision rule to an image, training areas from each population are defined, and estimates of the mean of each population $\hat{\boldsymbol{\mu}}_{\boldsymbol{i}}$ and the common covariance matrix $\hat{\boldsymbol{\Sigma}}$ is derived. For each pixel the discriminant scores for all possible populations are found, and it will be classified as belonging to the population with the highest discriminant score.

The review of the LDA is based on the terminology and notation presented by Johnson and Wichern (2002) and Ersbøll and Conradsen (2012).

4.2.2 Canonical Discriminant Analysis

Another statistical method applied for segmentation of images is the canonical discriminant analysis (CDA). This method maps the data to a space where the ratio between variance between groups and variance within groups is maximized.

As in the LDA case we consider k groups with observations within each group $\boldsymbol{X}_1, \ldots, \boldsymbol{X}_k$. Each group has n_i observations. $\bar{\boldsymbol{X}}_i$ defines the mean within each of the groups and $\bar{\boldsymbol{X}}$ the overall mean. We can then define the between and the within group variance-covariance matrices as

$$\boldsymbol{B} = \sum_{i=1}^{k} n_i \left(\bar{\boldsymbol{X}}_i - \bar{\boldsymbol{X}}\right)\left(\bar{\boldsymbol{X}}_i - \bar{\boldsymbol{X}}\right)' \tag{4.12}$$

$$\boldsymbol{W} = \sum_{i=1}^{k} \sum_{j=1}^{n_i} \left(\boldsymbol{X}_{ij} - \bar{\boldsymbol{X}}\right)\left(\boldsymbol{X}_{ij} - \bar{\boldsymbol{X}}\right)'. \tag{4.13}$$

To find the best discriminator function, $\boldsymbol{y} = \boldsymbol{d}'\boldsymbol{x}$, such that the ratio of the $\boldsymbol{d}^T\boldsymbol{B}\boldsymbol{d}$ and $\boldsymbol{d}^T\boldsymbol{W}\boldsymbol{d}$ is maximized, i.e. we can optimize the Rayleigh coefficient

$$\phi(\boldsymbol{d}) = \frac{\boldsymbol{d}^T\boldsymbol{B}\boldsymbol{d}}{\boldsymbol{d}^T\boldsymbol{W}\boldsymbol{d}}. \tag{4.14}$$

This optimization problem can be formulated as a generalized eigenvalue problem,

$$\det(\boldsymbol{B} - \lambda\boldsymbol{W}) = 0, \tag{4.15}$$

with largest eigenvalue, λ_1. The corresponding eigenvector, $\boldsymbol{d}_1$, maximizes the ratio in (4.14). Iterating further it is possible to find $k-1$ eigenvalues different from 0, and their corresponding eigenvectors, $\boldsymbol{d}_2, \boldsymbol{d}_3, \ldots, \boldsymbol{d}_{k-1}$, such that

$$\boldsymbol{d}_i^T\boldsymbol{W}\boldsymbol{d}_j = 0 \quad \forall i \neq j. \tag{4.16}$$

It is therefore possible to obtain $k-1$ discriminator functions.

A special case of the CDA is the so called normalized CDA (nCDA). As the name states, the canonical discriminant functions are normalized by subtracting the overall mean, $\boldsymbol{c}$, and dividing by the standard deviation, $\boldsymbol{s}$, of $\boldsymbol{y}$.

$$\bar{\boldsymbol{y}} = \frac{\boldsymbol{y} - \boldsymbol{c}}{\boldsymbol{s}}. \tag{4.17}$$

This has the advantage that the values of the discriminant function will be centered around zero. This makes it easy to set a threshold value for discrimination between populations.

When applying CDA for image segmentation, training areas representing the k groups are defined. From this information $\boldsymbol{B}$ and $\boldsymbol{W}$ are estimated and the problem in (4.15) can be solved. Hence the discriminant functions for each pixel value can be obtained, and a threshold can be set for pixel-wise classification.

The review of the CDA was based on the terminology presented by Johnson and Wichern (2002) and Ersbøll and Conradsen (2012).

Linear discriminant analysis (LDA) and canonical discriminant analysis, are classical statistical methods depending on a precise modeling of the random phenomena. In fact, when the problem only involves two classes the two methods, CDA and LDA, are equal. In the last decades these models have been supplemented by classification methods like support vector machines (determining separating hyperplanes) (Burges, 1998) or Random Forests (using decision trees) (Breiman, 2001; Hastie et al., 2009), just to mention a few. In the setting of this thesis it has been important to consider the covariant structures, for which the classical methods as e.g. CDA are well suited.

4.3 Texture

In the context of meat and meat products, we would normally think of texture as something we experience when we eat the product - is it chewy, tender, homogenous, etc. In image analysis texture is related to the visual appearance in two dimensions. In this setting texture can relate to surface roughness, smoothness, orientation, and similar characteristics (Haralick, 1979). Textures in images are often used for segmentation tasks (Belongie et al., 1998; Pal and Pal, 1993; Dahl and Larsen, 2011).

Two different texture characterization methods have been considered in this project. The first is build on gradients in an image, and based on simple filter operations. The idea was originally presented by (Dalal and Triggs, 2005) and is now often used in image recognition tasks. The method described in this section is based on the magnitude of the gradients in an image. The second texture measure is a characterization of speckle size. Speckle patterns arise when the surface imaged is rough at the scale of the wavelength of the illumination (Goodman, 1975). This leads to a granular-like pattern in the images that can be related to the physical properties of the material under investigation, and these speckle patterns can be characterized by e.g. the average speckle size.

4.3.1 Gradient Magnitude Histograms

The gradient of an image, f, is defined as

$$\nabla f = \frac{\partial f}{\partial x} e_x + \frac{\partial f}{\partial y} e_y, \tag{4.18}$$

where e_x and e_y are the unit vectors in the x and y directions respectively. The gradients can be approximated by simple filtering operations (Lowe, 2004). A convolution filter with the values $[-1, 0, 1]$ should be applied to both directions of the image, such that the gradient of an image, $\boldsymbol{I}$, in a point (x, y) is

$$\boldsymbol{I}'_x(x, y) = \boldsymbol{I}(x + 1, y) - \boldsymbol{I}(x - 1, y) \tag{4.19}$$

$$\boldsymbol{I}'_y(x, y) = \boldsymbol{I}(x, y + 1) - \boldsymbol{I}(x, y - 1). \tag{4.20}$$

This means that we use a central difference approach to find the approximate gradients (Elden et al., 2004). All the gradients in an image have an orientation, θ, and a magnitude, m, given by

$$\theta(x, y) = \arctan\left(\frac{f'_y(x, y))}{f'_x(x, y)}\right) \tag{4.21}$$

$$m(x, y) = \sqrt{f'^2_x(x, y) + f'^2_y(x, y)}. \tag{4.22}$$

In the originally presented work images are compared by collecting the gradient orientations for each image in a histogram, where each gradient orientation is weighted by its magnitude. Ensuring that the bins of the histograms are the same across images and performing a normalization of the histograms will results in a valid comparison basis (Ferman et al., 2002).

In the intended application of texture classification by gradients, the images are dominated by the same texture over time, but the change that do happen is a blurring of the lines between two groups in the images. This behavior means that the distribution of gradient magnitudes will change over time, and this quantity can therefore be used as a simple texture descriptor for identifying differences. If we on top of this consider the gradient magnitudes at different scales, we will be able to capture the total variation of the gradient magnitudes.

The gradient magnitudes are collected in histograms at each scale and these histograms are hereafter concatenated for all considered scales. In order to compare the histograms they are sampled with the same binning for all samples and afterwards normalized.

4.3.2 Speckle

The speckle characterization will be used on images from the 2D static light scattering (SLS) system described in Section 3.3. The speckle pattern arise due to the coherent light, when interferences between the light rays and the micro structures in the material occur. This means that different materials will results in different speckle patterns (Goodman, 1975). The method described below has previously been applied in the same image modality with acidified milk products as the subject of interest (Skytte, 2014; Sharifzadeh et al., 2013). In these studies it was shown that the speckle characterization is good at discriminating between milk and yoghurt with different amounts and sizes of fat particles.

The method for characterizing speckle is described by Skytte (2014), and is based on the theory by Goodman (1975) and Piederriere et al. (2004). The speckle of an SLS image, f, will be denoted, S_f. We wish to find the average speckle size in a center patch of $N \times N$ pixels, since this is where the speckle signal is the strongest. The first step in the procedure is a smoothing or local filter operation to extract the speckle pattern from the pure diffuse part of the reflectance. The speckle in a pixel (x, y) is hence obtained by

$$S_f = \frac{f(x,y) - m_f(x,y)}{\sigma_f(x,y)}, \tag{4.23}$$

where m_f and σ_f are the local mean and standard deviation respectively of a neighborhood of $n \times n$ pixels. From the images of speckle the average speckle size at each spectral band is found by considering the spatial autocorrelation function. For a single column or row in the speckle pattern, the average speckle size is defined as the full width at half maximum (FWHM) at lag 0. Figure 4.2 illustrates the approach. Averaging across all rows and columns will give the average speckle size. The method utilizes that the autocorrelation relates to the self similarity of local structures.

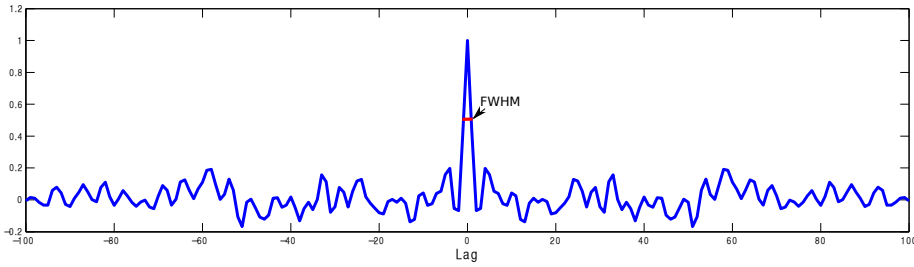

Figure 4.2: Autocorrelation function example. At lag 0 the average speckle size is found as the full width at half maximum (FWHM).

4.4 Fourier Transform

A classical method for investigating an image signal is by application of the Fourier transform. Extending the Fourier transform in (Easton, 2010) to two dimensions, and applying it to images will give knowledge about the spatial frequencies in the image. This will give the opportunity to identify periodicities and anisotropic behavior in the images. We will consider the two-dimensional discrete Fourier transform (DFT) defined as

$$F(u,v) = \frac{1}{MN} \sum_{m=0}^{M-1} \sum_{n=0}^{N-1} f(m,n) \exp\left(-i2\pi \left(\frac{mu}{M} + \frac{nv}{N}\right)\right), \tag{4.24}$$

for an image f of size $M \times N$ pixels (Hansen et al., 2006b). The magnitude of the DFT spectrum is given as the absolute value of the complex valued image.

4.5 Statistical Tools and Tests

Besides the LDA and CDA presented previously in this chapter, statistical tools such as principal component analysis and analysis of variance are widely used in the papers. This section will present the basics of these methods.

4.5.1 Principal Component Analysis

The principal component analysis (PCA) is a statistical tool that uses an orthogonal basis, $\boldsymbol{P}$, to produce linearly independent variables, called principal components from an original dataset $\boldsymbol{X}$. The basis is chosen such that the first principal component explains the most variability in the data.

The original dataset has n observations and p variables, such that $\boldsymbol{X} \in \mathbb{R}^{n \times p}$ with variance-covariance matrix $\boldsymbol{\Sigma}$. The eigenvectors of this matrix are given in descending order as

$$\lambda_1 \geq \lambda_2 \geq \cdots \geq \lambda_p,$$

and the corresponding eigenvectors are denoted $\boldsymbol{p}_i$, $(i = 1, \ldots, p)$. The orthogonal basis we use to map the original data to linear independent variables is defined as

$$\boldsymbol{P} = [\boldsymbol{p}_1, \ldots, \boldsymbol{p}_p] \quad (\boldsymbol{P} \in \mathbb{R}^{p \times p}). \tag{4.25}$$

The principal components, $\boldsymbol{Y} \in \mathbb{R}^{n \times p}$, are then given by

$$\boldsymbol{Y} = \boldsymbol{X}\boldsymbol{P}. \tag{4.26}$$

The PCA is a powerful tool for dimension reduction when the number of variables if larger than the number of observations, i.e. $p \gg n$. From the eigenvalues, λ_i, it is possible to find the fraction of variance explained by each of the principal components. This can help in selecting a suitable amount of dimensions. Moreover, each principal component often relates to a specific property of the original data, which is helpful in understanding and visualizing the original data. These interpretations can also be facilitated by using sparse principal components with e.g. application of the sparse PCA (Zou et al., 2006). We have, however, not found it necessary to pursue this line of thinking further.

The methodology used here is inspired by (Ersbøll and Conradsen, 2012).

4.5.2 Statistical Tests

In order to test for differences within groups or populations in an experiment it is beneficial to use the tools of univariate and multivariate *analysis of variance* (ANOVA and MANOVA). A standard problem in the univariate case is to test if there is difference in mean for two or more groups or populations. The observations, $X_i \sim N(\mu_i, \sigma^2)$, $i = 1, 2, \ldots, k$, are random samples from the k different populations, i.e. to test the hypothesis that the means are equal, $\mu_1 = \mu_2 = \ldots = \mu_k$, against all alternatives. In order to do so we define the individual means μ_i as

$$\mu_i = \mu + \tau_i \tag{4.27}$$

where μ is the overall mean and $\sum_i \tau_i = 0$. Hence the null-hypothesis can be reformulated as

$$H_0 : \tau_1 = \tau_2 = \ldots = \tau_k, \tag{4.28}$$

and the response variable can then be expressed as

$$X_{ij} = \mu + \tau_i + \varepsilon_{ij}. \tag{4.29}$$

When we wish to test the null-hypothesis we consider the sum of squares (SS) of the different effects, the residuals, and the total sum of squares given by

$$SS_{\text{effect}} = \sum_{i=1}^{k} n_i (\bar{x_i} - \bar{x})^2 \tag{4.30}$$

$$SS_{\text{res}} = \sum_{i=1}^{k} \sum_{j=1}^{n_i} (x_{ij} - \bar{x_i})^2 \tag{4.31}$$

$$SS_{\text{total}} = \sum_{i=1}^{k} \sum_{j=1}^{n_i} (x_{ij} - \bar{x})^2. \tag{4.32}$$

The F-test will reject the null-hypothesis at level α if

$$F = \frac{SS_{\text{effect}}/(k-1)}{SS_{\text{res}}/\left(\Sigma_{i=1}^{k} n_i - k\right)} > F_{k-1,\Sigma_i(n_i)-k}(\alpha) \tag{4.33}$$

Extending the univariate model in (4.29) to the multivariate case gives a model

$$\boldsymbol{X}_{ij} = \boldsymbol{\mu} + \boldsymbol{\tau}_i + \varepsilon_{ij}, \tag{4.34}$$

where $\varepsilon_{ij} \sim N(0, \Sigma)$. The sum of squares considered in the univariate case, will in the multivariate case be denoted between ($\boldsymbol{B}$) and within ($\boldsymbol{W}$) sum of squares given by

$$\boldsymbol{B} = \sum_{i=1}^{k} n_i(\bar{\boldsymbol{x}}_i - \bar{\boldsymbol{x}})(\bar{\boldsymbol{x}}_i - \bar{\boldsymbol{x}})' \tag{4.35}$$

$$\boldsymbol{W} = \sum_{i=1}^{k}\sum_{j=1}^{n_i}(\boldsymbol{x}_{ij} - \bar{\boldsymbol{x}}_i)(\boldsymbol{x}_{ij} - \bar{\boldsymbol{x}}_i)' \tag{4.36}$$

The total matrix is given by $\boldsymbol{B} + \boldsymbol{W}$. One way to test the null-hypothesis

$$H_0 : \boldsymbol{\mu}_1 = \cdots = \boldsymbol{\mu}_k \tag{4.37}$$

against the alternative

$$H_1 : \boldsymbol{\mu}_i \neq \boldsymbol{\mu}_j \quad \text{for all}(i, j), \tag{4.38}$$

is by means of *Wilks' lambda* test statistic given by

$$\Lambda* = \frac{|\boldsymbol{W}|}{|\boldsymbol{B} + \boldsymbol{W}|}. \tag{4.39}$$

The hypothesis is rejected if

$$\frac{|\boldsymbol{W}|}{|\boldsymbol{B} + \boldsymbol{W}|} \leq U(p, k-1, n-k)_\alpha. \tag{4.40}$$

Here U relates to the distribution of the test statistic under the null-hypothesis, since Wilk's lambda is dependent on the number of variables and number of groups. It should be noted that both the univariate and multivariate cases of ANOVA can be extended to two-sided analyses.

Again the review of the statistical test is based on the terminology presented by Johnson and Wichern (2002) and Ersbøll and Conradsen (2012).

4.5.3 Variance Component Analysis

An efficient tool that extends the ANOVA and MANOVA is the variance component analysis. When performing an ANOVA the effects related to variables can be considered random or fixed. Random effects relate to categorical variables where each observation is a stochastic measurement. Fixed effects relate to variables that are pre-determined, e.g. sex, type, etc. In a variance component analysis we wish to determine if the random effects are important or if they can be excluded as a factor in the analysis. This is done by assessing the proportion of variance that is due to the random effect's variable and, if present, interaction with other effects. We shall not dwell upon this but refer to textbooks on mixed models in ANOVA, e.g. (Galwey, 2007).

Part II

Applications

Chapter 5

Color

This chapter presents how the color transformations and segmentation methods presented in Sections 4.1 and 4.2 have been applied in the process of assessing color of meat and meat products. The results presented here are summaries of the results obtained in Papers A, B, C, and D.

Paper A contributes with an elaborate study on assessment of meat color with a multispectral imaging system. The study showed that the spectral properties of meat can influence the assessment of color, and that the applied vision system is less influenced by the scattering events occurring underneath the surface of the meat than the colorimeter.

Paper B is an extension of the study in Paper A. Where Paper A shows that the vision system is a valid instrument for color assessment, Paper B presents how the multispectral images can be of use in visualization and give a solid estimate of the distribution of color across the meat samples.

Sensory panel scores are related to instrumental color assessment in Paper C. Here the vision system presented in Section 3.2 and Paper F was applied. The study showed that the color measurements by the vision system and the colorimeter had equal correlation with the sensory panel scores. More importantly, it was shown that the colorimeter was more affected by the lightness of the samples than the vision system assessment.

Finally, the color measurements in Paper D, concerning the study of fermented salamis, gave an impression of the difference in color for chilled and non-chilled samples. The statistical models showed that the color difference between chilled and non-chilled samples corresponds to the color change obtained by fermenting salamis three more days.

5.1 Multispectral Meat Color Assessment

The objective of the study in paper A was to show that a multispectral imaging system assesses meat color in a similar or even superior manner when compared to the traditional colorimeter.

The study involves fresh meat samples from different animals (pork, beef, and turkey), and also processed products. This way we ensure that the comparison of the two instruments are based on samples representing a wide range of the scenarios that can arise within meat color measurements. Hence it can also be investigated if there is a product specific difference for the two instruments.

As stated in Section 4.1 the preferred color space within meat science is CIELAB. This color space has the advantage of being closely related to the human perception of color (León et al., 2006). The images are captured with the commercial multispectral imaging system VideometerLab described in Section 3.1. The applied version of the instrument has 19 spectral bands, where 12 of them are in the visual spectrum (400 - 700 nm). As described in Section 4.1 we can find a suitable transformation from knowledge about the spectral bands of the multispectral imaging system and the color matching functions of the CIE XYZ space. Figure 5.1(a) shows how the spectral bands are distributed in the visual spectrum. This information is contained in the columns of $\boldsymbol{B}$, and the color matching functions of the CIE XYZ tristimulus values are contained in $\boldsymbol{A}$. In this case we consider illuminant D65. We find the transformation from the 12 visible bands to CIE XYZ values by solving a linear system of equations as in Section 4.1, equation (4.4). The graphs in Figure 5.1(b) show the fit of the multispectral bands to the CIE XYZ color matching functions at illuminant D65. We see that around 550 nm – the green interval of the spectrum – a lack of fit is present due to the absence of an LED around this wavelength.

For an initial investigation of the two instruments, the ΔE^*_{ab} values for a classic color checker were investigated. Table 5.1 summarize the performance of the two instruments, which gives the general expression that the colorimeter returns colors closer to the ground truth value of the color checker. The average value of the colorimeter measurements is 3.5, with a maximum value of 8.5 and minimum

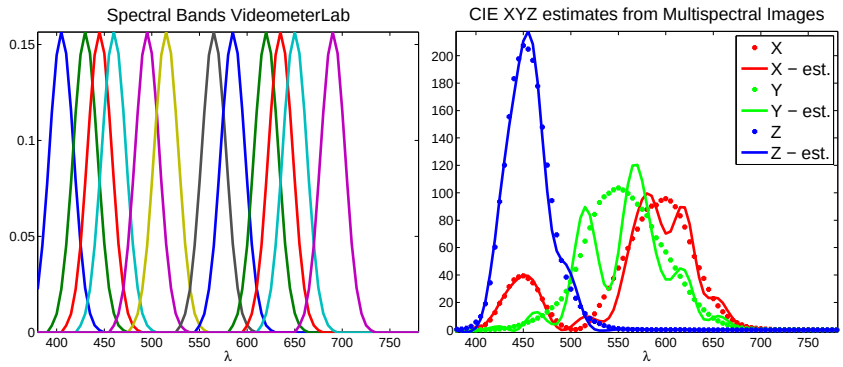

(a) Spectral bands of the VideometerLab. (b) CIE XYZ color matching functions and fit of spectral bands.

Figure 5.1: Data for fitting the spectral bands of the VideometerLab to the CIEXYZ color matching functions.

of 0.2. The corresponding values for the multispectral images are 6.94, 13.66, and 0.58. This shows that the colorimeter generally measures colors of the color checker closer to the ground truth value. But as described in Section 2.1.1 meat has diffuse scattering properties, and the study of the two instruments will take this fact into consideration.

The meat color measurements by the colorimeter are the average of four spot measurements, so in order to have an equal comparison basis for the colorimeter and the colors obtained from the multispectral images, we simulate these spot measurements in the images. The comparison of the color assessment by the two instruments is based on a variance component analysis with the model

$$\begin{aligned} Y_{hjkil} = \quad & \mu + p_h + t(p)_{j(h)} + S(TP)_{k(jh)} + m_i + mp_{ih} + mt(p)_{ij(h)} + \\ & MS(TP)_{ik(jh)} + L(MSTP)_{l(ikjh)} + \varepsilon \\ & h = 0, 1, \quad i = 1, 2, \quad , j = 1, \ldots, 7, \\ & l = 0, \ldots, 4 \quad k = 1, \ldots, 5. \end{aligned} \tag{5.1}$$

In this model we consider the effects processing level, p, method of measurement, m, and type within processing, $t(p)$, to be fixed. The random effects are sample within type and processing level, $S(TP)$. As a result, the interaction of the effects method and sample within type and processing, $MS(TP)$ is also considered random. The error term is given as $L(MSTP)$, and finally Y represents one of the three color components, L^*, a^*, or b^*.

The analysis by the model in (5.1) showed that the L^* component is assessed

Table 5.1: ΔE^*_{ab} for all 24 colors of the color checker. Values are given for the colorimeter (CM) and the multispectral imaging system (MSI).

Color	ΔE^*_{ab} CM	ΔE^*_{ab} MSI	Color	ΔE^*_{ab} CM	ΔE^*_{ab} MSI
Dark Skin	1.4	8.98	Blue	4.7	10.99
Light Skin	4.2	5.98	Green	4.8	9.37
Blue Sky	2.8	1.58	Red	4.6	19.3
Foilage	2.8	5.23	Yellow	6.5	3.02
Blue Flower	3.4	3.56	Magenta	3.9	13.66
Bluish Green	4.0	6.76	Cyan	8.3	7.18
Orange	1.8	11.40	White	0.7	0.58
Purplish Red	8.5	3.97	Neutral 8	1.1	1.67
Moderate Red	1.7	12.97	Neutral 5.5	1.3	2.18
Purple	3.8	10.31	Neutral 5	1.0	1.85
Yellow Green	4.8	5.98	Neutral 3.5	1.2	3.59
Orange Yellow	7.1	7.53	Black	0.2	9.00

more equally by the two instruments, than the a^* and b^* components. The variation of the a^* and b^* component is ascribed to the method of measurement effect and the processing level. For all three color components the interaction effect $MS(TP)$ is non-significant. Hence the variance estimate for each of the three color components were described by the combined measurement error (σ^2), the chosen location, $\sigma^2_{L(MSTP)}$ and the chosen sample ($\sigma^2_{S(TP)}$).

A further analysis of the color data, gave a general impression that the colorimeter assessed the chromatic components, a^* and b^*, at a lower level than the imaging system, but as the variance component analysis also revealed, the assessment of a^* was dependent of the processing level of the samples. The a^* and b^* component of the colorimeter, showed a higher correlation with the measured L^* values, which indicated that the colorimeter color assessment is more likely to be influenced by the lightness of the sample than the multispectral imaging system.

The study indicated that even though the colorimeter assess the color of a color checker slightly better than the vision system, the structure and reflectance properties of meat samples can lead to biased results for the colorimeter. The vision system on the other hand employs diffuse lighting, so the scattering properties of the meat are handled in a correct way. This combined with the fact that it can capture the total surface of a sample, makes the multispectral vision system a most valid, and even a superior system, for meat color assessment in certain situations.

Paper B is an extension of paper A. In Paper A only spot measurement in the

image data are considered, and Paper B then describes how the image data can be used to exploit its full potential. The segmentations are performed with linear discriminant analysis – see Section 4.2. The average values and standard deviations of the three color components of lean meat are found from the segmentations, and they give a clear impression of the color variation across the samples. Moreover, examples of visualization methods are given.

5.2 Meat Color Assessment and Sensory Panel Scoring

In paper A the objective was to compare two different methods for instrumental color assessment, but researchers often wish to compare the results of a color measurement with the scores of a sensory panel. Paper C relates the color measurements of a computer vision system (CVS) employing an RGB camera and a colorimeter with the human assessment of meat color.

The vision system employed in Paper C is the structured light system described in Section 3.2 and Paper F. Even though an RGB vision system has its limitations (Wu and Sun, 2013), the prototype of the described vision system was employed in the study for Paper C.

Three different cuts of beef, *longissimus dorsi* (LD), *semimembranosus* (SM), and *psoas major* (PM), with three different aging periods were investigated in the study. The three different types of muscle were carefully selected due to their difference in color stability properties, with LD being most color stabile and PM most color labile. Muscles from eight animals were harvested, and after the ascribed aging time a slice of the muscle was put on display for a week. On the first, the fourth and the seventh day of display the samples were scored by a trained sensory panel for both lean meat color and discoloration. On the same observation days the color of the samples were also assessed with a colorimeter and the computer vision system.

The processing of the images in the study were based on several of the methods described in Chapter 4. At first a segmentation of background, fat, and lean meat was carried out by linear discriminant analysis – see Section 4.2. The transformation from RGB to CIEXYZ and then to CIELAB values were carried out as described in Section 4.1. The optimization problem in (4.4) was in this case based on an $\boldsymbol{A}$ matrix with ground truth values of a Macbeth color checker under D65 illumination. The values in the regression matrix $\boldsymbol{B}$ will be found from pixel averages in images of the color checker. The study considered three methods for construction of the regression matrix:

WPPLS *White Point Preserving Least Squares*: The three columns of $\boldsymbol{B}$ represent the observed R, G, and B values. Equality for the white square of the color checker was ensured by constraining the problem.

PLS *Polynomial Least Squares*: Columns of $\boldsymbol{B}$ are R, G, B, R^2, G^2, and B^2 and there are no constraints.

PWPPLS *Polynomial White Point Preserving Least Squares*: Columns of $\boldsymbol{B}$ as above, but with the constraint from WPPLS.

The deviations from the color checker for the three transformations were evaluated by the ΔE^*_{ab} values and the correlation with the sensory scoring. Based on the results it was chosen to use the WPPLS transformation. An example of the three color components, L^*, a^*, and b^* in a segmented image can be seen in Figure 5.2. The average values of L^*, a^*, and b^* for the pixels of lean meat were used in the further study, along with the parameters chroma ($c^*_{ab} = \sqrt{(a^*)^2 + (b^*)^2}$) and hue angle ($h^*_{ab} = \arctan(b^*/a^*)$).

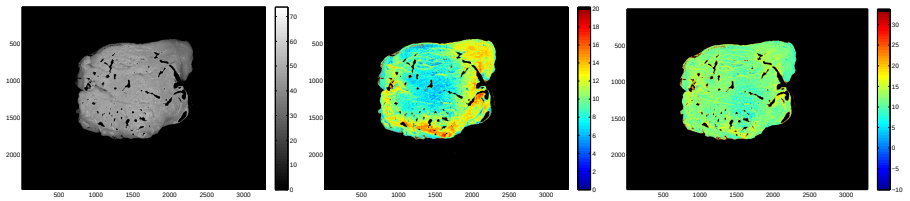

(a) L^* (b) a^* (c) b^*

Figure 5.2: Segmented and transformed images split on the three color components of CIELAB with fitted color scales.

Six different color parameters are now obtained; sensory scores for lean meat color and overall discoloration, colorimeter measurements (chroma and hue angle), and average color from the computer vision system (hue angle and chroma). We consider chroma values as representative of lean meat color scores and hue angle values to be related to discoloration scores (Hunt et al., 1991). The variance structure of the three different measurements are investigated by individual ANOVAs with the model

$$\begin{aligned} y_{jkl} = \quad & \mu + a_j + m_k + d_l + am_{jk} + ad_{jl} + md_{kl} + \varepsilon_{jkl}, \\ & j = \{9, 16, 23\}, \quad k = 0, 1, \quad l = \{1, 4, 7\}. \end{aligned} \tag{5.2}$$

The main effects considered are aging time (days), a_j, muscle type, m_k, days of display, d_l. μ is the overall mean, ε_{jkl} is the error term. Interactions of the

main effects are also included in the model. y_{jkl} represents one of the six color parameters.

The ANOVAs revealed that the contributors to variance of the lean meat color scores are the same as for the chroma values for both the colorimeter and the CVS. Similar results were obtained for the discoloration scores and hue angle values for the colorimeter and CVS. These results also indicate that it is reasonable to perform a correlation analysis to see if one of the two instrumental color assessment methods has a higher correlation with the sensory scores.

In the correlation analysis the different days of display were considered by themselves across muscle types at first, and hereafter the three muscle types are considered individually across days of display. This analysis showed that the colorimeter has a low correlation when the lighter LD muscle is considered, and especially on the first day of display. Both systems show high correlations for the darker samples, the PM muscle, and the later days of display.

The statistical tests of the study showed that the vision system is capable of assessing color that relates well to the human perception of color. The colorimeter measurements easily become biased due to the spot measurements, and the vision system offers the opportunity to get a complete impression of the sample. This is especially important when discoloration is the subject of investigation.

5.3 Salami Color

In paper D we present a study on fermented salamis with different starter cultures added. The starter cultures are lactic acid bacteria (LAB) with specifically chosen properties that influence the salami with respect to taste, color, and other characteristics (Leroy and De Vuyst, 2004). Moreover, they have a microbial function and therefore prolong the shelf life of the products (Leroy et al., 2006). A sensory panel is a strong tool in a product development process, but also easily influenced by e.g. difference in assessment times (van Kleef et al., 2005). It can therefore be difficult to assess the quality traits and monitor the development of a fermented sausage over time. It would be beneficial if it was possible to present all fermentation stages to the panel at the same time point, but we also need the salamis to be from the same batch. In paper D we investigate if it is possible to pause the fermentation by deep-chilling samples at -2°C.

The study involves salamis with four different recipes of starter cultures and observations from 2, 3, 9, 14, 21, and 42 days after fermentation onset. On each observation day two salamis from each recipe were taken from the smoker - one

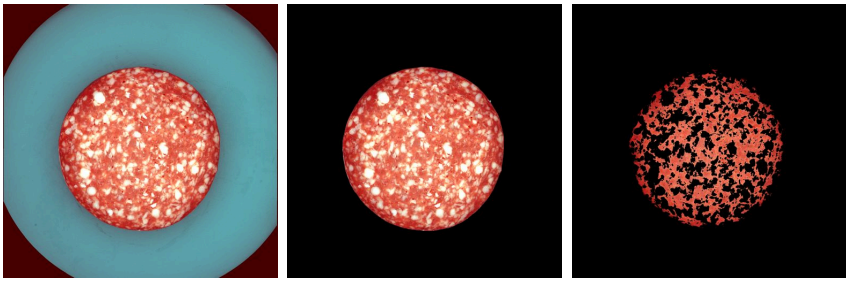

Figure 5.3: From left to right: Pseudo RGB image of a day 14 sample, background/salami segmentation, and fat and meat segmentation.

was sliced and imaged with a multispectral imaging system, and the other was placed in the chiller at $-2°$. After approximately 42 days of fermentation the chilled samples were removed from the chiller and after refrigerator temperature they were also sliced and imaged. For each sample - chilled or non-chilled - three slices of 2 cm height were captured with the multispectral imaging system VideometerLab described in Section 3.1. For day 42 only non-chilled samples are a part of the data set and we hereby obtain $n = 132$ samples in total.

We wish to assess if there is any color difference for the meat in the chilled and non-chilled samples by analysis of the multispectral images. The first steps in this process is to perform segmentations of background, meat, and fat. Here we utilize the supervised statistical methods described in Chapter 4, and more specifically apply the canonical discriminant analysis (CDA). The segmentations are therefore based on training areas in the images. Figure 5.3 shows a pseudo RGB image of a salami, and the two segmentations.

The first approach to determine if there is any color difference for the two groups of samples includes all spectral bands. By defining training areas of the meat in samples from day 2 and 42 - the two extremes - and again performing an nCDA based on this training data, we can map the pixels representing meat to an artificial color scale. Examples of the resulting color scales are shown in Figure 5.4.

Since the fermentation happens evenly from the rim towards the center of the salami we extract average color information at specified radii. These distance dependent observations are subject to a PCA, which shows that a large part of the variation is due to the difference in fermentation stages, but a small, and not insignificant part, is due to the chilling process. We establish whether there is a statistically significant difference by performing an ANOVA for each of the

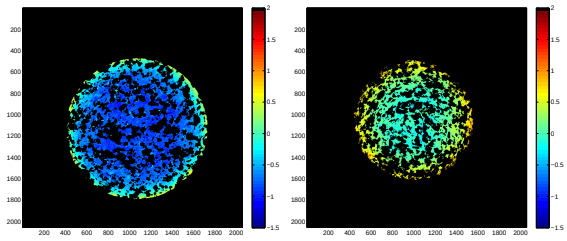

Figure 5.4: CDA meat color scale for a day 2 and day 42 sample. It is here clear how the fermentation stage is reflected in the meat color scale. Blue to red on the color scale represents darkening of meat.

first two PCs. An extensive model is considered

$$y_{ij}(t) = \mu + c_i + r_j + c_i r_j + \beta_{ij} t + \gamma_i j t^2 + \varepsilon_{ij}, \qquad (5.3)$$
$$i = 0, 1, \quad j = 1, 2, 3, 4.$$

This is a function of time, t, and dependent on chilling effect, c, and recipe type effect, r. The ANOVA of the first and second PC respectively showed that the deep-chilling process is a significant factor, and that it does actually contribute to a difference in color for the deep-chilled and non-chilled samples. By a stepwise selection based on the model in (5.3).. it was found that the first PC is described by the model:

$$p_1(t) = \begin{cases} \alpha_0 + \beta_0 t + \gamma t^2, & c = 0, \\ \alpha_1 + \beta_1 t + \gamma t^2, & c = 1. \end{cases} \qquad (5.4)$$

It is possible to formulate this model as a parabola with a shift, δ, for the chilled samples, such that

$$p_1(t) = \begin{cases} \alpha + \beta t + \gamma t^2, & c = 0 \\ \alpha + \beta(t - \delta) + \gamma(t - \delta)^2, & c = 1. \end{cases} \qquad (5.5)$$

Fitting the data of the first PC to such a model showed that δ was estimated to -3.2. The fit is seen in Figure 5.5. This result indicates that the average color difference for the chilled and non-chilled samples are approximately 3 days.

The above result showed a statistical difference in color for the two groups of samples, but it would be great to relate the difference to a visual difference. Once again we therefore resort to the color transformation for a multispectral imaging system described in Section 4.1 and apply it as is done in Section 5.1. We hereby obtain CIELAB images of all samples by finding a suitable transformation of the 12 visible bands as described in Section 4.1. By applying the segmentations

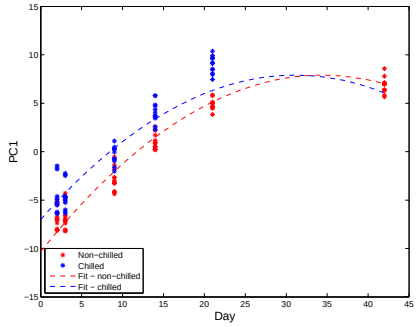

Figure 5.5: The first PC of the color data as a function of fermentation days for non-chilled and chilled samples. The resulting fit shows a difference of three days for the two groups.

obtained earlier in the study to the CIELAB images we can e.g. find an average color of the inner part of the salamis. The inner third is often used for sensory panel evaluation. We evaluate the ΔE^*_{ab} values between chilled and non-chilled samlpes for each recipe type at day 2, 3, 9, 14, and 21. Hence it was found that the ΔE^*_{ab} values are all under 3 units, which is on the edge of being detectable by human vision (Larraín et al., 2008).

The change in color is a significant part of the fermentation process. Two other factors are shrinkage and texture changes, which have also been investigated. The result of the texture analysis is presented in Chapter 6. The results of analyzing the shrinkage in width of the salami showed approximately a days difference for the two groups of samples.

Chapter 6

Texture

This chapter will present how the image texture methods described in Section 4.3 are used in papers D and E. The image modalities are very different in the two contributions - multispectral images obtained with diffuse lighting by the VideometerLab (see Section 3.1) in paper D and hyper spectral images with a coherent laser in paper E.

Paper D shows that the change in texture during a fermentation process of salamis can be captured by histograms of gradient magnitudes. It was in this way possible to show a texture difference for chilled and non-chilled salami samples. Moreover, it showed that the gradient magnitude histogram approach was suitable for the analysis of fermented salamis.

Paper E is a general analysis of the 2D SLS image from the instrument described in Section 3.3. The study involves samples of lard from boars with the objective of identifying suitable descriptors or image features for skatole and androstenone levels. It could be that the levels of these lead to a differences in speckle patterns as described in Section 4.3.2 and Section 6.2 presents the application of this method. Unfortunately the analysis did not support this hypothesis.

6.1 Gradient Magnitude Histograms

The fermentation process of sausages involves a drying of the meat by water evaporation (Leistner, 1995), and as can be seen in Figure 6.1 this influences the color of the sample (described in the previous chapter), but also the transition from meat to fat. The farther in the fermentation process, the distinction between meat and fat becomes blurred. The concept of the gradient magnitude histograms described in Section 4.3.1 will be applied in order to capture this texture change during fermentation.

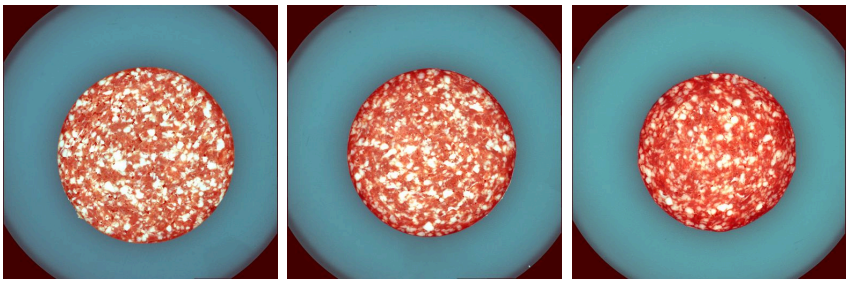

Figure 6.1: Pseudo RGB images of a fermented sausage from day 2, 14 and 21 (left to right). A clear development in texture from a loose structure to a more clear distinction between fat and meat.

Figure 6.2 shows how the gradient magnitude is dependent on scale for the 17th spectral band (890 nm) for samples from day 21. Since the images would give a high gradient value at the periphery of the salami, these values are not included in the histograms, and neither seen in the illustration in Figure 6.2.

The histogram data for all the 132 samples were gathered in order to analyze if there is any difference in texture for chilled and non-chilled samples. The histograms are based on only one spectral band (890 nm), five scales as defined by a Gaussian pyramid, and 64 bins within each scale. For each sample the histograms for the five scales are concatenated, such that histograms like the one seen in the bottom-right of Figure 6.2 are obtained.

In order to analyze the histogram and investigate the sensitivity towards texture for chilled and non-chilled samples, a PCA is performed as described in Section 4.5.1. The analysis of the principal components (PC), showed that the first three explain approximately 80% of the variance in the histogram data. The first PC described 64% of the variance by itself. The difference for the first PC describes the contrast between the very small gradient magnitudes and the second shows the differences for the larger gradient magnitudes. Plotting these first three

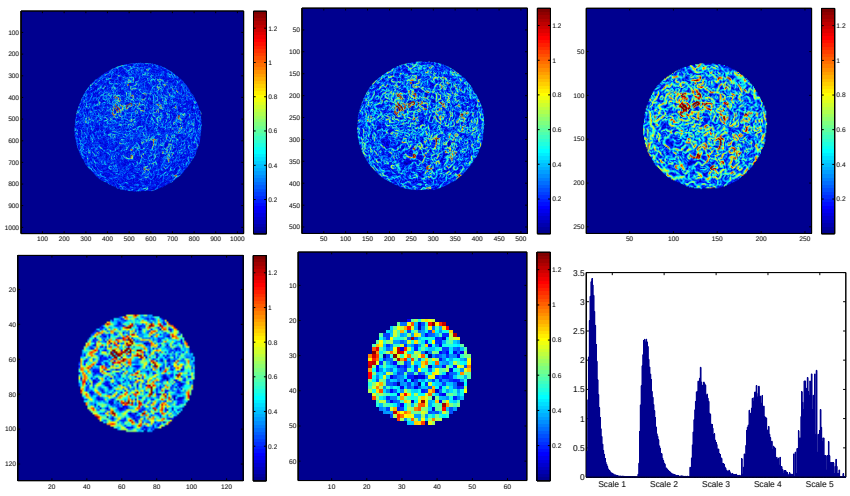

Figure 6.2: Gradient magnitude images at five scales and the concatenated histogram.

PCs against the observation days, indicated that the data was described by equal models, but with parameters dependent on chilled or non-chilled effect.

The ANOVA of the principal components based on the extensive model described in (5.3), showed that all three PCs were dependent on the chilling effect. This gives reason to believe that the chilling process does influence the fermented sausages.

6.2 Analysis of Speckle Patterns

The speckle patterns described in Section 4.3.2 can arise when we use the 2D SLS system described in Section 3.3. The SLS system was employed in Paper E for the investigation of lard samples from boars in the quest to identify skatole and androstenone levels. The two chemical compounds are present in meat from boars and, depending on their amounts, can lead to an unpleasant odor, known as boar taint, when the meat is cooked.

The vision system returns images of resolution 1200×1600 at 56 spectral bands from 440 nm to 990 nm at 10 nm intervals. Lard from 46 animals with known levels of skatole and androstenone are considered in the study. Three replicate measurements were performed for each animal to capture the variation within

animal.

As described in Section 4.3.2 the average speckle size is found at each spectral band and it is presented in Figure 6.3. The spectra plotted are average spectra across the three repetitions for each sample, and the combined level of skatole and androstenone is represented by the color coding with red (low values of both) to blue (high values of both).

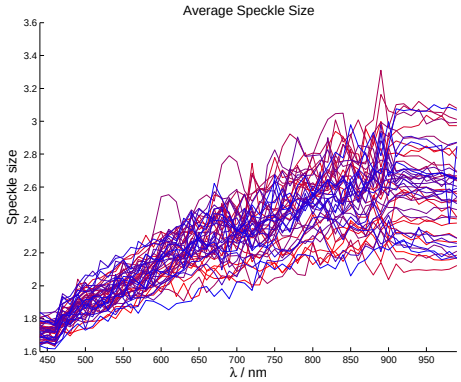

Figure 6.3: Speckle size wrt. spectral band with color coding from red to blue representing increase in combined level of skatole and androstenone.

In order to identify the important variance contributors in the data a PCA is performed for the speckle data. Figure 6.4 shows the loadings of the first three principal components. The first PC describes an average speckle size across the spectral bands with a slightly heavier weight on the longer wavelengths. The second PC holds the contrast between the shorter and longer wavelengths, whereas the third PC describes a difference between the central spectral bands and the shorter and longer wavelengths. The first three PCs describe close to 70% of the variance. The figure also shows plots of the first three principal components when plotting them against each other. The same color coding as in Figure 6.3 is used. No immediate correlation between PC value and level of skatole and androstenone seems to be present in the considered principal components.

It could be that the level of these chemical compounds only contribute very little to the variance in the data, and it is therefore very difficult to identify them. Therefore, a regression analysis on both skatole and androstenone level was performed for each of the individual PC, but unfortunately it was not possible

to find any good models.

Performing a regression analysis on the raw speckle size data itself neither gives any positive outcome. In this analysis it was important to consider the problem of division of training and test sets, and also over-fitting. Bootstrapping methods and cross validations (Hastie et al., 2009) were tested, but this did not improve the models. Hence, it is concluded that the speckle pattern is not necessarily a good indicator for differences in skatole and androstenone levels.

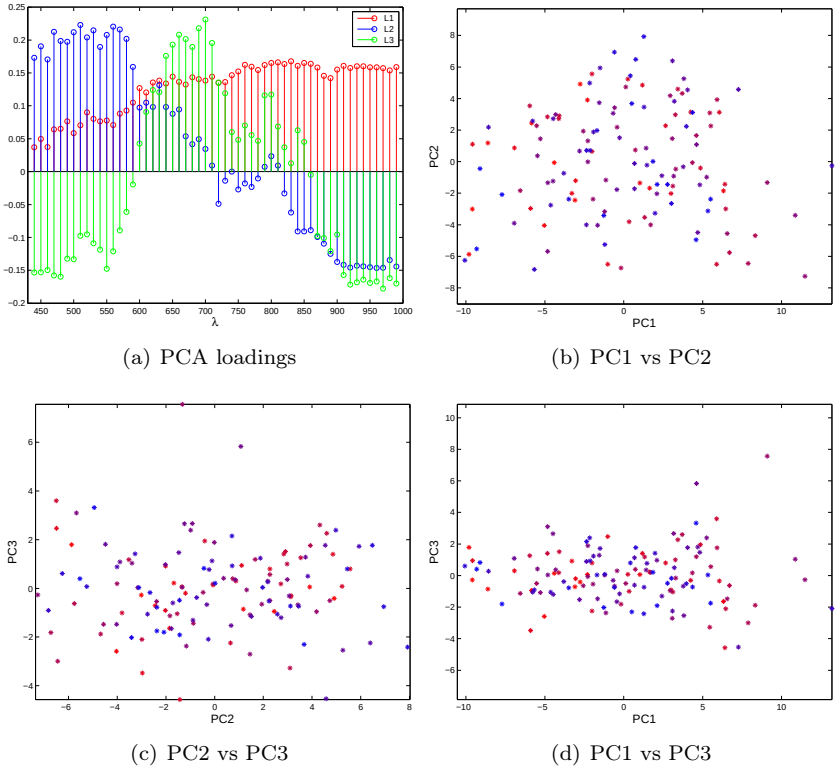

(a) PCA loadings

(b) PC1 vs PC2

(c) PC2 vs PC3

(d) PC1 vs PC3

Figure 6.4: PCA of speckle data. Loading and principal components are displayed.

Chapter 7

SLS Image Analysis

Paper E presents a study on identification of boar taint contributors. It would be beneficial to have a non-invasive method for assessing the levels of the chemical compounds skatole and androstenone that mainly gives rise to the boar taint in prepared pork (Banon et al., 2003; Babol and Squires, 1995). The analysis is based on images from the SLS system described in Section 3.3 and involves samples from 46 animals with varying skatole and androstenone level.

Analyses of images will often be based on prior knowledge about the visual change of the subject of interest. This is e.g. the case when the hyperspectral SLS images are used for monitoring the acidification process from milk to yoghurt (Skytte et al., 2012; Sharifzadeh et al., 2013). During the acidification the milk thickens due to changes in the protein aggregation, and the image analysis tools applied reflects this prior knowledge about the chemical or microstructural properties. However, it is not possible to find studies describing how the boar taint contributors influence the visual impression of lard, and the analysis described in the rest of this chapter will have an explorative nature. We wish to establish hypotheses, instead of testing them.

In addition to lack of research in this area, the analysis is made even more complex, since there is no linear relationship between the skatole and androstenone level, so a high level of skatole does not necessarily mean a high level of androstenone. It is also difficult to define a threshold value at which the human

nose can detect the smell (Bonneau et al., 1992). In fact some humans are not capable of detecting boar taint (Weiler et al., 2000).

The general analysis of the SLS images of lard from boars will be based on Fourier transformations of the principal components of the hyperspectral images. Image features capable of identifying anisotropic behavior in the Fourier images will be extracted, and the statistical analysis will investigate if it is possible to relate the image features to the level of either skatole, androstenone or a combined measure of the two.

7.1 Fourier Transformation

As the initial step in investigating the use of hyperspectral images for boar taint identification, each hyperspectral image is subject to a PCA. The PCA will be based on the center patch of the SLS image, since this is where major dynamics in the signal is located. The resulting principal components (the first two) are shown in Figure 7.1 for the two samples with the highest and lowest combined level of skatole and androstenone. The first principal component describe the average diffuse signal across wavelengths and the second principal component describes the variation close to the incident point.

Considering the absolute value of the complex Fourier spectrum of the principal components in Figure 7.1 results in the spectra seen in Figure 7.2. The FFT spectra have been smoothed with a median filter of size 10×10 pixels. There is a clear circular distribution from the center of the spectra. The difference for the two samples are not visible in the first PC, whereas the circular distribution appears different in the second PC.

7.2 Feature Extraction

From the FFT spectra several features will be extracted. First of all the average pixel value will be extracted in circles starting from the center pixel. The distance from the center at which the maximum average value is found will be extracted as a feature. A typical signal of the average values is illustrated in Figure 7.3.

The resulting features for all three repetitions from each animal are plotted in Figures 7.4 and 7.5. The observations are sorted according to combined level of

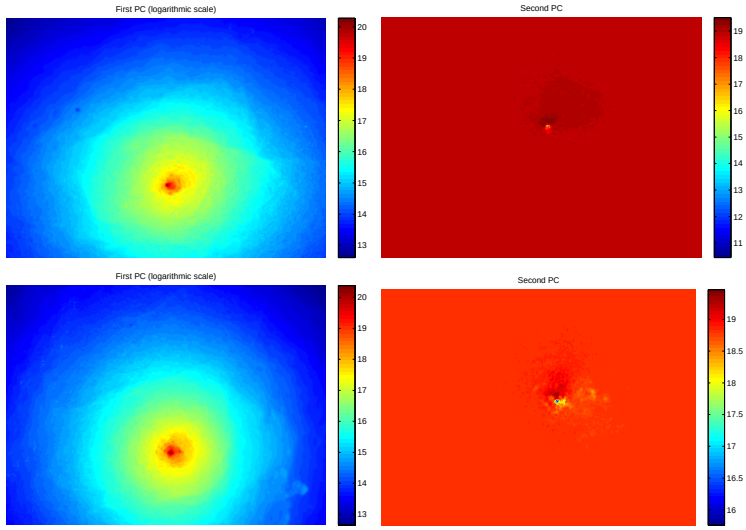

Figure 7.1: First and second principal component of the hyperspectral lard data for the two samples with the highest and lowest combined level of skatole and androstenone.

skatole and androstenone (low to high). No obvious correlation between the level of skatole and androstenone and this feature is observed for neither the first or second PC. In fact the distance at which the maximum average value is found is not varying a lot. The third repetition of animal 13 seems to be an outlier, and by further investigation it is concluded that the original hyperspectral image was not acquired correctly.

The second feature will also be based on the circular distribution of the Fourier spectra. For the circles at each considered radius, the average pixel values at 12 angle intervals will be found. The first observation of this feature will be the average value of the center patch, and the next will be at the first radius considered in the angle interval from 0 to $\frac{1}{6}\pi$, as illustrated in Figure 7.6.

The resulting signal from the features are plotted and shown in Figure 7.7 – both according to feature number, but also with respect to radius. Five radii are considered and with the polar division of the circle this gives a total of 301 variables including the center average. To give an overview the plots show an average signal across image repetitions for the three animals with the lowest combined level of skatole and androstenone (animal 11, 18, and 12) and the three with the highest combined level (animal 75, 37, and 50). Again there is no obvious relation of the features to the combined skatole and androstenone

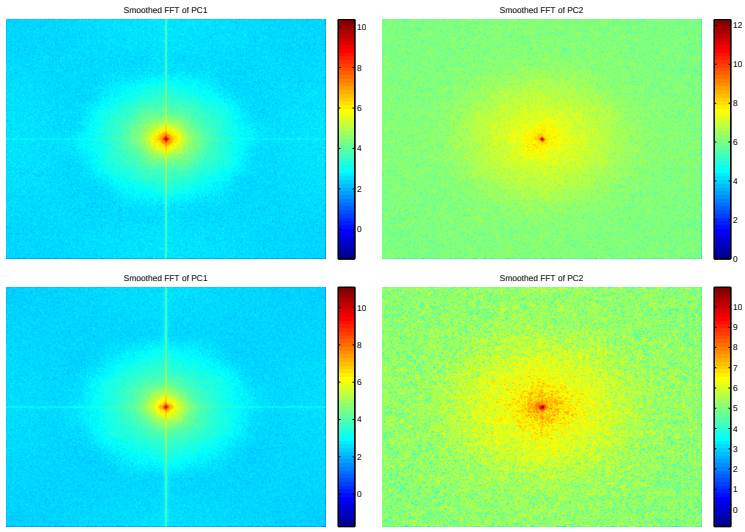

Figure 7.2: Smoothed FFT spectra of the first two principal components derived from the hyperspectral image data.

level – at least for the FFT of the first PC. Animal 50 and 75 with high levels of androstenone and skatole seem to be lying slightly above the level of the samples with a low level of the chemical compounds. Unfortunately we also observe that the features of animal 37 lie below the values of the low level samples.

The third and final feature that was extracted from the FFT spectra of the principal component is a measure of eccentricity. The approach is based on finding isocurves at certain distances from the center of the FFT image and fitting an ellipse to this isocurve. To give an impression of the feature, we again consider the three samples with the highest and lowest combined level of skatole and androstenone in Figure 7.8. The eccentricity signals considered have quite similar behavior for all levels of skatole and androstenone. Moreover the value or level of the eccentricity do not seem to have any clear relation to the level of skatole and androstenone.

The features extracted from the FFT spectra of the first and second principal components were subject to both discrimination and regression analyses, but unfortunately none of the methods showed promising results in being able to differentiate the samples with different levels from each other.

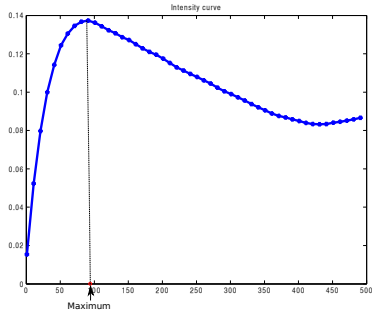

Figure 7.3: Distance from center at which the maximum average value of the FFT spectra is found.

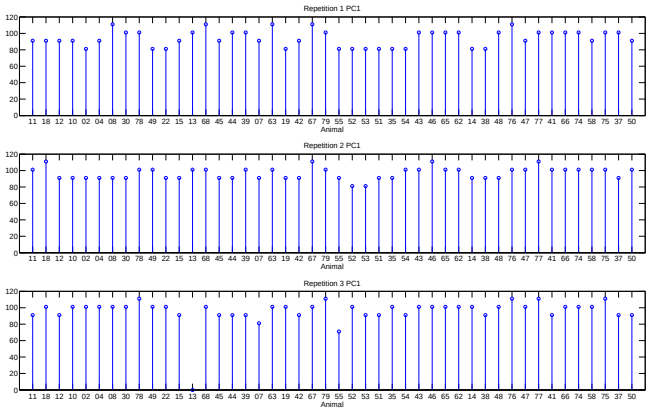

Figure 7.4: Distance from center for maximum average value in the FFT spectra of the first PC for all animals sorted by combined level of skatole and androstenone.

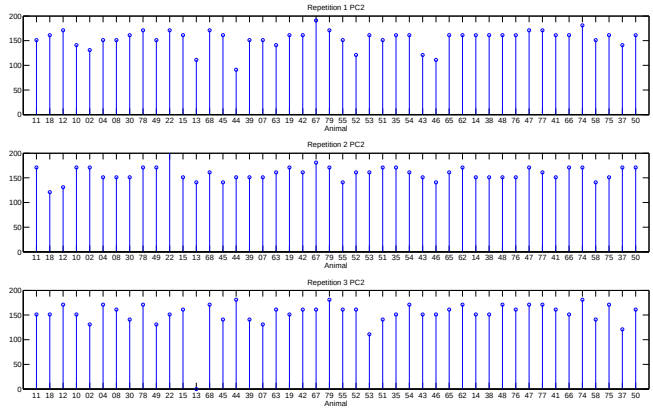

Figure 7.5: Distance from center for maximum average value in the FFT spectra of the second PC for all animals sorted by combined level of skatole and androstenone.

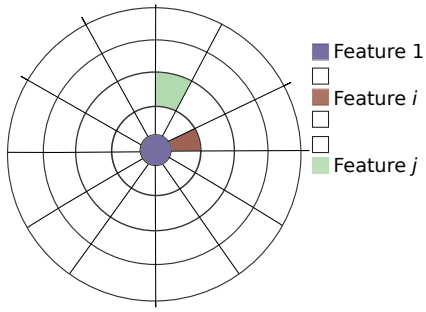

Figure 7.6: Approach to polar feature extraction. The image is sampled in the center first, and then in the first circle within the defined angle intervals.

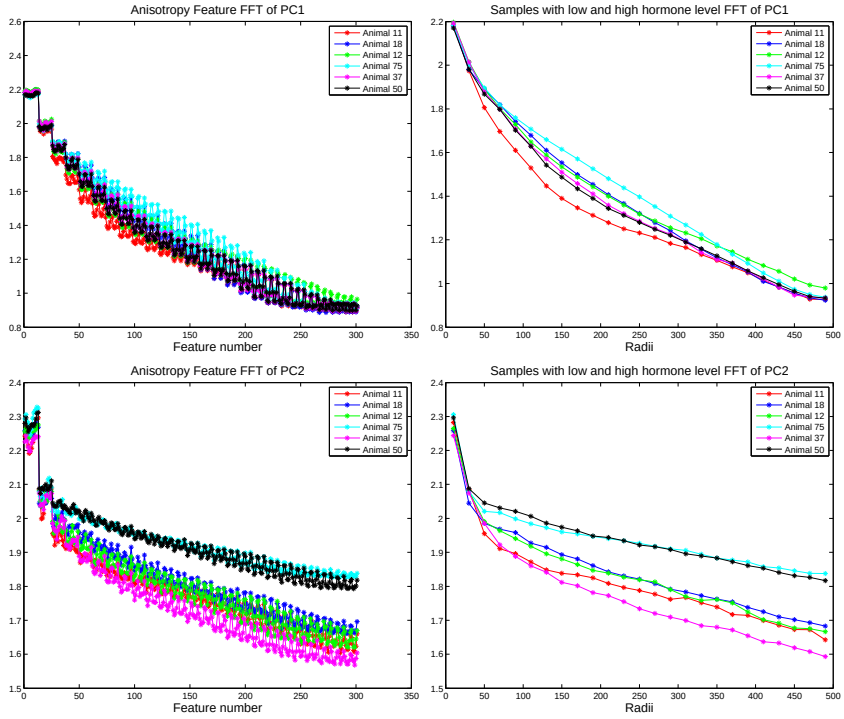

Figure 7.7: Anisotropy features for the FFT spectra of the first and second PC. Here three samples with highest and lowest levels of skatole and androstenone are seen.

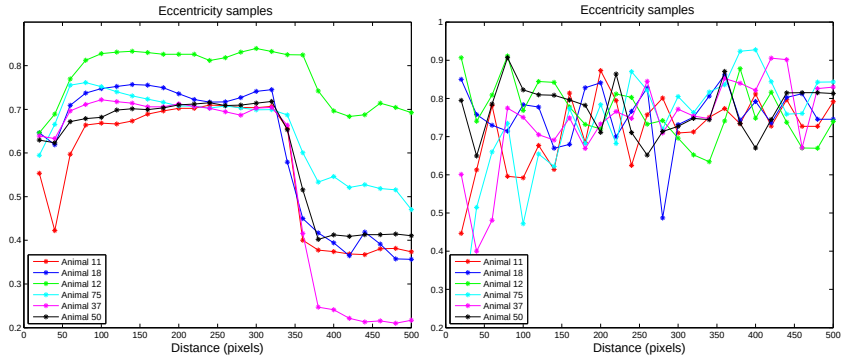

Figure 7.8: Eccentricity feature for the three samples with the highest and lowest level of skatole and androstenone for the FFT of both the first and second PC.

Chapter 8

Conclusion

The applicability of computer vision systems for measuring meat color and assessing texture have been investigated throughout the thesis. Furthermore, the application of the implemented structured light system showed promising results.

The color measurement by the multispectral imaging system showed that it is certainly a valid alternative to the traditional colorimeter. When assessing colors of a standard color checker the colorimeter returned values closer to the reference values than the vision system. Despite this fact, the vision system showed great performance in the assessment of meat color. It especially showed less dependency on the lightness of fresh meat samples than the colorimeter. Relating this to the very different scattering properties of the opaque color checker and translucent meat, it is concluded that the vision system handles the complex scattering properties of meat in a better way than the colorimeter.

The work in this thesis also showed that color measurements by a vision system correlates well with the scores of a sensory panel. The varying color stability of the muscles considered in the study was reflected in the correlations between the color measurements and the panel scores, where the vision system showed high correlations with the panel scores for early days of display, as opposed to the colorimeter. On the later days of display the correlations returned were similar. Again the results indicate that the applied vision system handle the complex

scattering properties of meat in a good manner.

The multispectral imaging system also showed its usefulness in the analysis of fermented salamis, where it was possible to show differences in both width, color and texture for chilled and non-chilled samples by use of appropriate image analysis methods. The differences could not necessarily have been assessed by other instruments. Especially the color, since the colorimeter measurements would not have been able to avoid the fat part of the salamis. The study was just one example of application of the proposed image analysis.

Investigating the use of hyperspectral images for identification of the chemical contributors to boar taint, showed that it is very difficult to relate any image features to the levels of skatole and androstenone. However, the study do reflect the importance of having a prior knowledge or hypothesis when modeling.

Finally, the development of the structured light system showed great potential. The system have already been applied for meat color assessment with great outcome, and the initial test of the multi-scale aspect of the system shows promising results. More investigations are needed though, but the complex scattering properties of meat inspires to have a system that can handle several aspects of reflectance.

The results of the work in the thesis demonstrate the potential for using multispectral and hyperspectral image analysis within production and development of meat products. The vision systems offer an objective assessment of the visual parameters and compared to the existing approaches they are fast and non-invasive.

Part III

Contributions

Appendix A

Comparison of a multispectral vision system and a colorimeter for the assessment of meat color

Meat Science 102 (2015) 1–7

Contents lists available at ScienceDirect

Meat Science

journal homepage: www.elsevier.com/locate/meatsci

Comparison of a multispectral vision system and a colorimeter for the assessment of meat color

Camilla H. Trinderup [a,*], Anders Dahl [a], Kirsten Jensen [b], Jens Michael Carstensen [a,c], Knut Conradsen [a]

[a] Technical University of Denmark, Richard Petersens Plads, 2800 Kongens Lyngby, Denmark
[b] Danish Meat Research Institute, Maglegå rdsvej 2, 4000 Roskilde, Denmark
[c] Videometer A/S, Lyngsø Alle 3, 2970 Hørsholm, Denmark

ARTICLE INFO

Article history:
Received 17 July 2014
Received in revised form 24 November 2014
Accepted 25 November 2014
Available online 5 December 2014

Keywords:
Color
Meat
Colorimeter
Multispectral
Variance component analysis
Reflectance properties

ABSTRACT

The color assessment ability of a multispectral vision system is investigated by a comparison study with color measurements from a traditional colorimeter. The experiment involves fresh and processed meat samples. Meat is a complex material; heterogeneous with varying scattering and reflectance properties, so several factors can influence the instrumental assessment of meat color. In order to assess whether two methods are equivalent, the variation due to these factors must be taken into account. A statistical analysis was conducted and showed that on a calibration sheet the two instruments are equally capable of measuring color. Moreover the vision system provides a more color rich assessment of fresh meat samples with a glossier surface, than the colorimeter. Careful studies of the different sources of variation enable an assessment of the order of magnitude of the variability between methods accounting for other sources of variation leading to the conclusion that color assessment using a multispectral vision system is superior to traditional colorimeter assessments.

1. Introduction

Whenever consumers consider buying fresh products, such as fruits, vegetables, and meat, color is used as a quality parameter. Evaluation of the product is based on earlier experiences, and expectations are set accordingly (MacDougall & Hutchings, 2002) and therefore determines the purchase. This fact makes color evaluation an important factor in not only quality control by the producer and manufacturer, but also within research and product development. It is important that such color evaluations are performed in a consistent and objective manner to achieve reliable results (Wu & Sun, 2013). Important as well, is that the color measurements reflect the human perception of color and that they can be performed in a non-invasive manner. It is therefore worthwhile investigating the current and future methods for meat color assessment.

The traditional instrument for assessing meat color is a colorimeter. The colorimeter measurements are based on a number of site measurements and the average of these is the final color measurement. This sampling strategy does not reflect the color variation of the full sample and can be hard to reproduce (Larraín, Schaefer, & Reed, 2008; Mancini & Hunt, 2005). To meet these shortcomings we suggest to use a camera based vision system. A vision system has the advantage of not being in physical contact with the meat and therefore there will be no risk of contaminating the meat by the color measurement. Earlier studies using vision systems for color evaluation have focused on converting RGB images to CIELAB values (Blasco, Aleixos, & Moltó, 2003; Chen, Chao, & Kim, 2002; Larraín et al., 2008; Mendoza, Dejmek, & Aguilera, 2006; O'Sullivan et al., 2003; Yam & Spyridon, 2004). Wu and Sun (2013) emphasize that the RGB images, among other issues, are dependent on the sensitivity of the camera employed, and cannot be directly transformed to the standardized color space, sRGB, in a consistent manner. Therefore, two systems might measure the same sample differently. Despite this issue Yagiz, Balaban, Kristinsson, Welt, and Marshall (2009) present a study on the color of fresh salmon filets where they compare the color outcome from an RGB vision system with the colorimeter measurements. Their study revealed that despite that similar results were obtained from calibration plates for the two assessment methods, the measured color of fresh salmon deviated. The color returned by the vision system had close resemblance to the perceived color of the filets, whereas the colorimeter returned grayish colors. A similar study was carried out by Girolami, Napolitano, Faraone, and Braghieri (2013), where a panel was exposed to an image of a meat sample and next to it two squares on a monitor. One square representing the color returned by the colorimeter and the other representing the color obtained from a computer vision system (CVS). The study clearly showed that the colors returned by the CVS resemble the actual sample color better than the

* Corresponding author at: Richard Petersens Plads, Bldg. 324, 2800 Lyngby, Denmark. Tel.: +45 45253463.
E-mail addresses: ctri@dtu.dk (C.H. Trinderup), abda@dtu.dk (A. Dahl), kij@teknologisk.dk (K. Jensen), jmc@videometer.com (J.M. Carstensen), knco@dtu.dk (K. Conradsen).

http://dx.doi.org/10.1016/j.meatsci.2014.11.012
0309-1740/

colorimeter measurement. The authors explain that one parameter influencing the difference of the two instruments, could be the penetration depth of the illumination source of the colorimeter.

The shortcomings of the RGB vision systems can to some extent be met by a multispectral imaging system. In this paper such a system called VideometerLab with precisely defined spectra was applied – 19 bands in the range 375 nm–970 nm (Videometer A/S, 2014). This gives the opportunity of performing camera based measurements in a spectrally consistent manner (Einarsson et al., 2006; Haeberli, 1992). The multispectral imaging system has previously been applied in meat research. Ljungqvist, Ersbøll, and Frosch (2012) studied the possibility of discriminating between naturally occurring and added, artificial astaxanthin in salmon filets. They compared the predictability of a human color scoring (SalmoFan), a colorimeter and the reflectance spectra from the multispectral imaging system. In that study the colorimeter gave less desirable discriminations than the two other instruments. In a related study for meat spoilage assessment Panagou, Papadopoulou, Carstensen, and Nychas (2014) also employed the VideometerLab by using the reflectance spectra.

To investigate the multispectral imaging system's ability to assess meat color, we chose to exploit the spectral information by simply mapping the multispectral pixel-wise information to CIELAB values with a photometric imaging model (PIM). The model is based on the spectral information of the LED light sources.

In this study meat from livestock and poultry, both fresh and processed types, are exposed to color measurements by the multispectral imaging system and a standard colorimeter. Considering these fresh and processed product types under the same conditions makes it possible to investigate how changes in the reflectance properties by processing of the meat influence the color assessment. The foundation of the analysis is a variance component analysis considering all possible effects influencing the color assessment. By performing a variance component analysis of the color measurements on the diverse set of meat samples, it will be possible to determine the order of magnitude of the different sources of variation. Thus it can be established whether the two different methods evaluate color in the same way when meat samples are considered despite a heterogenous and anisotropic material. The goal is to reach a method that can describe the true color variation across a wide variety of samples. Some preliminary results were presented in Trinderup, Dahl, Jensen, Carstensen, and Conradsen (2013).

2. Materials and methods

The set-up of the experiment will reflect that the goal of the study is to establish whether the two types of equipment for color assessment actually measure meat color in a similar manner. As stated in the introduction, it has been concluded that the two instruments assess color equally well when a color checker is concerned. The experiment is therefore set up such that the possible differences in assessment will be evident.

2.1. Samples

The experiment involved meat samples chosen such that they represented the natural color variation in different meat types. Samples ranging from dark red filet steak to lighter red pork loin and turkey breast are included as well as different products of processed meat. In the latter group of samples the meat samples have been processed by mincing, boiling and frying. In total, 12 different meat products were investigated: Seven fresh and five processed products. Within each product category there were five samples, giving a total of 60 samples. Table 1 gives an overview of the samples considered in the study.

The non-processed meat types have been frozen and thawed in a refrigerator at 5 °C prior to the experiment. The five samples within each type of product, originate from larger products. The larger products were cut into slices of approximately 2 cm in height. Since the scope of the study is to investigate the color assessment abilities of two instruments, the possible color change happening at thawing is not important in this study. These pieces are split in two and placed with the adjacent surfaces upwards for a blooming period. This meant 60 min for all samples, except veal and beef that bloomed for 80 min. This procedure made the samples mirrored, as shown in Fig. 1, and left two identical samples – one for measurement with the colorimeter and one for measurement with the multispectral vision system. Hence it was possible to perform the color measurements simultaneously.

Table 1
Table of samples and measurements. The numbers reflect the experimental set-up.

Meat type	Processing	Type*	Sample**	Method	Location***
Pork loin	No	1	1-5	1-2	1-4
Round of pork	No	2	1-5	1-2	1-4
Veal loin	No	3	1-5	1-2	1-4
Round of veal	No	4	1-5	1-2	1-4
Beef loin	No	5	1-5	1-2	1-4
Round of beef	No	6	1-5	1-2	1-4
Turkey breast	No	7	1-5	1-2	1-4
Sausage A	Yes	1	1-5	1-2	1-4
Sausage B	Yes	2	1-5	1-2	1-4
Cooked ham	Yes	3	1-5	1-2	1-4
Cooked turkey	Yes	4	1-5	1-2	1-4
Fried meat balls	Yes	5	1-5	1-2	1-4

* Type is a nested factor within processing.
** Sample is a nested factor within type and processing.
*** Location is a random factor nested within the processing, type, and sample.

2.2. Color evaluation equipment

In this study a Minolta CR-300 colorimeter was employed. This is a handheld instrument that filters the reflected light to obtain color values (Hunt et al., 1991). In Fig. 2 the colorimeter is seen while performing a measurement of a calibration plate. Measurements are influenced by the light spectrum, which can be expressed as the color temperature. It was chosen to use the D65 lightning for the colorimeter. The measurement head of the colorimeter covers a circular area with a diameter of 11 mm and the measurement sites on the sample are chosen by the operator. These sites are chosen depending on the sample, e.g. to avoid meat tendons and intramuscular fat.

The VideometerLab, which is employed for capturing the multispectral images is seen in Fig. 2. It has 20 spectral bands in the range 410 nm–955 nm where each image is 2056 × 2056 pixels, where wavelength specific LEDs and a light-integrating sphere ensure diffuse illumination in order to minimize specular reflectance. To gain color information from the multispectral images a PIM is employed to obtain CIELAB color measurements (Hardeberg, 2001; Lasarte, Vilaseca, Pujol, & Arjona, 2006). The VideometerLab has 12 bands in the visible spectrum, and their intensity distributions are the core of the PIM. Their distributions are seen in Fig. 3. From the International Commission on Illumination (CIE) we know the distribution of the CIE XYZ components under the D65 illumination, also denoted color matching functions (ISO, 11664 - 1, 2007; ISO, 11664 - 2, 1976; ISO, 11664 - 3, 1976; ISO/CIE Standard, 1976), seen in Fig. 3. The intensities of the spectra of the LEDs of the VideometerLab are fitted to the color matching functions by linear least squares fitting

$$\min_x \|AX - B\|_2^2, \tag{1}$$

where $A \in \mathbb{R}^{81\times 12}$ is the LED spectra, $B \in \mathbb{R}^{81\times 3}$ is the known CIE XYZ values, and $X \in \mathbb{R}^{12\times 3}$ is the weighting between these. The fit of the LED spectra to the CMFs are seen in Fig. 3. Hence we can now use this weighting to convert the multispectral images to CIE XYZ pixelwise.

Fig. 1. Images of several prepared samples. Left: Beef filet (top) and round of veal (bottom). Right: Round of beef.

From these images it is possible to convert these to CIELAB colors by using the standard formulas:

$$L^\star = 116f(Y/Y_n) - 16 \tag{2}$$

$$a^\star = 500[f(X/X_n) - f(Y/Y_n)] \tag{3}$$

$$b^\star = 200[f(Y/Y_n) - f(Z/Z_n)], \tag{4}$$

with

$$f(t) = \begin{cases} t^{1/3} & \text{if } t > \left(\frac{6}{29}\right)^3 \\ \frac{1}{3}\left(\frac{29}{6}\right)^2 t + \frac{4}{29} & \text{otherwise} \end{cases} \tag{5}$$

and $(X_n, Y_n, Z_n) = (0.9504, 1.0000, 1.0889)$. The color measurement capabilities were studied in Trinderup, Dahl, Jensen, et al. (2013) using a color checker. Here it was shown that the color measurement precision was the same for the two instruments.

In order to compare the colors assessed by the colorimeter with the colors obtained from the multispectral imaging system, we simulate the spot wise colorimeter measurements in the images by extracting average pixel values from four circles of ~11 mm in diameter from the CIELAB images. We can therefore not ensure that the location of the spot wise measurements are corresponding to the two instruments, hence we will consider this effect random in the further analysis. The extraction of the pixel information was performed using the Image Processing Toolbox in Matlab™.

2.3. Statistical model

The total difference for two color measurements is given as the Euclidean distance in the CIELAB color space:

$$\Delta E^*_{ab} = \sqrt{(L^*_1 - L^*_2)^2 + (a^*_1 - a^*_2)^2 + (b^*_1 - b^*_2)^2}, \tag{6}$$

In this study this parameter was used as a first indication for identifying differences in color assessment by the two different instruments.

A statistical model, based on the information in Table 1, was formulated in order to compare the two equipment types. The model accounts for the many sources of variation when considering meat samples. It was formulated as:

$$\begin{aligned} Y_{hjkil} = {} & \mu + p_h + t(p)_{j(h)} + S(TP)_{k(jh)} + m_i + mp_{ih} + mt(p)_{i\ j(h)} \\ & + MS(TP)_{ik(jh)} + L(MSTP)_{l(ik\,jh)} + \varepsilon_{hjkil} \end{aligned} \tag{7}$$

$$h = 0,1, \quad i = 1,2, \quad j = 1,\ldots,7, l = 0,\ldots,4, \quad k = 1,\ldots,5.$$

Fig. 2. Left: Minolta CR-300 colorimeter (CM) and calibration plate. Right: The VideometerLab (MSI) with the light integrating sphere.

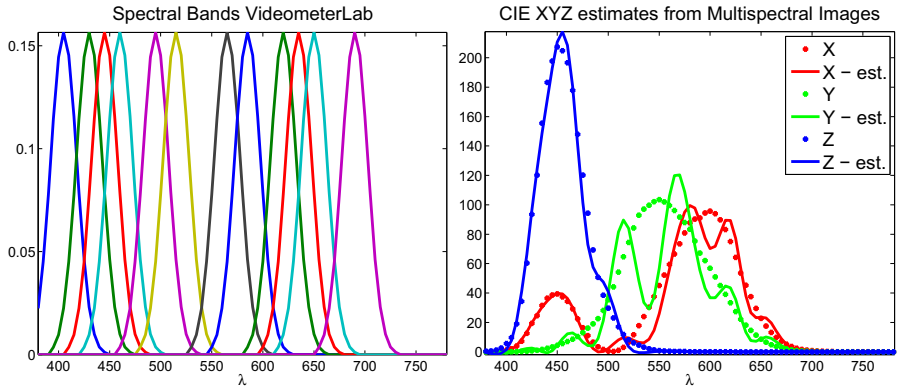

Fig. 3. Left: Spectra of the LEDs of the multispectral imaging system. All LEDs have the same relative intensity. Right: CIE XYZ color matching functions as defined by CIE and the fit of the spectra to these function.

$Y_{h\ jkil}$ represents a color measurement in one of the three color components. The model considers the effects processing level, p, type within processing level, $t(p)$, method of measurement, m, sample within type and processing level, $S(TP)$, and location within type, sample, and processing level, $L(MSTP)$. Further interactions are also considered in the model. μ is the overall mean value of the color component y and $\varepsilon_{h\ jkil}$ is the error term. The model has deterministic and random variables. In this case the random variables are symbolized with capital letters. Some effects are also nested. The variance of the three color components will be evaluated by

$$V\left(Y_{hjkil}\right) = \sigma^2_{S(TP)} + \sigma^2_{MS(TP)} + \sigma^2_{L(MSTP)} + \sigma^2, \tag{8}$$

The statistical analysis was performed in SAS 9.2. The model validation was primarily done by evaluating the residuals (and the so-called studentized residuals) obtained after fitting the models for all three parameters (L^*, a^*, and b^*). The plots used in the validation showed very similar patterns for the three parameters, and they will therefore be described simultaneously. Plotting the residuals or the observations against the predicted values showed no pattern indicating an inadequate model, and neither did a side-by-side plot of the centered fit and the residuals. The Q–Q plots and the histograms of the residuals indicated no violations of the assumption of normality and of homogeneity of variances. Thus we concluded that the models chosen describe the measurements appropriately. For a description of the diagnostic tools we refer to the SAS manual. Applying this model allows ascribing the variation in the color assessment of the meat samples to the different factors involved in the experiment; the method of measurement, meat type, processing, and sampling factors.

3. Experimental

After the blooming of the samples, the color measurements were performed. Before the actual measurements were done, all samples were dabbed with a napkin to remove excessive liquids and condensation. Hereafter the samples were exposed to the colorimeter measurements and a multispectral image was acquired with the VideometerLab. The CIELAB images of each sample were found as described in Section 2 by the use of the software accompanying the instrument. For each CIELAB image, four site measurements were computed.

4. Results and discussion

In Fig. 4 the different kinds of samples considered in this experiment are illustrated. This illustration indicates that the colors returned by the two instruments are not the same. The ΔE^*_{ab} values of the average color values are illustrated in the top left plot in Fig. 5. A clear difference in magnitude of ΔE^*_{ab} depending on the processing level of the product is observed. For the fresh products the ΔE^*_{ab} values are all above five, whereas for the processed types, the values are all under five. This clear differentiation between the fresh/raw and processed samples can be related to the threshold for human detection of color difference. Larraín et al. (2008) states that no exact threshold has been established

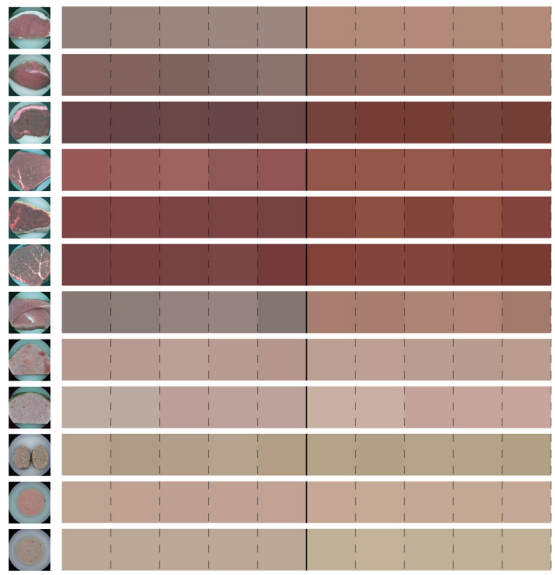

Fig. 4. Colors of the twelve different product types, as evaluated by the two instruments. Here shown in sRGB colors. Left column: Example of product type. Middle column (five blocks): Colorimeter colors. Right column (five blocks): Colors from the vision system. Colors displayed are averages of four site measurements on each sample.

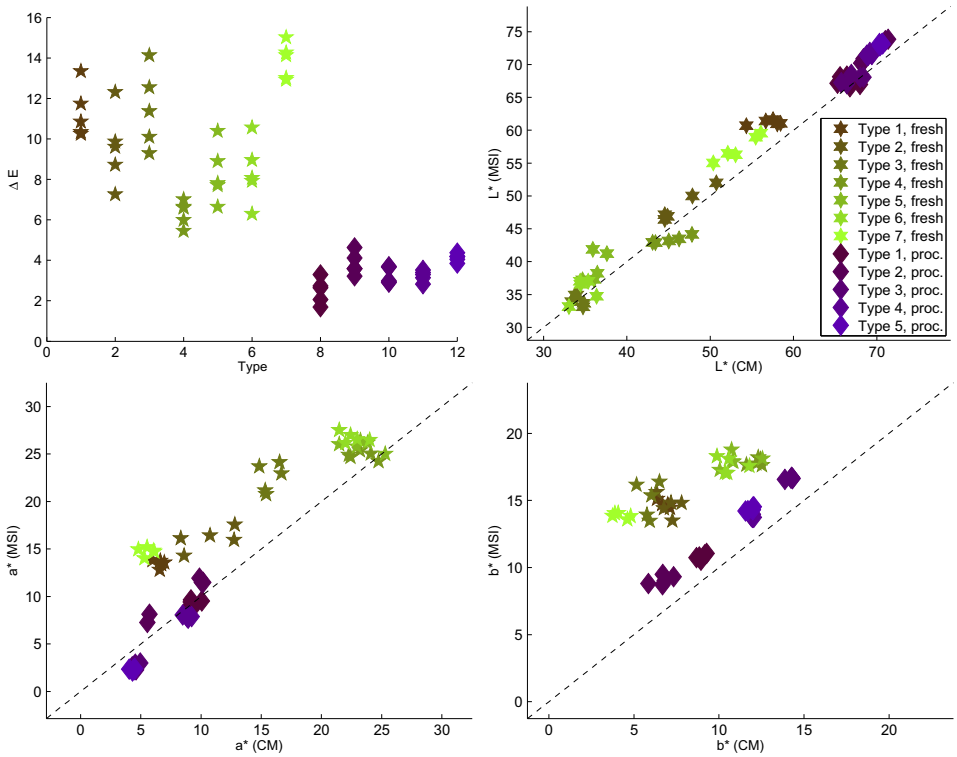

Fig. 5. Top-left plot shows the ΔE^*_{ab} values between the two methods for each sample. Top-right and bottom plots show the relations between the colors measured by the two different methods for each of the three color components L^*, a^* and b^*.

for meat color difference detection, but that a possible value could be around 2–6. This explains the visual differences observed in Fig. 4.

The remaining three plots in Fig. 5 show the average measurements of Fig. 4 split for the three color components. The values for the two methods are plotted against each other. Average values are also considered here, since there is no exact correspondence between the site measurements of the two instruments. For the L^* values a clear relation is seen along the identity line, whereas for the a^* and b^* components the relation is not as straightforward. Especially for the b^* values we see a clear difference in the relation between the fresh and processed meat types. For especially the fresh/raw samples, it is observed that the vision system returns higher a^* and b^* values. For the processed types this difference is not significant for the a^* parameter, but some systematic difference is observed for the b^* values. The figure shows that the two instruments do not return the same values for the two instruments, but it does not reflect their possible differences in color assessment abilities. The variance component analysis will reveal whether there is an actual difference.

Table 2
Summary of ANOVA for applying the model in (7) to the colors assessed by the two instruments. Mean square value (MS) and F-value of the tests are shown for all three color components.

	MS (L^*)	F (L^*)	MS (a^*)	F (a^*)	MS (b^*)	F (b^*)
m	191.58	87.36	887.58	493.13	2449.45	2667.66
mp	58.02	26.46	980.86	544.96	804.79	876.48
$mt(p)$	30.02	13.69	68.24	37.91	13.52	14.72
$S(TP)$	16.69	7.61	6.42	3.57	1.31	1.42
$MS(TP)$	2.19		1.80		0.92	
p	75,079.00	4499.79	14,659.00	2282.18	2.73	2.09
tp	2593.52	155.44	1136.49	176.93	275.43	210.71
$S(TP)$	16.69		6.42		1.31	
$MS(TP)$	2.19	0.75	1.80	1.25	0.92	1.28
Error	2.91		1.43		0.72	

In order to investigate the visible difference seen in Fig. 4 the statistical model in Eq. (7) is considered. For each of the color components, L^*, a^*, and b^*, all 480 color measurements will be included in the analysis. The results of the variance component analyses are summarized in Table 2. Comparing the tests of the three color components it is found that the F-value for method, m, is 87.36 for L^*, 493.13 for a^* and 2667.66 for b^*. For the processing factor, p, the opposite trend is observed – 4499.79 for L^*, 2282.18 for a^* and 2.09 for b^*. These results show that the L^* component is accessed more similarly by the two different measurement instruments than the other components. The variation of the a^* component is explained more by what instrument has been used and by the processing level for the samples. Finally the variation of the b^* component is likewise due to the processing level and the choice of instruments. The interaction between sample and method, $MS(TP)$, is non-significant in the test for all three components, and it is therefore concluded that there is no interaction between the method and sample within type and processing. The contribution from this term may therefore be added to the random variation. This result also indicates that the instruments are both capable of discriminating between samples within the different product categories.

As concluded above the factor $MS(TP)$ has no influence on the measurements and it is therefore assumed that $\sigma^2_{MS(TP)}$ is zero, i.e. the random variation of the color measurements may be ascribed to a combined measurement error (σ^2), a contribution from the chosen location

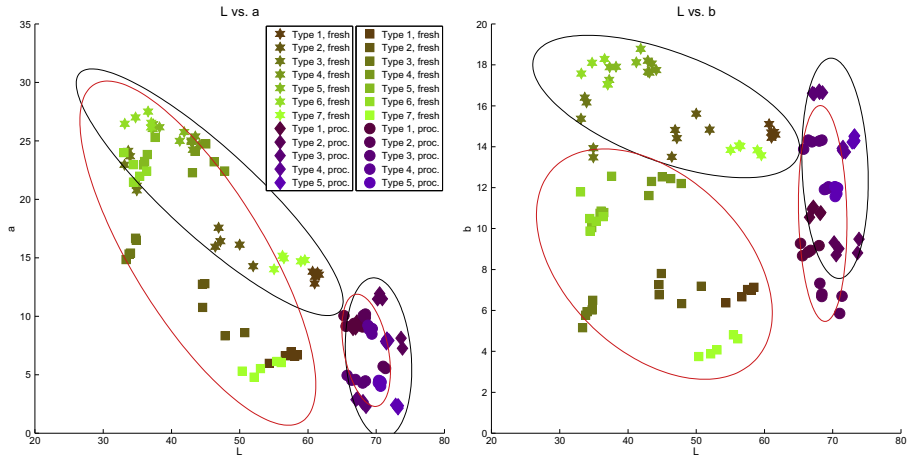

Fig. 6. The lightness component L^* against a^* and b^* values for the two different methods for each processing level. The red ellipsoids indicate the prediction interval of the colorimeter measurements (squares and circles), whereas the black ellipsoids are the prediction interval of the measurements from the vision system (stars and diamonds).

($\sigma^2_{L(MSTP)}$), and the chosen sample ($\sigma^2_{S(TP)}$). Relating this to the variance model in Eq. (8), gives variances of the three color components as

$$\hat{V}(Y_{L^*}) = 1.7217 + 2.9112 = 2.15^2 \quad (9)$$

$$\hat{V}(Y_{a^*}) = 0.6236 + 1.4346 = 1.43^2 \quad (10)$$

$$\hat{V}(Y_{b^*}) = 0.0740 + 0.7154 = 0.89^2 \quad (11)$$

The variance of the L^* component is greater than for the two chromatic components a^* and b^*, but the observations also range from 33 to 80, whereas a^* ranges from 2 to 28, and b^* from 3 to 19.

The color illustration in Fig. 4 indicates that the colorimeter yields more grayish colors for the lighter fresh products, such as pork and turkey. These products have a smaller L^* and a^* component than e.g. the beef products. The plots indicate that the chromatic components of the colorimeter results may depend more on the L^* measurement than what is the case for the vision system. In Fig. 6 the a^* and b^* values of each of the products are plotted against the corresponding L^* values. The plots are split according to fresh and processed meat types. The ellipsoids represent the 95% prediction intervals. These two plots show that the chromatic component, either a^* or b^*, has a higher dependency on the lightness component L^* for the colorimeter measurements than for the VideometerLab color results. These plots support the indication of higher dependency on the L^* value for the colorimeter.

The plots in Figs. 5 and 6 indicate that the colorimeter is very dependent on the scattering properties of the sample. The processed meat products have to some extent been homogenized due to the preprocessing, and they are visually less glossy than the fresh meat samples. This glossiness can lead to specular reflectance which will lead to a less significant contribution to the chromatic components a^* and b^* (Kigle-Böckler & Hammond, 2012). The results indicate that the diffuse illumination by the VideometerLab gives less dependency on the lightness and glossiness of the sample than the simple illumination and filtering employed by the colorimeter. These results are in accordance with the results of the study on salmon meat by Yagiz et al. (2009). This study on different meat types and processing levels reveals that the reflectance properties of fresh meat, whether that being poultry or livestock animals, can influence the colorimeter measurements and that a diffuse illumination and multispectral imaging of the sample can be a way of overcoming this problem.

Imaging the samples has several advantages compared to the colorimeter measurements. First of all it captures the color variation across the sample, but as stated above, the illumination of the imaging system is preferable to that of the colorimeter. The multispectral images also enable for several other analyses than color, such as finding fat and lean meat ratio measures by segmentation or spoilage detection. Examples of such uses are explained in Trinderup, Dahl, Carstensen, Jensen, and Conradsen (2013) and Dissing et al. (2012).

5. Conclusion

This study has shown that despite a similar evaluation of the color checker for the two measurement methods, significant differences when assessing colors of the meat samples were observed. The analysis also revealed that the physical parameters of the subjects of interest influence the color measurement. Moreover, it was possible to show that the diffuse illumination employed in the multispectral vision system meets the issues regarding the glossiness of the samples. The glossiness reflects the complexity of meat color that is determined with respect to reflectance, absorption and scattering properties of the product. These factors again depend on the chemical composition of the product. The use of a vision system with diffuse illumination is therefore considered a superior alternative to the traditional method for measuring color.

Conflict of interest

The authors declare that there is no conflict of interest.

Acknowledgment

This work has been financed by the Center for Imaging Food Quality, a project funded by the Danish Council for Strategic Research (contract no 09-067039) within the Program Commission on Health, Food and Welfare. The experiments were conducted in collaboration with the laboratory technicians at The Danish Meat Research Institute.

References

Blasco, J., Aleixos, N., & Moltó, E. (2003). Machine vision system for automatic quality grading of fruit. *Biosystems Engineering, 85*(4), 415–423.

Chen, Y., Chao, K., & Kim, M. (2002). Machine vision technology for agricultural applications. *Computers and Electronics in Agriculture, 36*(2–3), 173–191.

Dissing, B. S., Papadopoulou, O. S., Tassou, C., Ersbøll, B. K., Carstensen, J. M., Panagou, E. Z., & Nychas, G. -J. (2012). Using multispectral imaging for spoilage detection of pork meat. *Food and Bioprocess Technology*, 1–12.

Einarsson, P., Chabert, C. -F., Jones, A., Ma, W. -C., Lamond, B., Hawkins, T., Bolas, M. T., Sylwan, S., & Debevec, P. E. (2006). Relighting human locomotion with flowed reflectance fields. *Rendering techniques* (pp. 183–194).

Girolami, A., Napolitano, F., Faraone, D., & Braghieri, A. (2013). Measurement of meat color using a computer vision system. *Meat Science*, *93*(1), 111–118.

Haeberli, P. (1992). Synthetic lighting for photography. http://graficaobscura.com/synth/index.html (Online; accessed October 16, 2016)

Hardeberg, J. (2001). *Acquisition and reproduction of color images: Colorimetric and multispectral approaches.* Universal-Publishers.

Hunt, M., Acton, J., Benedict, R., Calkins, C., Cornforth, D., Jeremiah, L., Olson, D., Salm, C., Savell, J., & Shivas, S. (1991). Guidelines for meat color evaluation. *44th Annual reciprocal meat conference* (pp. 9–12).

ISO 11664 - 1 (2007). *ISO 11664 - 1: 2007(E)/CIE S 014-1/E: 2006: Joint ISO/CIE standard: Colorimetry - Part 1: CIE standard colorimetric observers.*

ISO 11664 - 2 (1976). *IISO 11664-2:2007(E)/CIE S 014-2/E:2006: Joint ISO/CIE standard: Colorimetry part 2: CIE standard illuminants for colorimetry.*

ISO 11664 - 3 (1976). *ISO 11664-3:2012(E)/CIE S 014-3/E:2011: Joint ISO/CIE Standard: Colorimetry part 3: CIE tristimulus values.*

ISO/CIE standard (1976). *ISO 11664-4:2008(E)/CIE S 014-4/E:2007: Joint ISO/CIE standard: Colorimetry - Part 4: CIE 1976L*a*b* colour space.*

Kigle-Böckler, G., & Hammond, H. K. (2012). Gloss. *Paint and coating testing manual: 15th. Edition of the Gardner–Sward handbook*, *17*. (pp. 558–568).

Larraín, R., Schaefer, D., & Reed, J. (2008). Use of digital images to estimate CIE color coordinates of beef. *Food Research International*, *41*(4), 380–385.

Lasarte, M., Vilaseca, M., Pujol, J., & Arjona, M. (2006). Color measurements with colorimetric and multispectral imaging systems. *Proceedings SPIE, vol. 6062*, (pages 0F1–0F11).

Ljungqvist, M. G., Ersbøll, B. K., & Frosch, S. (2012). *Multivariate image analysis for quality inspection in fish feed.* IMM-PHD-2012 Technical University of Denmark.

MacDougall, D., & Hutchings, J. (2002). *Colour in food — Improving quality.* Woodhead Publishing.

Mancini, R., & Hunt, M. (2005). Current research in meat color. *Meat Science*, *71*(1), 100–121.

Mendoza, F., Dejmek, P., & Aguilera, J. (2006). Calibrated color measurements of agricultural foods using image analysis. *Postharvest Biology and Technology*, *41*(3), 285–295.

O'Sullivan, M., Byrne, D., Martens, H., Gidskehaug, L., Andersen, H., & Martens, M. (2003). Evaluation of pork colour: Prediction of visual sensory quality of meat from instrumental and computer vision methods of colour analysis. *Meat Science*, *65*(2), 909–918.

Panagou, E. Z., Papadopoulou, O., Carstensen, J. M., & Nychas, G. -J. E. (2014). Potential of multispectral imaging technology for rapid and non-destructive determination of the microbiological quality of beef filets during aerobic storage. *International Journal of Food Microbiology*, *174*, 1–11.

Trinderup, C. H., Dahl, A. L., Carstensen, J. M., Jensen, K., & Conradsen, K. (2013). Utilization of multispectral images for meat color measurements. *DTU Compute — Technical Report-2013* (pp. 42–48). Technical University of Denmark.

Trinderup, C. H., Dahl, A. L., Jensen, K., Carstensen, J. M., & Conradsen, K. (2013). A comparison of meat color measurements from a colorimeter and multispectral images. *Proceedings of the 16th international conference on near infrared spectroscopy 2013, vol. 1.*

Videometer A/S (2014). VideometerLab 3. http://videometer.com/Portals/0/pdfs/VideometerLab (Online; accessed 8-Oct-2014)

Wu, D., & Sun, D. (2013). Colour measurements by computer vision for food quality control — A review. *Trends in Food Science and Technology*, *29*(1), 5–20.

Yagiz, Y., Balaban, M., Kristinsson, H., Welt, B., & Marshall, M. (2009). Comparison of Minolta colorimeter and machine vision system in measuring colour of irradiated Atlantic Salmon. *Journal of the Science of Food and Agriculture*, *89*(4), 728–730.

Yam, K., & Spyridon, E. (2004). A simple digital imaging method for measuring and analyzing color of food surfaces. *Journal of Food Engineering*, *61*(1), 137–142.

Appendix B

Utilization of Multispectral Images for Meat Color Measurements

Utilization of Multispectral Images for Meat Color Measurements

Camilla Himmelstrup Trinderup[1], Anders Lindbjerg Dahl[1], Jens Michael Carstensen[1,3], Kirsten Jensen[2], and Knut Conradsen[1]

[1] DTU Compute, Technical University of Denmark, Denmark
ctri@imm.dtu.dk
[2] Danish Meat Reasearch Institute, Roskilde, Denmark
[3] Videometer A/S, Hørsholm, Denmark

Abstract. This short paper describes how the use of multispectral imaging for color measurement can be utilized in an efficient and descriptive way for meat scientists. The basis of the study is meat color measurements performed with a multispectral imaging system as well as with a standard colorimeter. It is described how different color spaces can enhance the purpose of the analysis - whether that is investigation of a single sample or a comparison between samples. Moreover the study describes how a simple segmentation can be applied to the multispectral images in order to reach a more descriptive measure of color and color variance than what is obtained by the standard colorimeter.

1 Introduction

The ability to measure color is important within meat product development and production due to color's great impact on consumer acceptance. The traditional method of assessing color by using either a colorimeter or a spectrophotometer is cumbersome and does not have the ability to capture the color variation across a sample [4]. Measuring color from images is a way of overcoming this issue. Earlier studies have shown that RGB images can be used for color assessment in the CIELAB color space as reviewed in [6]. The disadvantage when using RGB images is that they depend on the sensitivity of the camera employed and cannot be directly transformed to sRGB in a consistent manner [2]. The use of multispectral images for color assessment has previously been shown in [5]. Here, multispectral images are used to gain the advantage of additional spectral information compared to the three bands of the RGB images. The multispectral information also gives the advantage of simple mapping to the CIELAB color space. In [5] it is also shown how the meat colors assessed by the multispectral vision system were less dependent on the nature of the sample – samples of both fresh and processed meats were considered.

In this paper an extension of the study performed in [5] is presented. It will give examples on how the multispectral image information can be utilized in the color assessment of meat products. This involves visualization, segmentation, and quantification based on the segmentation. The segmentations are aimed at being applicable in the daily work of a meat scientist.

2 Materials and Methods

The study employs a VideometerLab for acquisition of the multispectral images and established statistical methods for data analysis. A standard colorimeter is applied for comparison with the measurements of the multispectral imaging system.

VideometerLab VideometerLab is a multispectral imaging device that illuminates a given sample under an integrating sphere, which causes diffuse illumination and a minimum of shadows on the sample. 19 spectral bands are considered ranging from 410 nm to 955 nm with 12 bands in the visible range. The resulting images have a spatial resolution of 2056×2056 pixels. Each spectral band is generated by a number of LEDs equally spaced at the equator of the sphere.

Color is measured by mapping the multispectral information from the visual bands to the CIE XYZ color space. This mapping is determined by finding a linear fit of the spectral bands to the CIE XYZ color matching functions. This simple idea is illustrated in Figure 1. The mapping, also denoted *photometric imaging model* (PIM), is described and validated in [5]. By mapping to the CIE XYZ color space it is possible to use standardized transformations to any other color space. In food science the CIELAB color space is often used, and will therefore also be considered in this study. In this case the transformation is given as [3]

$$\mathrm{L}^* = 116 f\left(\frac{Y}{Y_n}\right) - 16 \tag{1}$$

$$\mathrm{a}^* = 500\left(f\left(\frac{X}{X_n}\right) - f\left(\frac{Y}{Y_n}\right)\right) \tag{2}$$

$$\mathrm{b}^* = 200\left(f\left(\frac{Y}{Y_n}\right) - f\left(\frac{Z}{Z_n}\right)\right) \tag{3}$$

with

$$f(q) = \begin{cases} q^{1/3} & q < 0.008856 \\ 7.787q + 16/166 & \text{otherwise.} \end{cases} \tag{4}$$

Colorimeter The colorimeter we apply in the experiments is the Minolta CR-300 chroma. Four circular sites with a diameter of 11 mm are measured with the chroma meter. When performing measurements with the chroma meter it is important to hold the instrument perpendicular to the surface of the object. The pressure of the instrument can also influence the measurement, so the operator has to be careful when handling the instrument. The chroma meter returns the L*, a*, and b* values of each point measurement.

Segmentation The advantage of applying the photometric imaging model using a multispectral vision system is that it will be able to capture the color variation across a sample. One way to take advantage of this is to perform a segmentation

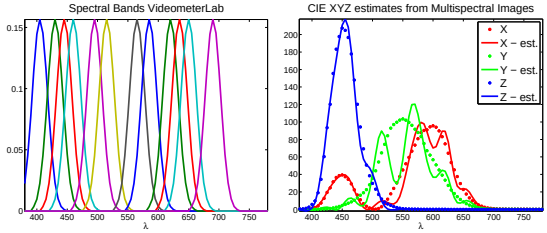

(a) (b)

Fig. 1. The spectral bands of the VideometerLab and the fit of these to the CIE XYZ color matching functions.

of the images. In this study a simple segmentation is performed by pixel-wise classification based on linear discriminant analysis. The classification rule for each pixel will be estimated by

$$S_i = \boldsymbol{x}\hat{\boldsymbol{\Sigma}}^{-1}\hat{\boldsymbol{\mu}}_i - \frac{1}{2}\hat{\boldsymbol{\mu}}_i'\hat{\boldsymbol{\Sigma}}^{-1}\hat{\boldsymbol{\mu}}_i + \ln(p_i), \quad i = \{1, \ldots, n\}. \tag{5}$$

$\boldsymbol{\mu}_i$ is the mean of the i'th class, $\boldsymbol{\Sigma}$ the pooled covariance of all classes and p_i the prior probability of observing class i. The segmentation uses information from all spectral bands. Training areas are used for estimating $\boldsymbol{\mu}_i$ and $\boldsymbol{\Sigma}$. A segmentation can lead to additional information as, e.g. a texture measure [1].

3 Results

This section presents how it is possible to change the color scale in order to enhance the purpose of the color assessment by the images, example results of the segmentation and a simple example on how to use the segmentation for quantification.

Visualization For the scientist working with color assessment it is important to be able to get a rapid feeling of the color variation across the sample of interest. Different ways of visualization can be of interest. First of all it is important to consider the three components of the CIELAB color space separately. Hereafter the color scale has to be chosen. For meat samples especially the a* component describing the amount of red color is important. Fig. 2 shows two different choices for displaying the variation of each color component. The first is based on the range of the CIELAB space – L* from white to black (0 to 100), and a* from green to red and b* from yellow to blue (-120 to 120), whereas the second is an arbitrary scale, enhancing the areas with a high or low L*, a* or b* value. The first scale is advantageous when comparing different samples, since the scale is the same for each image, whereas the second scale is preferable when only one sample is of interest.

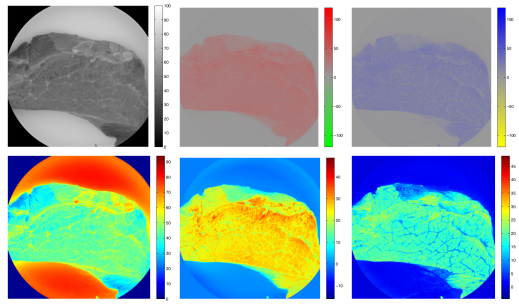

Fig. 2. Images of round of veal for each of the three color components L*, a*, and b* with two different color scales.

Segmentation The traditional method for assessing color with a colorimeter does not take full advantage of the spatial information that is gained by using a multispectral vision system. A segmentation is an excellent choice for highlighting the variance of color within a certain region of interest in the images. An appropriate segmentation for the meat color experiments could consist of segmenting background, fat and meat.

The segmentation will, as opposed to the photometric model, make use of all the multispectral bands, also the NIR ones. A simple segmentation by means of linear discriminant analysis is applied at the pixel level. An example of training areas used for estimation of mean and covariances of the three classes are seen in Fig. 3. The segmentation aims in this case at a mask only representing meat. Fig. 4 shows how the final mask is used on the CIELAB images to illustrate the distribution and variance of the L*, a*, and b* colors over the sample. Moreover L*, a*, and b* images for cooked ham, where only the background is removed, are shown. This illustration underlines the difference in consumers' view on the two types of products: For fresh meat the color of the meat excluding the fatty tissue is important, whereas for the processed meat types, the distribution of color across the entire sample is central.

Quantification The segmentation above can be utilized by finding simple statistics such as mean and variance based on the mask. For the example of veal fillets in Fig. 4 and other types of meat we find standard deviations as seen in Table 1. The corresponding values from the four sub-samplings of the colorimeter measurements are stated as well. The standard deviation of the photometric imaging model is far higher than that of the colorimeter measurements and the vision system therefore gives a better assessment of the color variation of the sample. A test for the significance level of the differences in variance is performed

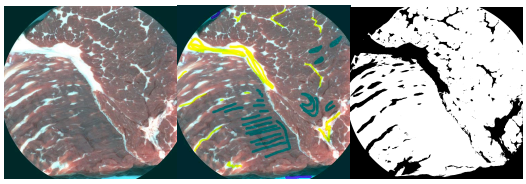

Fig. 3. Left: Pseudo RGB of round of beef. Middle: Training areas indicated. Right: Segmentation of meat and fat.

with a null hypothesis stated as $H_0 : \sigma_{PIM} = \sigma_{CM}$ vs. $H_1 : \sigma_{PIM} \neq \sigma_{CM}$. Since the number of observations is far higher for the multispectral images, the F-statistic for testing the differences in variances for the two methods is in all cases $F_{0.95,N_{PIM},N_{cm}} = 13.90$. Table 1 states the F values of the test and corresponding p values at a test level of 5%. The p values support or assumption, albeit the test values for the L* component are less significant than for the a* and b* values.

This simple analysis shows that the possibilities of working with multispectral images are far greater than the site measurements of a colorimeter. Additionally more complex segmentations can be done. For items with large color variation, e.g. minced meat or salami, a segmentation like this offers the opportunity to obtain actual measures of the color of e.g. meat and fat, in contrast to what the colorimeter can offer.

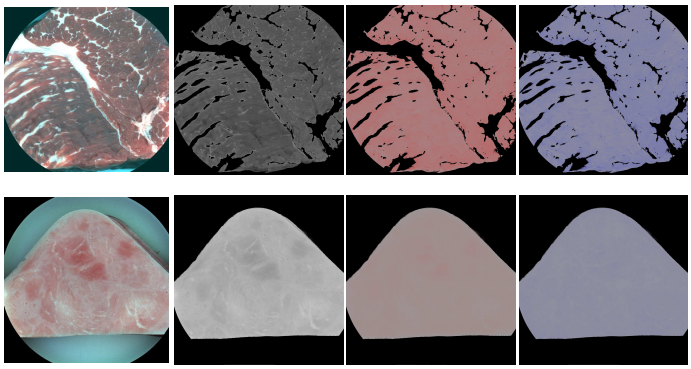

Fig. 4. Top row: Pseudo RGB, L*, a*, and b* images of the same sample as in Fig. 3 for only meat. The variance of the color components is clearly seen. Bottom row: Pseudo RGB, L*, a*, and b* images of cooked ham with background segmentation.

Table 1. Table of standard deviations for some of the 60 samples as found by the segmentation (PIM) or the colorimeter (CM)

Sample	$\hat{\sigma}_{L^*}$ (PIM)	$\hat{\sigma}_{L^*}$ (CM)	$\hat{\sigma}_{a^*}$ (PIM)	$\hat{\sigma}_{a^*}$ (CM)	$\hat{\sigma}_{b^*}$ (PIM)	$\hat{\sigma}_{b^*}$ (CM)
Round of beef	4.01	2.74	4.08	1.06	3.96	1.27
Round of pork	5.18	4.61	3.20	2.08	3.01	0.86
Filet of veal	6.5	2.07	5.11	0.50	4.61	0.62
Filet of beef	4.71	0.96	4.85	1.00	4.08	0.38
Turkey breast	5.32	3.59	2.33	0.41	2.13	0.98
	F value	p	F value	p	F value	p
Round of beef	2.36	0.13	14.87	0.002	9.55	0.006
Round of pork	1.26	0.35	2.3633	0.13	12.2624	0.004
Filet of veal	9.9537	0.04	104.6503	< 0.0001	55.3317	0.0001
Fillet of beef	24.0569	0.01	23.5502	0.0007	115.2350	< 0.0001
Turkey breast	2.1976	0.15	32.3855	0.0003	4.7136	0.03

4 Conclusion

This study has given a short introduction to the utilization of multispectral images in accordance with color assessment. The multispectral images can be used for color and color variation assessment in a precise and robust manner. Additionally it offers the opportunity for analysis enhancing the final results. The statistical analysis showed that the multispectral images gives a better view on the actual variance of the meat samples than the colorimeter.

Acknowledgments

This work was financed by the Center for Imaging Food Quality, a project funded by the Danish Council for Strategic Research (contract no 09-067039) within the Program Commission on Health, Food and Welfare.

References

1. T. Brosnan and D. Sun. Improving quality inspection of food products by computer vision – a review. *Journal of Food Engineering*, 61(1):3–16, 2004.
2. R.E. Larraín, D.M. Schaefer, and J.D. Reed. Use of digital images to estimate CIE color coordinates of beef. *Food Research International*, 41(4):380–385, 2008.
3. D.B. MacDougall and J. Hutchings. *Colour in Food - Improving Quality*. Woodhead Publishing, 2002.
4. R.A. Mancini and M.C. Hunt. Current research in meat color. *Meat Science*, 71(1):100 – 121, 2005.
5. C. H. Trinderup, A. L. Dahl, K. Jensen, J. M. Carstensen, and K. Conradsen. A comparison of meat color measurement from a chroma meter and multispectral images. Accepted for *International Conference on Near Infrared Spectroscopy 2013*, June 2013.
6. D. Wu and D. Sun. Colour measurements by computer vision for food quality control - A review. *Trends in Food Science and Technology*, 29(1):5 – 20, 2013.

Appendix C

Fresh Meat Color Evaluation Using a Structured Light System

Food Research International 71 (2015) 100–107

Contents lists available at ScienceDirect

Food Research International

journal homepage: www.elsevier.com/locate/foodres

Fresh meat color evaluation using a structured light imaging system

Camilla H. Trinderup [a], Yuan H. Brad Kim [b,*]

[a] Technical University of Denmark, Richard Petersens Plads, 2800 Kgs. Lyngby, Denmark
[b] Meat Science and Muscle Biology Lab, Department of Animal Sciences, Purdue University, West Lafayette, IN 47906, United States

ARTICLE INFO

Article history:
Received 10 December 2014
Received in revised form 21 February 2015
Accepted 28 February 2015
Available online 7 March 2015

Keywords:
Color
Meat
Colorimeter
Computer vision system
Correlation analysis
Muscle type
Aging

ABSTRACT

The objective of this study was to investigate the efficacy of a computer vision system (CVS) with structured light for meat color assessment. Three muscles (*longissimus dorsi* (LD), *semimembranosus* (SM), and *psoas major* (PM)) from eight beef carcasses were obtained at 1 day postmortem, vacuum packaged and assigned to three aging periods (9, 16, and 23 days). After aging, steaks were cut and displayed for 7 days at 3 °C under light. The surface colors were evaluated by using a Minolta, the CVS and trained color panel. In general, the CVS was highly correlated to the sensory scores, and showed an equivalent meat color assessment compared to the colorimeter. The CVS had a significantly higher correlation with the panel scores for the lighter and more color stable samples compared to the colorimeter. These results indicate that the CVS with structured light could be an appropriate alternative to the traditional colorimeter by offering improved precision and accuracy over the colorimeter.

1. Introduction

Fresh meat color is one of the most important meat quality attributes, since consumers rely on the appearance of meat to determine its freshness and wholesomeness (Mancini & Hunt, 2005). In this regard, extensive research and technological advancements have been progressed to develop more precise and consistent methods for meat color evaluation.

In general, colorimeters, such as Minolta Chroma meter and Hunter Lab MiniScan colorimeter are most widely and extensively used for the evaluation of meat color (Tapp, Yancey, & Apple, 2011). The colorimeters measure the L^* (lightness), a^* (redness), and b^* (yellowness) values in CIELAB color space by scanning a number of random spots on the meat surface as representatives of the sample. However, this type of approach also has a limitation in terms of repeatability and accuracy (Larraín, Schaefer, & Reed, 2008; Tapp et al., 2011), since 1) the meat surface is not homogeneous (containing fat and connective tissues), and 2) discoloration occurs on random areas (including the edge of meat, which is very hard to scan with colorimeters). Consequently, this could result in a biased result.

Recently, there has been a growing interest in employing a computer vision system (CVS) for meat color assessment. Several studies have exploited different computer vision systems for color measurement of fresh meat (Gerrard, Gao, & Tan, 1996; Girolami, Napolitano, Faraone, & Braghieri, 2013; Kamruzzaman, Barbin, ElMasry, Sun, & Allen, 2012; Larraín et al., 2008) and processed meat products (Valous, Mendoza, Sun, & Allen, 2009). By using a CVS, it is possible to capture the color variation across a sample, so that the possible bias due to locational variation can be avoided. The digital images captured can also be a basis for other analyses, e.g., marbling structure and fat content estimation (Jackman, Sun, & Allen, 2009; Shiranita, Hayashi, Otsubo, Miyajima, & Takiyama, 2000). Another important advantage of employing a CVS is that images can be stored and thus be evaluated even after the samples are discarded. Yagiz, Balaban, Kristinsson, Welt, and Marshall (2009) and Girolami et al. (2013) have tested the performance of the colorimeter against computer vision systems, and found that the colors returned by the CVS had a higher resemblance with the human perception of meat/food samples compared to the colors assessed by a colorimeter.

While a CVS has a great potential to be used for meat color assessment, it also has some technical limitations to overcome. For example, a CVS often employs an RGB camera for meat color evaluation, which requires consistent calibration of the instrument and illumination (Wu & Sun, 2013). Moreover, the outcome from a CVS with an RGB camera is device dependent and it can therefore be hard to translate the RGB information to other color spaces such as CIEXYZ or CIELAB.

Whenever an RGB camera is a part of a CVS, the above issues are likely present. A multispectral imaging system is one way to overcome the limitations of the RGB systems (Trinderup, Dahl, Jensen, Carstensen, & Conradsen, 2013). However, such a system is complex and the

* Corresponding author. Tel.: +1 765 496 1631.
E-mail address: bradkim@purdue.edu (Y.H.B. Kim).

http://dx.doi.org/10.1016/j.foodres.2015.02.013
0963-9969/

illumination becomes a great challenge. It would be ideal to have diffuse illumination of a sample when measuring color to limit the specular reflectance, but this could be a difficult task. A way to overcome the illumination issues could be by applying structured light to the image acquisition method. Structured light is often used in stereo optics to obtain a 3D representation of a scene (Valkenburg & McIvor, 1998). However, it can also be of use in separating the diffuse and specular components of a scene as shown by Nayar, Krishnan, Grossberg, and Raskar (2006). For a translucent material like meat, this combined approach could be a viable option, since the diffuse component depicts the true color information, whereas the specular component depicts the direct reflections of the illumination (Martelli, 2010). Therefore, it can be hypothesized that the CVS system coupled with structured light will enable data transformation of RGB to color spaces and thus precisely and accurately assess meat color. The objective of this study was to determine the efficacy of using a structured light CVS system to evaluate fresh meat color changes during retail display. To test our hypothesis, the most appropriate transformation from RGB to CIELAB was evaluated by comparing the transformed data with color data obtained by a trained sensory color panel evaluation and using a traditional colorimeter. Furthermore, three different bovine muscle samples with different aging times (*longissimus dorsi* (LD), *semimembranosus* (SM), and *psoas major* (PM)), which are known to have different color stability (Kim, Keeton, Smith, Berghman, & Savell, 2009), were evaluated to determine the efficacy of the CVS system in meat color evaluation.

2. Materials and methods

2.1. Raw materials and processing

A total of eight beef carcasses (USDA Select; A maturity; average 24 months old) were harvested at the Purdue University Meat Laboratory. Three beef muscles (LD, SM, and PM) were separated from the carcasses at 1 day postmortem, resulting in $n = 8$ replicates for each muscle type. Each muscle from each of the eight carcasses was split in three parts and vacuum packed, and randomly assigned to three different aging times of 9, 16, and 23 days postmortem. After the assigned aging time, a steak was cut from each muscle (≈2 cm), placed on a Styrofoam tray and wrapped with PVC film. The steaks were displayed under continuous fluorescent natural white light (3500 K) for 7 days at 3 °C. At display days 1, 4 and 7, a trained sensory panel ($n_{\text{panel}} = 10$) evaluated the lean meat color and discoloration scores based on the AMSA color guidelines (AMSA, 2012). The sensory color panelists, who all passed the Farnsworth–Munsell 100 Hue Test, were trained twice by exposure to images of meat samples and actual samples. Lean color was assessed using eight scale points (1 — extremely dark/brown; 8 — extremely bright red), and discoloration was evaluated in seven scale points (1 — no discoloration; 7 — total discoloration). On the days of evaluation for the trained panel, the sample colors were assessed with a Minolta CR-400 colorimeter (D65, 1 cm diameter aperture, and 2 standard observer; 3 spot measurements) and a computer vision system (CVS) employing structured light. The colorimeter calibration and measurements were performed through PVC wrap, whereas the imaging was performed without cover of the samples.

2.2. Computer vision system

The CVS consisted of an industrial RGB camera from JAI (8 M pixels) and a TI LightCrafter 3000 pico-projector. These instruments were connected to a computer running the software controlling the projections and camera trigger. The camera and projector set-up is illustrated in Fig. 1. The set-up was enclosed in a black box to keep the lighting conditions similar for all samples.

The projections used in this set-up are checkerboard patterns. For each projection, this checkerboard pattern was shifted at a fixed amount of pixels right or down. This approach results in a sequence of images,

Fig. 1. Illustration of the computer vision system set-up. Camera and projector are placed in the same height. Both instruments are connected to a computer handling projections and camera trigger.

$\boldsymbol{I}_s \in \mathbb{R}^{m \times n \times p}$, where a point in the scene is either fully lit or unlit at least once. In the fully lit points specular reflections arise. The unlit points are not totally black, since they receive light scattered underneath the surface – also denoted subsurface scattering – as illustrated in Fig. 2. This light would hold information about the color of a scene. By making some simple assumptions the diffuse and specular components in a pixel (i, j) can be found as

$$\boldsymbol{I}_{diffuse}(i,j) = \frac{1}{2} \min_n \boldsymbol{I}_s(i,j,n) \tag{1}$$

$$\boldsymbol{I}_{specular}(i,j) = \max_p \boldsymbol{I}_s(i,j,n). \tag{2}$$

This way a diffuse and a specular image of size $m \times n$ was obtained. The method is described in further details in Nayar et al. (2006). In this study checkerboard patterns with checkers of 4×4 projector pixels were applied. Since the projector had a lower resolution (480×640 pixels) than the camera (3926×2472 pixels), 45 projections were needed in order to reach a separation of the two components without artifacts.

2.2.1. Camera characterization

In order to obtain color information in CIELAB coordinates – the common color space within color measurement in foods – the RGB

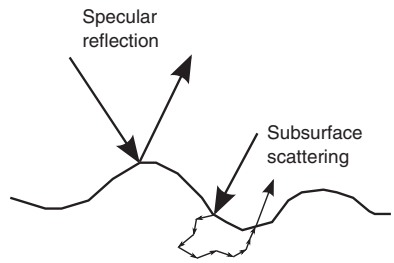

Fig. 2. Specular reflection, where the light is reflected on the sample surface. In subsurface scattering the light rays are scattered multiple times underneath the surface.

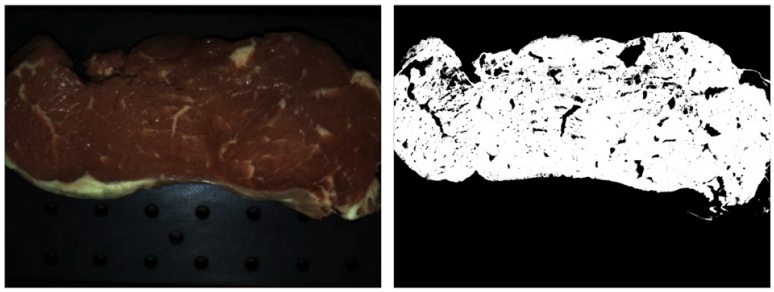

Fig. 3. Example of diffuse component and segmentation of an sample of *longissimus dorsi* at 9 days postmortem. The image was taken at day four of display.

images have to be transformed to the CIEXYZ color space and then to CIELAB values by standard formulas. The transformation from RGB to CIEXYZ was based on images of a classic color checker. Earlier studies showing the specific details of the regressions were done by Finlayson and Drew (1997) and Valous et al. (2009).

The average pixel values of each square on the color checker was extracted by means of Matlab, and stored in a 24×3 array X, with columns representing R, G, and B average values. The known CIEXYZ values under the chosen illumination of the 24 squares are stored in Y, which is also 24×3. We found the relation between the two measurements by solving

$$W_{opt} = \min_W \|Y - XW\|_2^2. \tag{3}$$

The minimization problem stated in Eq. (3) is the simplest formulation of the problem. By constraining the problem, it is possible to map the ith color exact:

$$W_{opt} = \min_W \|Y - XW\|_2^2 \quad \text{s.t.} \quad Y_{[i]} = X_{[i]}W. \tag{4}$$

Here $Y_{[i]}$ and $X_{[i]}$ refer to the ith row of the respective matrices. It would beneficial to constrain the problem for the white square of the color checker and this constrained problem would hence be denoted *white point preserving least squares* or WPPLS. Another expansion of the problem in Eq. (3) is to consider a polynomial set-up of the RGB array X, such that the ith row of X is

$$X_{[i]} = \begin{bmatrix} R_i & G_i & B_i & R_i^2 & G_i^2 & B_i^2 & 1 \end{bmatrix}, \quad i = 1, \ldots, 24. \tag{5}$$

Similar to Eq. (4) we can formulate this as a constrained problem. The two methods will be denoted polynomial least squares (PLS) and polynomial white point preserving least squares (PWPPLS).

After the transformation to the CIEXYZ color space was established, these values were mapped to the CIELAB space, by the formulas

$$L^* = 116 f(Y/Y_n) - 16 \tag{6}$$

$$a^* = 500[f(X/X_n) - f(Y/Y_n)] \tag{7}$$

$$b^* = 200[f(Y/Y_n) - f(Z/Z_n)], \tag{8}$$

with

$$f(t) = \begin{cases} t^{1/3} & \text{if } t > \left(\frac{6}{29}\right)^3 \\ \frac{1}{3}\left(\frac{29}{6}\right)^2 t + \frac{4}{29} & \text{otherwise} \end{cases} \tag{9}$$

and $(X_n, Y_n, Z_n) = (0.9504, 1.0000, 1.0889)$.

Table 1
Table ΔE^*_{ab}values of the color checker for the Minolta colorimeter, and the three different transformations of RGB to CIELAB values obtained from the CVS. The colors represent the 24 different colors of the color checker.

Minolta	WPPLS	PLS	PWPPLS	Minolta	WPPLS	PLS	PWPPLS
13.58	13.99	8.96	9.08	25.31	54.58	8.22	6.64
5.60	14.22	5.18	5.23	11.64	9.26	3.54	4.41
4.20	23.76	6.31	7.30	14.81	29.57	13.78	18.28
9.11	4.36	7.89	8.00	11.75	12.74	7.75	7.90
5.48	32.09	4.70	4.98	7.74	44.86	11.41	14.20
4.27	9.88	4.62	5.15	5.62	26.93	7.50	7.68
14.58	15.68	5.15	5.15	1.46	0.00	3.88	0.00
8.80	46.62	3.45	3.01	1.94	13.29	6.09	7.82
4.95	27.98	3.10	3.53	1.53	18.65	3.70	3.37
18.49	35.04	4.32	4.56	2.30	14.04	8.57	9.69
13.53	5.85	1.43	2.52	6.81	13.75	4.99	5.05
11.60	13.67	13.22	12.34	14.27	11.80	14.94	16.64

WPPLS: White point preserving least squares.
PLS: Polynomial least squares.
PWPPLS: Polynomial white point preserving least squares.

Table 2
Overall correlations of color data and sensory scores for the different transformations of the image data. All values are statistically different from 0.

Method	σ^2 (chroma and lean color)	σ^2 (hue angle and discoloration)
Colorimeter	0.8107	0.9299
WPPLS	0.8803	0.9382
PLS	0.8992	0.7437
PWPPLS	0.8911	0.7187

WPPLS: White point preserving least squares.
PLS: Polynomial least squares.
PWPPLS: Polynomial white point preserving least squares.

The three different approaches for transformation from RGB pixel info to CIELAB was investigated by means of a color checker. Differences between the ground truth value of the color checker and the measured color value was evaluated by the ΔE^*_{ab} value. This value is given as

$$\Delta E^*_{ab} = \sqrt{\left(L_{cc,i} - L_i\right)^2 + \left(a_{cc,i} - a_i\right)^2 + \left(b_{cc,i} - b_i\right)^2} \quad (10)$$

for the ith color and expresses the total color difference for one measurement.

Even though the transformations were based on RGB images that were fully lit, these were applied to the RGB images of the diffuse components. Since the specular component holds very little color information no significant information should be lost by this approach.

2.3. Feature extraction

When extracting color from images it is important that only pixels representing the subject of interest are taken into account. Therefore a segmentation of lean meat, fat and background was performed. This is done by defining training areas for the three classes – background, lean meat, and fat – in the RGB images. From these trainings areas a model for linear discriminant analysis was built — for further information on the linear discriminant analysis see Johnson, Wichern, and Education (1992). The model uses the prior distribution of the three classes, p_i with $i = \{1, 2, 3\}$, and the frequency function of the class, f_i. For an observation x, a discriminant score $S_i = p_i f_i(\boldsymbol{x})$ is found. x belongs to the class i that gives the maximum discriminant score. Performing this discrimination pixel-wise it was possible to segment the image and have a mask representing only the lean meat. An example is seen in Fig. 3. Based on the masks found by the segmentation and the transformation to the CIELAB color space it is possible to extract several features from the images. The average CIELAB values, L^* (lightness of sample), a^* (redness of sample), and b^* (yellowness of sample), of lean meat were found, as well as the parameters chroma $\left(C^*_{ab} = \sqrt{(a^*)^2 + (b^*)^2}\right)$ and hue angle (h^*_{ab} = arc tan(b^*/a^*)) were found. These two parameters have previously shown to correlate well with sensory evaluations.

2.4. Statistical analysis

The features extracted were used in the evaluation of the two instruments' ability to evaluate color. The comparison was based on different statistical tools. First of all an ANOVA (Analysis of Variance) was performed. After establishing the effects and their interaction a correlation analysis established the performance of the two instruments.

The model for the ANOVA was formulated as

$$y_{jkl} = \mu + a_j + m_k + d_l + am_{jk} + ad_{jl} + md_{kl} + \varepsilon_{jkl} \quad (11)$$

with the effects a_j: aging time ($j \in \{1, 2, 3, 4\}$), m_k: muscle type ($k \in \{1, 2, 3\}$), d_l: days of display ($l \in \{1, 4, 7\}$), and an error term ε_{jkl}. y can represent the color scores by the panel, or the color parameters from either the colorimeter or the CVS. The model was established to determine if there would be any significant interactions of the different effects.

Correlation comparisons were used for evaluating the performance of the computer vision system and the colorimeter. Muscle type, and display day effects were considered. The chroma and hue angle values will be considered as predictors for lean meat color and discoloration respectively.

3. Results and discussion

3.1. Color transformations

The performance of the three different transformations considered in Eqs. (4) and (5), is summarized in Table 1. In the same table the color evaluation of the colorimeter is also summarized. The ΔE^*_{ab} value (the difference between the ground truth of the color checker and the measured color) of the colorimeter was 9.14 as an average, a minimum of 1.46 (the white square), and a maximum value of 25.31 (blue square). The WPPLS transformation led to a higher average difference of 20.52 and due to the constraint a minimum value of 0 and maximum of 54.58. The PLS and PWPPLS performed well with average ΔE^*_{ab} values around 7, and maximum values of 14.94 and 18.28 respectively.

The color checker is an opaque object, which has significantly different absorption and scattering properties than a translucent material like meat. Considering the numbers in Table 1, one would judge that the PLS and PWPPLS methods would be better at predicting color values, but based on the very different material properties of the color checker and meat, the optimal transformation for the RGB was chosen by considering the correlation of the meat colors returned by the three methods (WPPLS, PLS, and PWPPLS) with the sensory panel scores. The transformations considered in this study had less terms in the regression matrix than the study performed by Valous et al. (2009), and the ΔE^*_{ab} values obtained were hence also higher. However, the ΔE^*_{ab} values are comparable to those of the colorimeter, and the transformations considered should be acceptable.

Table 3
Color attributes acquired from the CVS and the colorimeter for all samples. The three components of the CIELAB space are considered and the chroma (c) and hue (h) angle values are considered.

	Muscle					
	Longissimus dorsi		*Semimembranosus*		*Psoas major*	
Instrument	CVS	Colorimeter	CVS	Colorimeter	CVS	Colorimeter
L^*	49.7 ± 5.3	44.3 ± 1.5	49.6 ± 4.7	45.9 ± 2.4	46.7 ± 3.9	43.5 ± 3.6
a^*	13.8 ± 3.3	17.1 ± 2.3	10.9 ± 4.5	16.8 ± 4.1	8.4 ± 4.3	14.6 ± 4.4
b^*	14.2 ± 1.9	8.2 ± 0.9	13.4 ± 1.7	9.7 ± 1.2	12.7 ± 1.1	9.1 ± 0.8
h	19.8 ± 3.5	18.9 ± 2.4	17.6 ± 3.7	19.5 ± 3.9	15.6 ± 3.1	17.3 ± 3.9
c	46.4 ± 4.3	25.7 ± 1.7	53.1 ± 11.3	30.8 ± 5.5	58.8 ± 11.7	33.3 ± 7.4

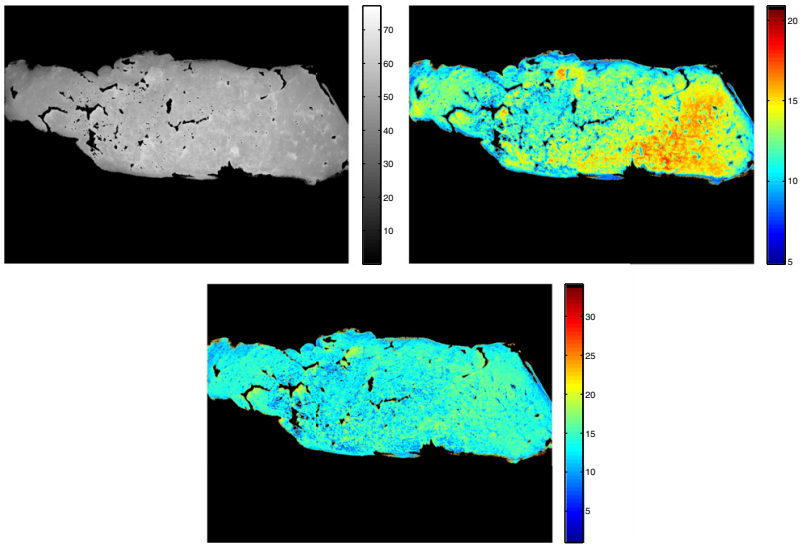

Fig. 4. An example of a highly discolored sample (*psoas major*) at the seventh day of display. Top-left: L^* values. Top-right: a^* values. Bottom: b^* values. The variation of the a^* parameter clearly indicates a progression of discoloration during display.

3.2. Image features

The linear discriminant analysis was applied to the RGB and segmentations as shown in Fig. 3 were obtained. The RGB image of one of the acquired samples is seen along with its segmentation. Using the transformations found in the previous section, it was possible to extract a mean pixel intensity for the three color components, L^*, a^*, and b^*, and other color attributes, such as hue angle and chroma values. In order to establish the most suitable transformation for the meat samples in the current study, the crude correlations with the sensory panel scores were evaluated as summarized in Table 2. The chroma and hue angle values obtained from the colorimeter had a crude correlation with the lean color scores of 0.81 and with discoloration scores of 0.93 respectively. The average L^*, a^*, b^*, chroma (c) and hue (h) angle values of lean meat for the three different transformations were found. The transformations all had crude correlations close to 0.89 when chroma values obtained from the CVS were related to lean meat color scores. Relating the hue angle values to the discoloration scores, the WPPLS transformation showed a significantly higher correlation than the two other transformations, suggesting that this transformation would be the most applicable for converting RGB image data from the CVS to the CIELAB color space when a translucent material like meat is concerned as discussed in the previous section.

Table 3 summarizes the first and second order statistics of the color values obtained when applying the WPPLS transformation to the RGB images. The comparable values returned by the colorimeter were also observed. A general tendency of the L^* values being at a similar level between the two instruments was observed. The a^* values were generally higher for the colorimeter, whereas the opposite was observed for the b^* values. The statistics showed that there was no difference in how the two instruments assessed the L^* component, but that the a^* component was generally lower for the CVS and the b^* component was generally higher for the CVS. The difference in a^* value could be related in part to the fact that the color measurement by the CVS was an average of pixel values. As seen in Fig. 4 the a^* values of highly discolored pixels were actually negative and therefore represent a slightly green color in the CIELAB color space. Nevertheless, these negative pixels could impact the average value of a sample. Hence the lower average a^* values from the CVS compared to the colorimeter would not necessarily be an indication that the CVS actually measured the component lower, but reflected that the CVS assessed the a^* component at a broader range than the colorimeter. This speculation could also be supported

Table 4
ANOVA for the model in Eq. (11). For summary, the resulting F- and p-values are shown.

Effect	DF	$F_{leancolor}$	$p_{leancolor}$	$F_{c,colorimeter}$	$p_{c,colorimeter}$	$F_{c,CVS}$	$p_{c,CVS}$
a	2	2.93	0.055	9.37	0.0001	1.54	0.217
m	2	158.83	<0.0001	43.30	<0.0001	145.01	<0.0001
d	2	181.04	<0.0001	427.98	<0.0001	435.01	<0.0001
am	4	2.63	0.035	0.20	0.938	2.32	0.059
ad	4	2.51	0.043	3.18	0.0197	3.90	0.005
md	4	6.244	<0.0001	16.44	<0.0001	7.66	<0.0001

Effect	DF	$F_{discoloration}$	$p_{discoloration}$	$F_{h,colorimeter}$	$p_{h,colorimeter}$	$F_{h,CVS}$	$p_{h,CVS}$
a	2	5.09	0.007	2.09	0.1262	3.79	0.0242
m	2	113.35	<0.0001	103.70	<0.0001	99.97	<0.0001
d	2	283.92	<0.0001	153.04	<0.0001	213.49	<0.0001
am	4	3.00	0.0198	1.69	0.154	0.49	0.740
ad	4	11.20	<0.0001	1.62	0.170	0.85	0.496
md	4	28.42	<0.0001	30.09	<0.0001	20.45	<0.0001

a: aging.
m: muscle type.
d: display day.
am: aging × muscle type.
ad: aging × display day.
md: muscle type × display day.

Table 5
Correlations split on days of display. Lean meat color scores were investigated with respect to chroma (c) value and discoloration scores were correlated with hue (h) angle values.

Days of display	Lean color			Discoloration		
	Colorimeter (c)	CVS (c)	p^*	Colorimeter (h)	CVS (h)	p^*
1	0.570	0.843	<0.0001	0.394	0.486	0.250
4	0.797	0.941	<0.0001	0.859	0.870	0.406
7	0.844	0.748	0.060	0.925	0.900	0.186

* p-Value of test for difference in correlation coefficient.

Table 6
Correlations split on muscle types. Lean meat color scores were investigated with respect to chroma (c) values, whereas discoloration scores were correlated with hue (h) angle values.

Muscle type	Lean color			Discoloration		
	Colorimeter (c)	CVS (c)	p^*	Colorimeter (h)	CVS (h)	p^*
Longissimus dorsi	0.727	0.753	0.364	0.407	0.811	<0.0001
Semimembranosus	0.918	0.896	0.238	0.905	0.960	0.005
Psoas major	0.922	0.890	0.142	0.954	0.912	0.026

* p-Value of test for difference in correlation coefficient.

by the fact that the difference in average a^* for the two instruments was increased as the color stability of the muscle decreased.

3.3. Color variation analysis

In order to establish the sources of variation in the data, the model in Eq. (11) was applied to the panel scores (lean meat color and discoloration), and chroma and hue angle values from the two instruments. The analyses of lean meat color scores and chroma parameters were considered first. For the lean meat color scores, the significant contributors to the variance are days of display, muscle type, and their interaction. The F-values of the single effects were much higher than the interaction (Table 4). The variation of the discoloration scores showed days of display as the most dominant effect, followed by the muscle type effect. The interaction between muscle type and days of display was also significant. Significant aging effect on discoloration was also observed ($p = 0.007$). The observed main effects of muscle type and display day on color and color stability are well understood (Kim et al., 2009; McKenna et al., 2005). For both instruments the variance structure reflected almost the same structure, except that the days of display effect had a higher F-value than the muscle type effect. For the hue angle values (indication of discoloration) assessed by the two instruments, the two dominant effects were again days of display and muscle type. The aging effect was not significant for the colorimeter measurements, but for the CVS it was at a 2.5% significance level, which was in agreement with the discoloration result obtained from the sensory panel evaluation. More detailed comparison between the CVS and colorimeter in meat color assessment based on the correlations of the instrumental color parameters to the scores of the sensory panel is discussed in the next section.

3.4. Instrument comparison

Based on the statistical result of the ANOVAs for each of the color assessment parameters — panel scores and instrumental measurements, the CVS and the colorimeter were equally good at assessing the variance in meat color as represented by the panel scores. A further analysis correlating the panel scores to the instrumental assessment again showed that the two instruments had similar performance. In some cases the CVS even performed better than the traditional colorimeter. For the chroma values and lean meat color scores, it was observed that the correlations of the colorimeter increase with the number of display days (Table 5). Conversely, for the CVS, there was a strong correlation at day 1 till day 4, and then decreased at day 7. The test for difference in correlation coefficients showed that the CVS had a significantly higher correlation with the panel scores at days 1 and 4 than the colorimeter. For the correlations of discoloration scores and the hue angle values from the two instruments, there was an increase in the number of display days. No significant difference between the correlations of the two instruments was observed for the discoloration scores.

Considering the data for each muscle type separately showed different patterns of correlations (Table 6). For the correlations with lean meat color scores the two instruments showed similar correlation coefficients. Moreover it is important to observe that the correlation for the lighter LD muscle was lower than that of the two other muscles. A difference in correlation coefficient was seen for the LD muscle when hue angle and discoloration scores were considered. In this case the colorimeter returned values, which were less correlated with the panel scores.

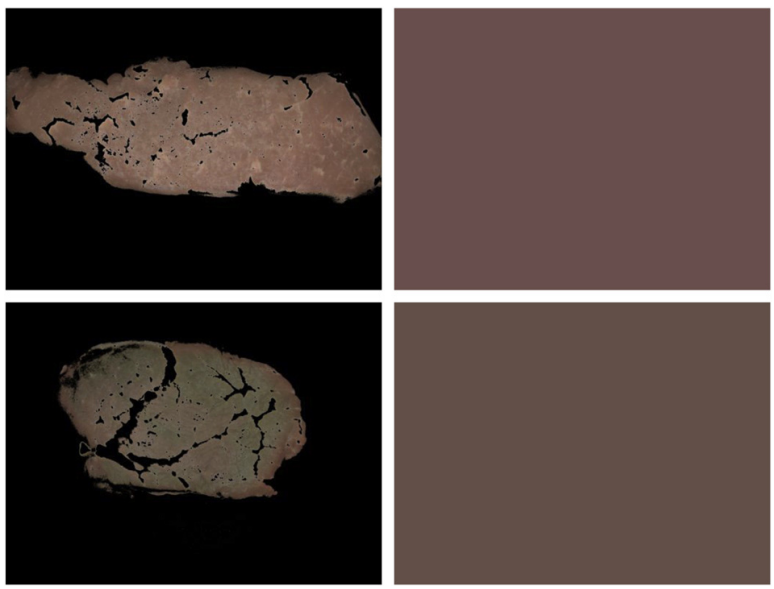

Fig. 5. Top-left: Fresh sample with almost no discoloration. Top-right: The sRGB color returned by the colorimeter for the sample top-left. Bottom-left: Highly discolored sample from day 7 of display. Bottom-right: The sRGB color returned by the colorimeter of the sample from day 7 (bottom-left).

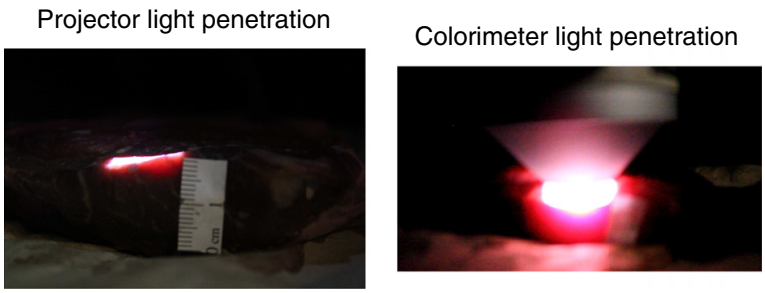

Fig. 6. Illustration of difference in penetration depth for the two color measurement instruments. Left CVS and right the colorimeter. The flashing light of the colorimeter clearly penetrates the whole sample, whereas the light of the projector only appears in the top surface of the meat sample.

For the semi-color stable SM muscle, there was also a significant difference for the two instruments ($p = 0.005$).

To summarize the results of the correlation analysis, lean meat color scores were well correlated for both instruments when the darker samples at display days 4 and 7 were considered, as well as the darker muscle type, SM and PM. These indicate that the overall brighter red samples at display day 1, and to some extent the color of the lighter LD muscle, were less well assessed by the instruments. The CVS performed better than the colorimeter in these cases. Discoloration scores seemed to be harder to capture for the colorimeter than the CVS for the color stable muscle like LD. Both instruments were good at evaluating the discoloration scores of the darker samples. In this setting, it is important to mention that previous studies found that the color assessment abilities of the colorimeter did not always reflect the human perception of color (Girolami et al., 2013; Yagiz et al., 2009) and that the instrument especially had difficulties when lighter samples such as pork, turkey, and salmon fillets were considered (Trinderup et al., 2013). The results from the current study also showed the similar trends as discussed above.

3.5. Reflectance properties of meat

Fig. 5 shows a sRGB image of two samples from the study — a fresh sample from day 1 and a highly discolored sample from day 7. The sRGB images were generated from the pixel wise CIELAB measurements by the method described in Section 2.2.1. The illustration also shows a square indicating the sRGB color returned by the colorimeter. The strength of the CVS was clearly seen from these images. The colorimeter was not capable of capturing the color variation across the discolored sample, whereas the image clearly showed what areas were discolored. One possible explanation for the difference in color assessment ability could be the penetration depth of the illumination light, as pointed out by Girolami et al. (2013). In Fig. 6 the difference was illustrated for the two instruments in this study. It was clearly seen how the flash of light in the colorimeter, penetrated all the way through an $\approx$2 cm high sample, whereas the projector illumination only traveled a few millimeters down the sample. Since the red color from oxymyoglobin was mostly present at the surface of the sample, the light penetration of the colorimeter could lead to unwanted contributions. Another closely related explanation or contributor to the difference in color assessment abilities, could be the fact that meat is a translucent material, where subsurface scattering occurs. This issue was addressed in Section 2.2. The translucency of the meat samples and subsurface scattering are two sides of the same coin so to speak. When the aperture of the colorimeter is small, the subsurface scattering can lead to rays reflected outside the instrument opening and they do not contribute to the color measurement. This shows that the different apertures of the color assessment instrument can impact the result of color attributes (Tapp et al., 2011). As the results show, the CVS employing structured light to extract the diffuse component measured meat color at the same level as the traditional colorimeter, and in some instances, it actually had a better performance than that of the colorimeter as it related more closely to the visual judgments by a trained panel.

4. Conclusion

The results of the current study indicate that the CVS employing structured light to obtain the diffuse component of a sample showed an equivalent color assessment of meat with different color stability with different aging times compared to the colorimeter. In fact, in some instances, it actually had a better performance than the colorimeter as it related more closely to the visual evaluation of a trained panel. Taken together, it can be suggested that the CVS employing structured light could be an appropriate alternative to the traditional colorimeter by offering improved precision and accuracy over the colorimeter. Further studies on the data from the CVS employing structured light, could be an analysis involving image registration over display time. This would result in an analysis of spatial discoloration over time.

Acknowledgment

This work has been financed by the Center for Imaging Food Quality, a project funded by the Danish Council for Strategic Research (contract no 09-067039) within the Program Commission on Health, Food and Welfare to support the first author's, Camilla Trinderup, visiting research travel to Purdue University. This project was supported by a Start-up Funding from the College of Agriculture, Purdue University. The authors thank Danyi Ma, Brandon Meyers, Juhui Choe, and the Purdue Meat Lab staff for the sample and data collection, and the sensory color panel at the Department of Animal Sciences at Purdue University for the color evaluation.

References

AMSA (2012). *American meat science association committee on guidelines for meat color evaluation.*

Finlayson, G. D., & Drew, M. S. (1997). Constrained least-squares regression in color spaces. *Journal of Electronic Imaging, 6*(4), 484–493.

Gerrard, D., Gao, X., & Tan, J. (1996). Beef marbling and color score determination by image processing. *Journal of Food Science, 61*(1), 145–148.

Girolami, A., Napolitano, F., Faraone, D., & Braghieri, A. (2013). Measurement of meat color using a computer vision system. *Meat Science, 93*(1), 111–118.

Jackman, P., Sun, D. -W., & Allen, P. (2009). Automatic segmentation of beef longissimus dorsi muscle and marbling by an adaptable algorithm. *Meat Science, 83*(2), 187–194.

Johnson, R. A., Wichern, D. W., & Education, P. (1992). *Applied multivariate statistical analysis, Vol. 4*, Englewood Cliffs, NJ: Prentice Hall.

Kamruzzaman, M., Barbin, D., ElMasry, G., Sun, D. -W., & Allen, P. (2012). Potential of hyperspectral imaging and pattern recognition for categorization and authentication of red meat. *Innovative Food Science & Emerging Technologies, 16*, 316–325.

Kim, Y. H., Keeton, J. T., Smith, S., Berghman, L. R., & Savell, J. W. (2009). Role of lactate dehydrogenase in metmyoglobin reduction and color stability of different bovine muscles. *Meat Science, 83*(3), 376–382.

Larraín, R., Schaefer, D., & Reed, J. (2008). Use of digital images to estimate CIE color coordinates of beef. *Food Research International*, *41*(4), 380–385.
Mancini, R., & Hunt, M. (2005). Current research in meat color. *Meat Science*, *71*(1), 100–121.
Martelli, F. (2010). *Light propagation through biological tissue and other diffusive media: Theory, solutions, and software*. SPIE.
McKenna, D. R., Mies, P. D., Baird, B. E., Pfeiffer, K. D., Ellebracht, J. W., & Savell, J. W. (2005). Biochemical and physical factors affecting discoloration characteristics of 19 bovine muscles. *Meat Science*, *70*(4), 665–682.
Nayar, S. K., Krishnan, G., Grossberg, M. D., & Raskar, R. (2006). *Fast separation of direct and global components of a scene using high frequency illumination. ACM Transactions on Graphics (TOG), Vol. 25.* (pp. 935–944). ACM.
Shiranita, K., Hayashi, K., Otsubo, A., Miyajima, T., & Takiyama, R. (2000). Grading meat quality by image processing. *Pattern Recognition*, *33*(1), 97–104.
Tapp, W. N., III, Yancey, J. W. S., & Apple, J. K. (2011). How is the instrumental color of meat measured? *Meat Science*, *89*(1), 1–5.
Trinderup, C. H., Dahl, A. L., Jensen, K., Carstensen, J. M., & Conradsen, K. (2013). *A comparison of meat color measurements from a colorimeter and multispectral images. Proceedings of the 16th International Conference on Near Infrared Spectroscopy 2013, Vol. 1*.
Valkenburg, R. J., & McIvor, A. M. (1998). Accurate 3D measurement using a structured light system. *Image and Vision Computing*, *16*(2), 99–110.
Valous, N. A., Mendoza, F., Sun, D. -W., & Allen, P. (2009). Colour calibration of a laboratory computer vision system for quality evaluation of pre-sliced hams. *Meat Science*, *81*(1), 132–141.
Wu, D., & Sun, D. (2013). Colour measurements by computer vision for food quality control — A review. *Trends in Food Science and Technology*, *29*(1), 5–20.
Yagiz, Y., Balaban, M., Kristinsson, H., Welt, B., & Marshall, M. (2009). Comparison of Minolta colorimeter and machine vision system in measuring colour of irradiated Atlantic salmon. *Journal of the Science of Food and Agriculture*, *89*(4), 728–730.

Appendix D

Longitudinal Studies of Multispectral Images of Salami

Longitudinal studies of Multispectral Images of Salami

Camilla H. Trinderup, Anders Dahl, Flemming Møller and Knut Conradsen

December 23, 2014

Abstract

Image analysis tools applicable for the analysis of fermentation stages if sausages are presented. The difference in chilled and non-chilled samples is assessed by a statistical analysis of image features relating to size, color, and texture of the sausage over time. The feature analyses show that there are statistically significant difference between the two groups, but in the case of color measurements the difference will be difficult to asses for a sensory panel. The results indicate that it might be possible to stall the fermentation such that a sensory panel can evaluate all fermentation stages at once, yet still in a reliable manner.

1 Introduction

The visual changes during the fermentation process of a salami occur due to the evaporation and is expressed by a shrinkage of the salami diameter, a graduate color change and a texture change. In this study we show how analysis of multispectral images of salamis can be an objective tool for quantifying the changes. As an example of the usefulness of the image analysis tools applied differences of chilled and non-chilled samples will be investigated.

Fermentation is an old method for preservation of food products and to this day it is still used in developing countries as a cheap and reliable preservation method (Leroy and De Vuyst, 2004). In the Western world fermented products such as cheese, yoghurt, sourdoughs, and sausages represent gastronomic qualities and genuine products. For bulk production of fermented food products it is necessary that the fermentation process is controlled and that the final products meet some specified standards, so the products' quality is maintained for the returning costumer. Starter cultures have to a great extent facilitated this possibility. These cultures are lactic acid bacterias (LAB) chosen selectively and added to the raw material to accelerate and control the fermentation process. When starter

cultures are added to ferment sausages, they contribute to the texture, aroma, and flavor (Leroy, Verluyten, and De Vuyst, 2006). Moreover, the LAB strains possess anti-microbial effects and prolong shelf-life. Starter cultures is a natural method for obtaining wanted product properties, which fits well with the consumer and society trends .

It is important to be able to characterize the effect of different starter cultures - i.e. how do they react with and influence the raw materials under the same production conditions? This will help in facilitating the understanding of the cultures, and also contribute to a product with consistent properties regarding texture, color and flavor. A sensory panel can be a strong tool to precisely determine quality parameters (van Kleef, van Trijp, and Luning, 2005), but variations in their assessment can occur, especially when the same product is assessed at different time points. This is of particular relevance for fermented products like salamis, where the sausage is developed over time. In order to avoid such variations it would be advantageous to present all fermentation stages of the salamis to the sensory panel at once. Having all fermentation stages could be achieved by having started salami production at different time points, but this can cause variations between batches, which should also be avoided. Instead it could be beneficial to have a method for stopping or pausing the fermentation process, such that a sensory panel could be exposed to all fermentation stages at the same trial and perform a more equal assessment of the salamis.

In this study we present some tools for processing and analyzing multispectral images of salamis with the goal of determining if there is a difference of chilled and non-chilled samples. A vision system is a great option for a comparison study like this, since the illumination is consistent across acquisition days. Hence we will have equal assessment properties of the samples across fermentation stages.

Image analysis has previously been used in assessment of color of meat products. Several studies describe how a computer vision system and subsequent image analysis can be used in the process of describing various meat products (Valous, Mendoza, Sun, and Allen, 2009; Chmiel, Słowiński, and Dasiewicz, 2011; Mendoza, Valous, Allen, Kenny, Ward, and Sun, 2009). The studies relate to both color and texture of the products. Mendoza, Dejmek, and Aguilera (2006) review how different vision systems are employed to assess color and other attributes of agricultural foods. Image analysis has also proven useful in the analysis of ripening stages for fruits and vegetables (Mendoza and Aguilera, 2004; Xing and De Baerdemaeker, 2005; Steinmetz, Roger, Molt , and Blasco, 1999), identification of previously frozen products (Sun and Brosnan, 2003; Sharifzadeh, Clemmensen, Løje, and Ersbøll, 2013), and spoilage detection in meat (Dissing, Papadopoulou, Tassou, Ersbøll, Carstensen, Panagou, and Nychas, 2013). Work presented in this paper is inspired by the studies in Møller, Larsen, and Carstensen (2012).

In this paper we have quantified appearance features related to size, color, and texture of salami slices using image analysis. Our results show subtle differences between chilled and non-chilled samples. In order to determine the magnitude and cause of these differences

we have employed a statistical variance component model. Before describing our analysis we will begin by describing the experiment and data collection followed by describing the computation of the image feature. The image analysis tools applied in this study should be considered as tools applicable for extracting general features descriptive of fermented salamis.

2 Materials and methods

During the fermentation process of a salami the meat changes color and the salami also shrinks in circumference. Moreover, the texture or firmness of the product also changes. We capture this change by extracting features from the multispectral images and investigated if the change was different for chilled and non-chilled samples.

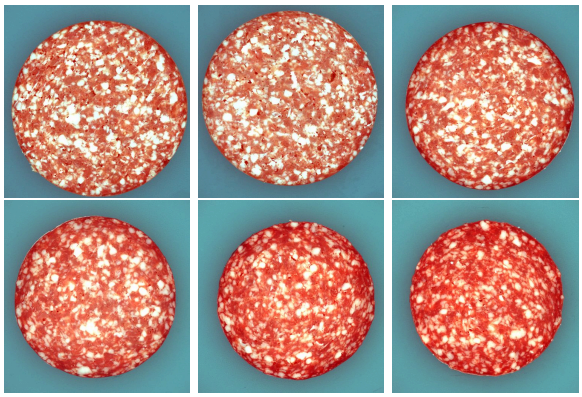

Figure 1: Fermentation process for one type of salami at day 2, 3, 9, 14, 21, and 42 after making (ordered from upper left to lower right). These images are false color composite based on three spectral bands of the image (660 nm, 470 nm, and 435 nm).

2.1 Samples and Instrument

The rate of the changes during the fermentation process is determined by factors like fermentation culture, smoke time, fat and meat content, etc. In this study we will only consider four different recipes of starter cultures, and keep all other factors constant.

We study samples from specific days (2, 3, 9, 14, 21 and 42) after fermentation start. On these days, two samples of each recipe were taken from the smoker. From one sausage three

Table 1: Schematic view of the samples involved in the experiment, and average sensory panel values pr. fermentation day.

Days of fermentation	Recipe	No. slices/sausage	Days at $-2°$C
2	1-4	3	0
2 - C	1-4	3	39
3	1-4	3	0
3 - C	1-4	3	38
9	1-4	3	0
9 - C	1-4	3	32
14	1-4	3	0
14 - C	1-4	3	27
21	1-4	3	0
21 - C	1-4	3	20
42	1-4	3	0

slices of ~ 2 cm were cut and imaged with the multispectral imaging system. The other sausage was placed in the chiller at $-2°$C until day 42. At day 42 the chilled samples were taken out of the chiller and put in the refrigerator until they had a temperature of ???°C. Just as for the non-chilled samples, the chilled samples were now sliced and imaged with the VideometerLab. The chilled samples have been stored at $-2°$C for different number of days when they are imaged.

We have 4 different types of recipes, 3 slices at each day, and 6 observation days. Since the day 42 samples have not been chilled, we only have one 'set' from this day, and we reach a total of 44 different samples, and $n = 132$ observations in total. Table 1 gives a schematic view of the samples in the experiment.

In this study we employ the multispectral imaging system VideometerLab that depicts objects with a diameter of up to 10 cm using wavelength specific diffuse illumination, making it ideal for salami slices. The resulting images are 2056×2056 pixels with a pixel size of about 45μm. The instrument has 19 spectral bands - 12 visible and 7 near-infrared bands.

2.2 Image analysis

Figure 1 shows images of salamis fermented for 2, 3, 9, 14, 21, and 42 days, and the careful reader will see a change in width, color, and change in image texture. This section will present tools that are capable of capturing these changes from the image data. Before we can extract features from the images, it is necessary to segment the images, such that

the information we extract only represent the sample. Figure 2 presents the steps in the analysis - all steps will be described thoroughly in the rest of this section.

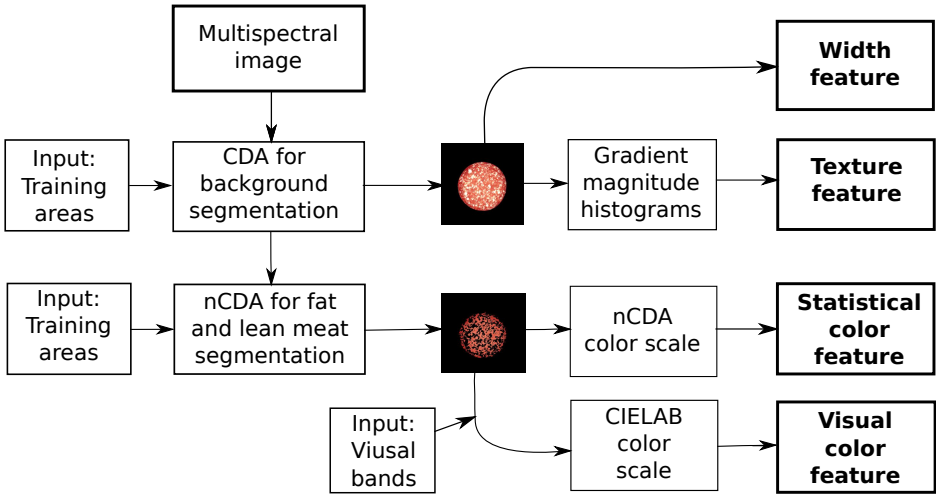

Figure 2: Outline of the approach for feature extraction from the multispectral images.

2.2.1 Segmentation

In order to segment the images into background, meat, and fat, we will use canonical discrimination analysis (CDA). The CDA is a supervised method using training areas of the k wanted classes in setting up the discriminator. More specifically we seek a discriminator, $\boldsymbol{y} = \boldsymbol{d}^{\boldsymbol{T}}\boldsymbol{x}$, that maximizes the between variation among ($\boldsymbol{B}$) relative to the variation within classes ($\boldsymbol{W}$). This is done by maximizing the Rayleigh coefficient given by

$$R(\boldsymbol{d}) = \frac{\boldsymbol{d}^{\boldsymbol{T}}\boldsymbol{B}\boldsymbol{d}}{\boldsymbol{d}^{\boldsymbol{T}}\boldsymbol{W}\boldsymbol{d}}. \tag{1}$$

We obtain $\boldsymbol{d}$ as the generalized eigenvectors of $\boldsymbol{B}$ with respect to $\boldsymbol{W}$. We may obtain $k-1$ solutions, uncorrelated and with decreasing discriminative power.

In this study we shall use the so-called normalized CDA (nCDA) by standardizing the canonical discriminant scores $\boldsymbol{y}$ by subtracting the mean and dividing by the standard deviation:

$$\hat{\boldsymbol{y}} = \frac{\boldsymbol{y} - \bar{\boldsymbol{y}}}{\boldsymbol{s_y}}. \tag{2}$$

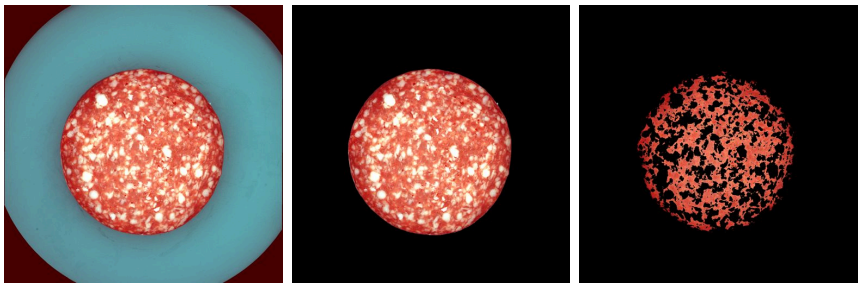

Figure 3: Pseudo RGB image of sample from day 14 with background and meat and fat segmentations.

This approach will ensure canonical discriminant function scores centered around zero, and it will be easy to set a threshold value for obtaining the segmentation,e.g. at zero.

The first step in the segmentation is to separate salami and background by CDA. Training areas in the background are defined as one class and salami as the second class. The model for segmentation is based on only one training sample, so even though it is a supervised method, the manual work is limited to finding few training areas. Since the variation in the background is relatively small compared to the larger variation within meat and fat in the salami, the method still discriminates well.

Second step in the segmentation is the separation of meat and fat areas. Training areas for the two classes are again found from a day 9 sample, such that the training areas reflect the variation that is present across all fermentation stages. In this segmentation we obtain good results by performing a spectral pretreatment, where some (noise) artifacts are removed and the segmentation of fat and mat is improved. The pretreatment is done pixel-wise, such that a pixel in the pretreated image, $\boldsymbol{P}_i$ in pixel (x, y) is given by

$$\boldsymbol{P}_i(x, y) = \frac{\boldsymbol{I}_i(x, y)}{\boldsymbol{I}_j(x, y)}. \tag{3}$$

This equation expresses the pretreatment of the i'th band with the j'th band. The improvement in the segmentation can be directly related to an increase in the value of the Rayleigh coefficient in (1). The salami images showed an increase in Rayleigh coefficient when the pixel-wise division was done with the third spectral band (435 nm). This band was left out in the further segmentation. An example of the final segmentations is seen in Figure 3.

2.2.2 Width of salami

From the segmentations of background and salami the width of the salami is found in the horizontal direction. In case the structure of the salami is influenced by the chilling process this could lead to a change in this physical parameter.

2.2.3 Statistical Color Information

During the fermentation process there is a change in color especially for the meat parts of the salami – see Figure 1. The change in color starts from the rim of the salami. In order to capture the variation in color across the samples we define a meat color scale based on an nCDA analysis using two training areas from non-chilled samples at days 2 and 42, to represent the extreme colors. Subsequently all samples are mapped to the obtained nCDA space. Since the model is trained on samples from days 2 and 42, negative values of the nCDA meat color scale reflects fresher meat, whereas the positive values represents the darker, fermented meat. It is important to mention that the nCDA is trained on the non-chilled samples, so the chilling process is not already accounted for in the analysis of the color feature, i.e. chilled and non-chilled samples will be mapped to the same space.

The loadings for each of the 19 spectral bands are summarized in Figure 4. In general the longer wavelengths, red (645 - 660 nm) and NIR (890 - 970 nm), are dominant, which reflects that color changes mainly occur in the red meat part.

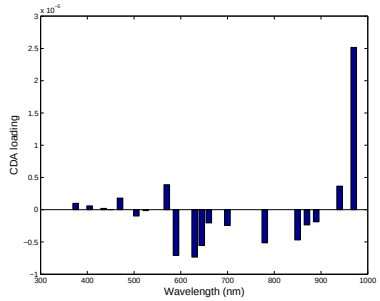

Figure 4: CDA loadings for the statistical meat color scale.

Applying the trained nCDA color model to the masked multispectral images gives images representing the statistical color scale as the ones seen in Figure 5. An assumption is that the fermentation occurs evenly from the rim of the salami. Hence we extract the average pixel value in circles at predefined radii from the center of the salami. The maximum radius considered, r_{max}, is defined as the average width across all samples. For the samples that

have a maximum radius smaller than r_{max}, the missing pixel averages will be found by extrapolation.

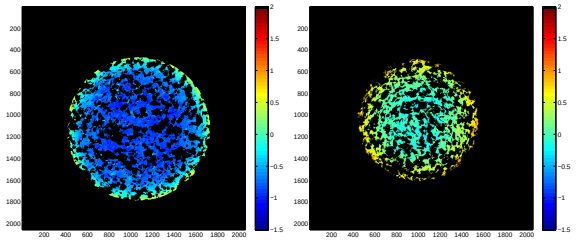

(a) Sample day 2. (b) Sample day 42.

Figure 5: nCDA meat color scale. The darker blue color represents fresher meat, whereas the yellow and orange colors are darker red, fermented meat.

2.2.4 CIELAB Color Information

The above method where all spectral bands are employed to obtain a general measure of color change is good for statistical analysis and identification of even subtle differences. In food research it is common to measure color in the CIELAB color space since it relates well to human perception of color. We can convert the pixel-wise multispectral information to L^*, a^*, and b^* pixel values by a *photometric imaging model*. The details of the transformation from multispectral images to CIELAB is e.g. described by Trinderup, Dahl, Jensen, Carstensen, and Conradsen (2015), but in short consists of fitting the 12 visual spectral bands of the vision system to the CIEXYZ color matching functions for a certain illuminant. The CIELAB values are hereafter obtained by the standard transformation (Mendoza et al., 2006), and we obtain an L^*, a^*, and b^* image for all samples. For all three color components we follow the same strategy as for the nCDA meat color scale and extract the color of meat at certain radii of the salami.

Furthermore, we will assess the ΔE^*_{ab} value for the chilled and non-chilled samples. This parameter expresses the total sample difference, and is given by the Euclidean distance between the color coordinates (in the CIELAB color space) of a chilled and a non-chilled sample. ΔE^*_{ab} will be used in two evaluations. First in the assessment of the difference for chilled and non-chilled samples at the radii considered in the above analyses. Secondly, we will find the average color of the inner third of the salami, commonly used for sensory panel scoring, and determine if there is a visible difference between the chilled and non-chilled samples.

2.2.5 Texture

Figure 1 shows the fermentation progress for one recipe of salami, where a change in image texture over time can be seen as an increase in blended meat and fat pixels. In this section references to texture will relate to the image texture which is given in terms of changes in pixel values. This section will describe a possible way to capture the change in texture by considering gradient magnitude histograms (Lowe, 2004).

The gradient of an image, f, is defined as

$$\nabla f = \frac{\partial f}{\partial x} e_x + \frac{\partial f}{\partial y} e_y, \tag{4}$$

and can be found by simple filtering operations. A filter with the values $[-1, 0, 1]$ will in our case be applied to both directions of the image, such that the gradient of an image, $\boldsymbol{I}$, in a point (x, y) is given by

$$f'_x(x, y) = I(x + 1, y) - I(x - 1, y) \tag{5}$$
$$f'_y(x, y) = I(x, y + 1) - I(x, y - 1). \tag{6}$$

This filter represent a central difference definition of the gradient (Elden, Wittmeyer-Koch, and Bruun Nielsen, 2004). All the gradients in an image have an orientation, θ, and a magnitude, m, given by

$$\theta(x, y) = \arctan\left(\frac{f'_y(x, y))}{f'_x(x, y)}\right) \tag{7}$$
$$m(x, y) = \sqrt{f'^2_x(x, y) + f'^2_y(x, y)}. \tag{8}$$

In this study we will consider the distribution of the gradient magnitudes of the salami images. The gradient magnitude histograms will be found at different scales, such that texture changes at different scales will be captured. The scales considered will be found at five levels of a Gaussian pyramid. In each level of the pyramid the image is convolved with a Gaussian kernel and the resolution is halved. The number of bins in the histogram will be fixed for each scale. Moreover, the limits of the histogram will be the same for all samples., which makes the histograms comparable across samples. Figure 6 shows an example of gradient magnitude images at the five levels of the Gaussian pyramid. In this analysis we apply the background-salami mask found previously, such that the texture measure we find is only defined for the salami itself.

Several parameters influence the histograms. The number of scales is chosen to be five in this case. We also wish to find the most suitable amount of bins in the histogram per scale and what spectral band is the most descriptive. We have chosen to investigate the

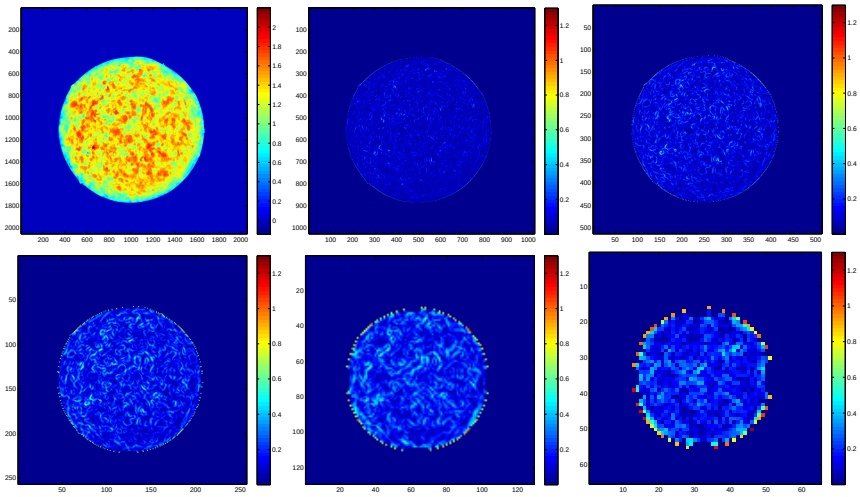

Figure 6: Single band image (890 nm) and the corresponding gradient magnitude images at the five levels of the Gaussian pyramid.

number of bins to be 16, 32, 64, 128, and 256. For each wavelength and number of bins the histogram is found by concatenating the histograms for the five considered scales. An example of a concatenated histogram of a day 2 sample is seen in Figure 7.

The dissimilarity between two histograms, h_1 and h_2, are found in terms of the Chi-square distance metric

$$d(h_1, h_2) = \frac{1}{2} \sum_{i=1}^{n_{\text{bins}}} \frac{(h_1(i) - h_2(i))^2}{h_1(i) + h_2(i)}. \tag{9}$$

The mutual Chi-square distance for all types of recipe at the observation days are illustrated by a distance matrix in Figure 8. The distance matrix shown is for the 17th spectral band (890 nm), and is sorted after recipe type (R1, R2, R3, R4). The blocks along the diagonal are therefore for one recipe. Within recipe the samples are sorted with respect to days, such that the sequence is 2 days non-chilled, 2 days chilled, 3 days non-chilled, 3 days chilled, and so forth.

A visual inspection of the distance matrices for all spectral band and bin size combinations showed that varying the bin size resulted in similar distance behavior, but the range of the distance measure grew as the number of bins increased. It was hence chosen to use 64 bins at each of the five scales, since it limits the amount of variables in the further analysis but it still captures the variation within each scale in a satisfactory manner.

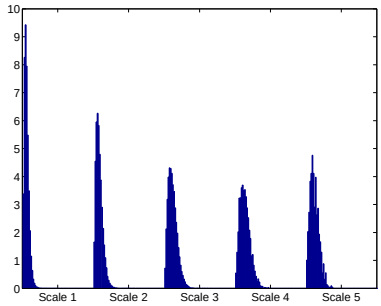

Figure 7: Histogram example of the five levels in the Gaussian pyramid for a day 2 sample. The histogram distribution is wider at the the coarser scales of the Gaussian pyramid.

The gradient magnitudes are dependent on the spectral band, and we wish to investigate if any of the bands are better at describing the data than the rest. For each band the histogram data is given by $\boldsymbol{Y}_i = (\boldsymbol{y}_{i,1}, \boldsymbol{y}_{i,2}, \ldots, \boldsymbol{y}_{i,320})^T$, $i = 1, \ldots, 132$, and from this the principal components are found. The first two principal components are are subject to an analysis of variance (ANOVA) with the main effects of day, chilled/non-chilled factor, recipe type, and their two way interactions to identify important effects. The spectral band describing the data best is determined by how well the model fits the data variation in the principal components, expressed by the coefficient of determination, the R^2 value. This way it was confirmed that the spectral band of 890 nm fitted the variation in the categorical variables slightly better than some of the other bands. This spectral band lies in the NIR wavelength, and as seen in Figure 9, the difference between meat and fat in absolute pixel value is higher for the NIR bands than e.g. the second spectral band (405 nm). The principal components of the histograms will be considered in the further analysis of the texture measure.

2.3 Statistical Analysis

The above feature extraction methods gives a catalogue of variables to use in the further analysis. The features extracted will be subject to a statistical analysis that reflects the purpose of the study; the comparison of chilled and non-chilled samples. In general an extensive model formulated as

$$y_{ij}(t) = \mu + c_i + r_j + cr_{ij} + \beta_{ij}t + \gamma_{ij}t^2 + \varepsilon_{ijt} \qquad (10)$$
$$i \in \{0, 1\}, j \in \{1, 2, 3, 4\},$$

will be applied throughout the study as an initial statistical analysis of each of the features extracted. Here t is time point, and c and r are the main effects of chilling and recipe.

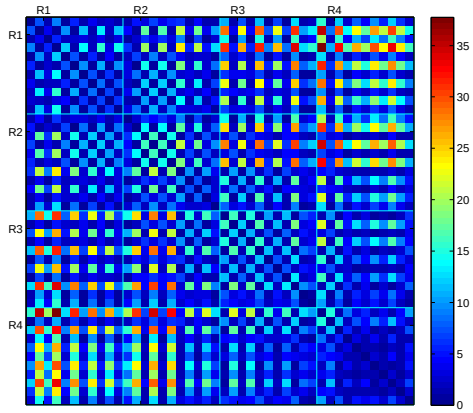

Figure 8: χ^2 distances for spectral band 17 with 64 bins for each histogram at five scales. Here divided by type/recipe, such that the square R1 holds all recipe 1 samples, both fresh and chilled ones, sorted by fermentation days. Same goes for the remaining three recipes.

Interactions and polynomial effects of the main effects are also considered. In order to identify the significant effects of the different parameters described above, we turn to a stepwise approach for estimating a general linear model. Beal (2007) has compared different model selection criteria and found that Schwarz‘ Bayesian Information Criterion (SBC) given in terms of the Sum of Squares Error (SSE)

$$\mathrm{SBC} = n \ln\left(\frac{\mathrm{SSE}}{n}\right) + k \ln(n) \tag{11}$$

gave superior results in a series of simulation studies. The models found will be subject to an Analysis of Variance (ANOVA) to identify important variance contributors. Besides the linear model described in (10), we will also apply non-linear models whenever the physics behind demands it or the data suggests it. The statistical analyses will be performed in SAS by use of general linear models and stepwise selection methods.

For the analysis of the width of the salami we will use a model based on physical assumptions about the evaporation from the salami. If we assume that the evaporation at any time, t, is proportional to the amount of water $y(t)$ in the salami, $y(t)$ will satisfy a differential equation $\frac{dy}{dt} = -ky(t)$ which has the solution

$$y(t) = ce^{(-kt)}. \tag{12}$$

The shape is cylindrical and thus the diameter is (basically) proportional to the square root of the volume and will therefore also decrease exponentially. The dry matter will not

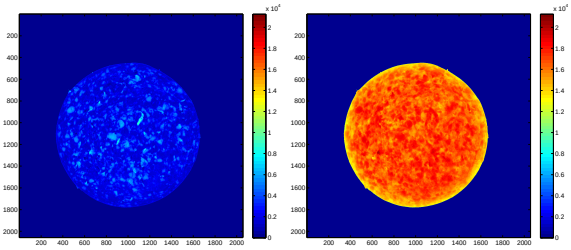

Figure 9: Salami at day 2 of fermentation. Left: Spectral band 2 (405 nm). Right: Spectral band 17 (890 nm).

disappear over time, and therefore it could be expected that the diameter will decrease asymptotically to a limit larger than zero. If chilling and subsequent thawing releases water from cells and make it more available for evaporation, one might see an increased evaporation in the beginning, and we might be in a situation as described in Figure 10, with a difference in models for the chilled and non-chilled samples.

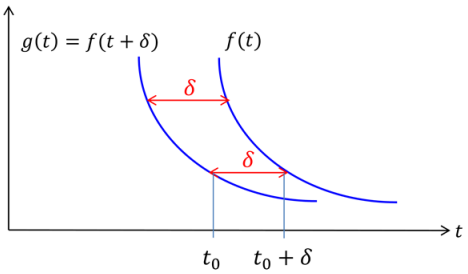

Figure 10: Illustration of the decay in salami width as a function of time.

3 Results

3.1 Width features

The average widths of the salamis are are show in Figure 11a. As expected we see a clear tendency that the width of the sample decreases as the fermentation progress. After day 21, it seems like the shrinkage stalls, which would fit the model described in (12).

Investigating the width data with the model in (10), it turned out that none of the effects

involving recipe, r were selected, and the polynomial term were neither dependent on the chilling process. The resulting model is of the form

$$w_1(t) = \begin{cases} \alpha_0 + \beta_0 t + \gamma t^2, & \text{for } c = 0 \\ \alpha_1 + \beta_1 t + \gamma t^2, & \text{for } c = 1 \end{cases}, \tag{13}$$

i.e two parabolas with different intercepts and coefficients to the first order time component, t. We may consider a re-parametrization that brings two parabolas on the form considered above, i.e.

$$w_2(t) = \begin{cases} \alpha + \beta t + \gamma t^2, & \text{for } c = 0 \\ \alpha + \beta(t-\delta) + \gamma(t-\delta)^2, & \text{for } c = 1 \end{cases} \tag{14}$$

Both models, w_1 and w_2, have a possible minimum in the time period considered (2-42 days), which makes them unfeasible. Instead we introduce the model

$$w_3(t) = \begin{cases} \lambda + \exp(-\frac{t-\alpha}{\beta}) & \text{for } c = 0 \\ \lambda + \exp(-\frac{t-\alpha-\delta}{\beta}), & \text{for } c = 1 \end{cases} \tag{15}$$

that corresponds well with the behavior of the data and has an asymptote that will represent the width that the salami stalls at. This model incorporates the exponentially decaying functions introduced in (12) only deviating from each other by a time shift as above, with an added, common asymptote.

By fitting the data to the three models in (13)-(15) results seen in Figure 11 are obtained. In the models w_2 and w_3 the δ parameter describes the difference in fermentation stages for the chilled and non-chilled samples. In model w_2 the fit gives $\delta = -0.505$, which means the chilling process speeds up the fermentation by approximately half a day. In w_3 we find $\delta = -0.9771$, so this model describes that the chilling process speeds up the fermentation process by almost a day.

3.2 Analysis of statistical color scale

The nCDA meat color scale is illustrated in Figure 12, where the results are shown for each of the considered fermentation stages with respect to the radius from the center of the sample. The average over the three images within one recipe is shown, and the samples are also split for non-chilled and chilled samples. The plots show a clear development in the color towards the rim of the salami, and a general increase in nCDA value as the samples gets older. Moreover, it looks like there is some separation between the meat color for the non-chilled and chilled samples. It becomes more dominant at the center of the salami for the later fermentation stages.

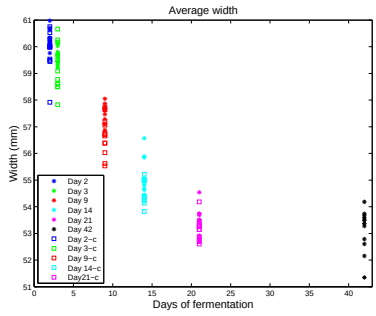

(a) Salami width at different fermentation stages (days).

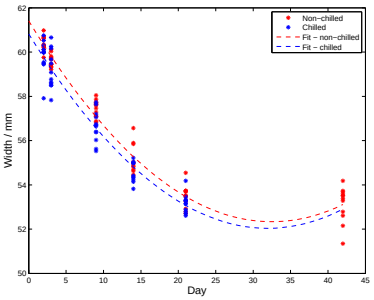

(b) Fit of the polynomial model in (13).

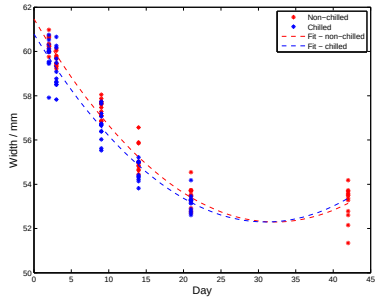

(c) Fit of the polynomial model in (14).

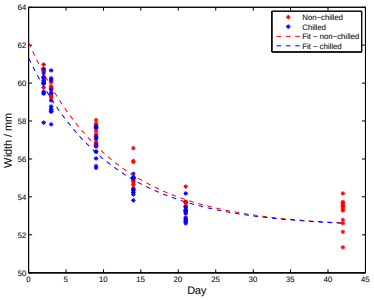

(d) Fit of the exponential model in (15).

Figure 11: Nonlinear fit of salami width.

To explore the co-variability of the salami samples we employ a PCA. The analysis shows that the first and second principal components (PC) explains 99.5% of the variance in the data. In Figure 13 the first two PCs are plotted against each other. The color indicates days of fermentation, whereas the symbols (cross or circle) indicate whether the samples have been chilled. The PC loadings in Figure 13a show that the first PC describes an average color across all radii. For the second PC the observations close to the center and again at the rim have great influence. It describes the contrast between the inner and outer part of the salami slices. The scatter plot in Figure 13b indicates that the variation relating to PC1 is mostly due to the different fermentation days and that the relative small variance ($\sim 3.6\%$) explained by the second PC is due to the chilling effect. The plots show that there is a good separation between days of fermentation, except for days 2 and 3, where the color of the salamis has not changed much. In general it seems like the chilled samples have a slightly lower value than the non-chilled salamis, when PC2 is considered.

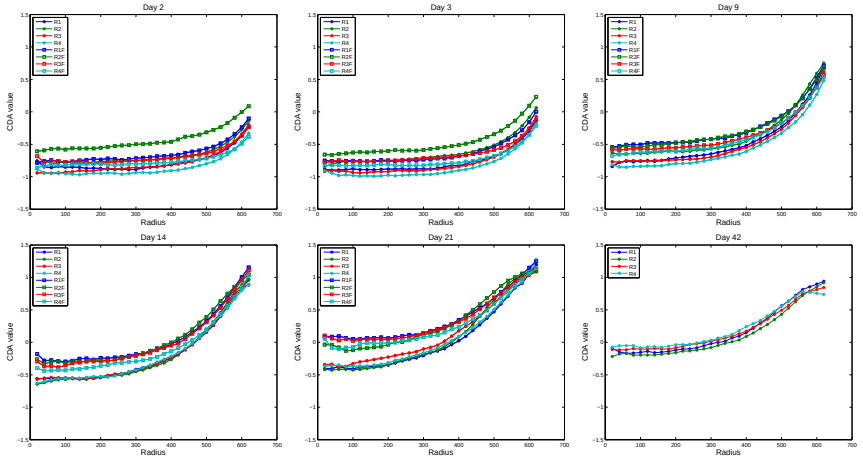

Figure 12: Color distribution through the salamis expressed on the meat color scale found by canonical discriminant analysis. Here the colors measured for each day are shown.

The observations from Figure 13 are analyzed based on the first two principal components. For each of the two components we will use the SBC criterion for choosing the most appropriate model parameters based on the model in (10). For both principal components all effects are significant, except the interaction of chilling process and recipe, cr. The continuous effects of days, t and t^2, are though dominant with a relative high mean sum of squares. These results indicate that the chilling process do influence the color of the salamis, but that the influence is even for all four different recipes. It is not possible to uniquely estimate the parameters of the model including all significant effects due to singularity of the data matrix, and we therefore consider a simpler model to describe the development in the first principal component:

$$p_1(t) = \begin{cases} \alpha_0 + \beta_0 t + \gamma t^2 & \text{for } c = 0 \\ \alpha_1 + \beta_1 t + \gamma t^2 & \text{for } c = 1 \end{cases} \tag{16}$$

Figure 14 shows the fit of this model to the principal components. This model is similar to the expression in (13) and we can therefore re-parametrize the model, such that the model is expressed as in (14). Fitting the data to such a model returns the fit seen in Figure 14c. The time shift (δ) is in this case estimated to be 3.2 days. Since the first PC is a measure of average color across the sample, this means that the average color of the chilled samples are 3 days ahead of the non-chilled samples in the color development. For the second PC a

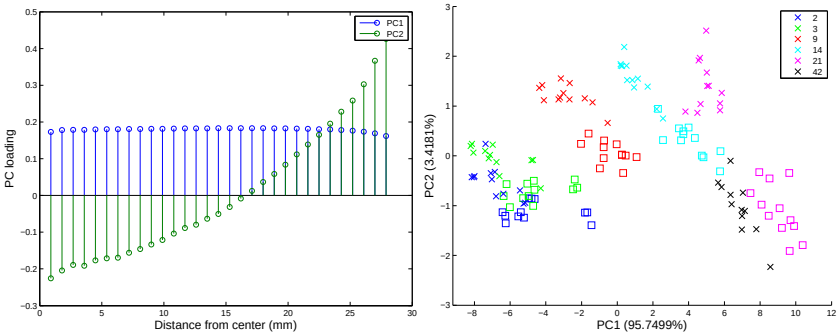

(a) Principal components loading for the first three principal components.

(b) The first and second principal component of the meat color scale data.

Figure 13: The PC loadings of the meat color scale, where the first is an average color across the sample, and the second is the contrast between the center and rim of the salami. (b) shows PC1 against PC2 with circles representing non-chilled samples and crosses are the chilled samples - both color coded by observation day.

similar model was found, but with chilling dependency of the polynomial time coefficient:

$$p_2(t) = \begin{cases} \alpha_0 + \beta t + \gamma_0 t^2 & \text{for} \quad c = 0 \\ \alpha_1 + \beta t + \gamma_1 t^2 & \text{for} \quad c = 1. \end{cases} \tag{17}$$

The fit of this model is seen in Figure 14b. This result clearly shows that it is possible to differentiate between the chilled and non-chilled samples for the second PC, which supports the results in Figure 13b. The difference in color seems to increase with the number of fermentation days.

These results indicate that there is in fact a color difference for the non-chilled and chilled samples. The difference observed for the first principal component indicate that the average color of the chilled samples is different from the average color of the non-chilled samples. The time difference of the two groups is approximately 3 days. For the second principal component, describing the contrast between the center and the rim of the salami also indicates a difference for chilled and non-chilled samples.

3.3 CIELAB color analysis

The second approach for assessing color difference in the chilled and non-chilled samples is to look at the color components L^*, a^*, and b^* of the CIELAB color space. The change in

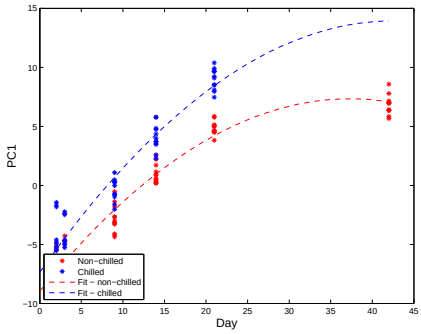

(a) First PC of CDA meat color scale.

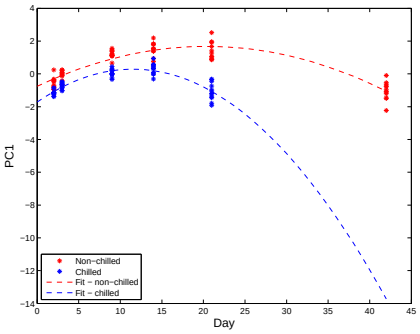

(b) Second PC of CDA meat color scale.

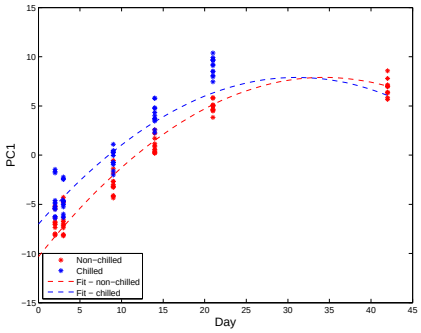

(c) First PC of CDA meat color scale with time shift. Time shift is three days.

Figure 14: First and second PCs of the CDA meat color scale with the fits described in (16) and (17).

color is primarily due to changes in the a^* component since this reflects the change in red color, but as the meat gets darker red, the L^* component will most likely decrease.

The analysis for each color component is similar to the analysis of the nCDA scale; a PCA is performed and the two first principal components are investigated with respect to the model in (10). The PC loadings of the three color components are shown in Figure 15, and it is observed that for the L^* and a^* data the first PC describes an average across the salami, whereas the second PC is again the contrast between the color at the rim and the center. For the b^* value the behavior is slightly different. The first PC is in this case an average for the inner part of the salami, and the second PC is dominated by the observations close to the rim.

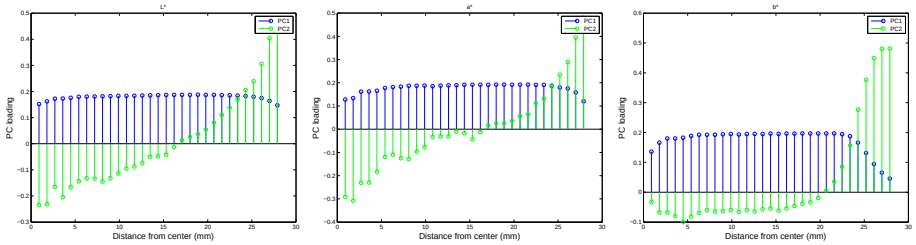

(a) PCA loadings for the L^* values for the first and second PC.

(b) PCA loadings for the a^* values for the first and second PC.

(c) PCA loadings for the b^* values for the first and second PC.

Figure 15: First and second PCs of the L^*, a^*, and b^* color components as extracted at different radius from the center of the salami.

The explorative analysis of each color component showed that the day 2 samples of recipe 2 had great influence on the model fits. The Rstudent residuals and also Cook's D was greatly above the average for all analyses performed. It was therefore chosen to fit a separate model for recipe 2 for all observation days. This also means that the PCA and the analysis of the principal components will be given in terms of two datasets; one with recipe 1, 3, and 4 included, and the other with only recipe 2 included.

At first the L^* values are investigated. The stepwise selection method results in a model with main effects recipe, r, and chilling c for the first PC. For the dataset including recipe 1, 3, and 4, reliable model parameter estimates are obtained by considering the following models:

$$p_{1,L^*}(t) = \begin{cases} \alpha_j + \beta t + \gamma_0 t^2, & c = 0, \quad j = 1,2,3,4 \\ \alpha_j + \beta t + \gamma_1 t^2, & c = 1, \quad j = 1,2,3,4 \end{cases} \tag{18}$$

$$p_{2,L^*}(t) = \begin{cases} \alpha_0 + \beta_0 t + \gamma t^2, & c = 0 \\ \alpha_1 + \beta_1 t + \gamma t^2, & c = 1. \end{cases} \tag{19}$$

The models for the dataset including only recipe 2 were found as

$$p_{1,L^*}(t) = \begin{cases} \alpha_0 + \beta_0 t, & c = 0 \\ \alpha_1 + \beta_1 t, & c = 1 \end{cases} \tag{20}$$

$$p_{2,L^*}(t) = \begin{cases} \alpha_0 + \beta_0 t + \gamma t^2, & c = 0 \\ \alpha_1 + \beta_1 t + \gamma t^2, & c = 1 \end{cases}. \tag{21}$$

In Figure 16 the fits are seen. The models indicate that the L^* component develops differently in the four different recipes. Moreover there is a constant difference for the

chilled and non-chilled samples. It should be noted that for the model in (18), $\gamma 1$ is not statistically different 0. This problem arise due to the absence of chilled samples from day 42.

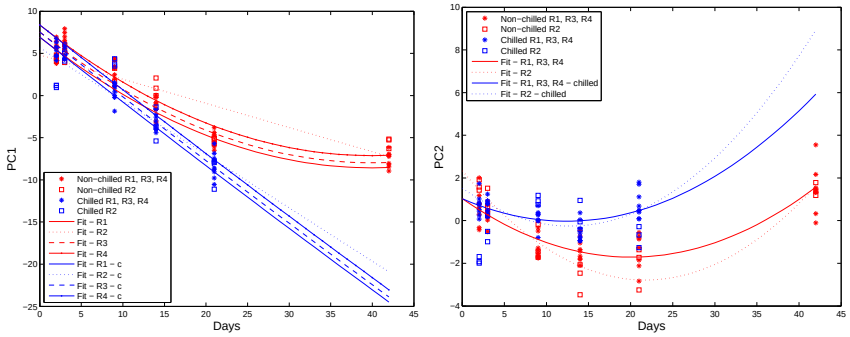

Figure 16: Left: PC1 of L^* values. Right: PC2 of L^* values.

The a^* values are analyzed just as the L^* values, and the fitted models for the dataset including recipes 1, 3, and 4, for the first two PCs are given as

$$p_{1,a^*}(t) = \begin{cases} \alpha_0 + \beta t + \gamma t^2, & c = 0 \\ \alpha_1 + \beta t + \gamma t^2, & c = 1 \end{cases} \tag{22}$$

$$p_{2,a^*}(t) = \begin{cases} \alpha_0 + \beta t + \gamma t^2, & c = 0 \\ \alpha_1 + \beta t + \gamma t^2, & c = 1 \end{cases} \tag{23}$$

The models involving only recipe 2 is given as

$$p_{1,a^*}(t) = \begin{cases} \alpha_0 + \beta_0 t, & c = 0 \\ \alpha_1 + \beta_1 t, & c = 1 \end{cases} \tag{24}$$

$$p_{2,a^*}(t) = t. \tag{25}$$

In Figure 17 the fits of model are seen. The first two PCs of the dataset with recipes 1, 3, and 4 are described by similar models, but with different coefficients. Here we clearly see a dependence on the chilling process. The recipe data are dependent on the chilling process only for the first PC, and it is a linear dependency. The second PC is only described by the time dependency, which is in fact not a significant model.

Finally, the stepwise regression for the PCs of the b^* component also returns different

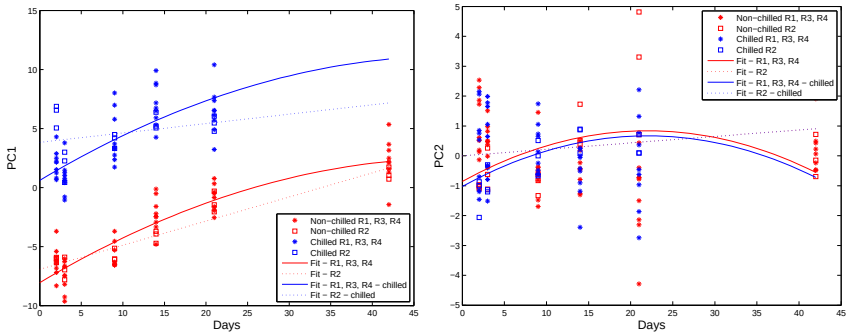

Figure 17: Left: PC1 of a^* values. Right: PC2 of a^* values.

models for the two PCs. First for the dataset with recipes 1, 3, and 4:

$$p_{1,b^*}(t) = \begin{cases} \alpha_0 + \gamma t, & c = 0, \\ \alpha_1 + \gamma_j t, & c = 1, \end{cases} \tag{26}$$

$$p_{2,b^*}(t) = \alpha_j + \gamma t^2, \quad j = 1, 3, 4. \tag{27}$$

For recipe 2 the model is

$$p_{1,b^*}(t) = \begin{cases} \alpha_0 + \beta t + \gamma_0 t^2, & c = 0 \\ \alpha_1 + \beta t + \gamma_1 t^2, & c = 1 \end{cases} \tag{28}$$

$$p_{2,b^*}(t) = \begin{cases} \beta_0 t + \gamma_j t^2, & c = 0,\ j = 1, 3, 4 \\ \beta_1 + \gamma_j t^2, & c = 1,\ j = 1, 3, 4. \end{cases} \tag{29}$$

These results indicate that the variation of the b^* component is dependent on the chilling and recipe, but just as for the L^* component, the chilling process influences the different recipes differently. The data and corresponding fit of the models obtained are seen in Figure 18.

The analysis of the individual color components showed that all three color components are influenced by the chilling of the samples. Especially the a^* component is influenced by the chilling, which relates well with the fact that it is the a^* component that represent red colors. But the statistical significant influence of the chilling may not represent a visual detectable difference. We find the ΔE^*_{ab} values by averaging the original radius dependent color measurements for the three replicates within each recipe type. Hereby we obtain an average difference for each recipe type on all observation days. The differences are summarized in Figure 19 and we see that the total difference in color is below 5 units

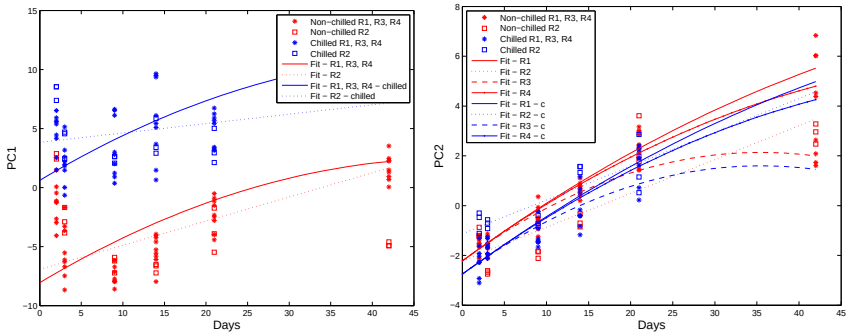

Figure 18: Left: PC1 of b^* values. Right: PC2 of b^* values.

for all radii. The threshold for human detection of color difference is around 3 - 6 units (Larraín, Schaefer, and Reed, 2008). These results show that there is a difference in color for the chilled and non-chilled samples, but also that the difference is on the edge of being negligible for the human vision.

The inner third of the salamis are often used for color judgement by a sensory panel. Considering the average L^*, a^*, and b^* values for these areas gives an average ΔE^*_{ab} value of approximately 2.1 and the maximum value is 2.9. This gives reason to believe that the chilling process does influence the color of the salamis, but that it will be a change in color that is hard to detect for a sensory panel.

Texture The gradient magnitude histograms are extracted for all spectral bands at each wavelength. As described in Section 2.2.5 it was chosen to use the 17th spectral band (890 nm) for this analysis. In Figure 8 the overall histogram distances are displayed. The checker-like behavior in the block-diagonal of each recipe indicates that there is some difference in the texture of the non-chilled and chilled samples.

The observations of Figure 8 will again be investigated by taking a close look at the principal components of the histogram data. The first three principal components explain 80.7% of the variance in the histogram data, with the first PC explaining $\sim 64\%$ by itself. As can be seen from Figure 20 the first PC is dominated by the lower gradient magnitude values, and they do not put much weight on the parts of the histogram that are close to zero. The second and third PCs put greater importance on the histograms at the lower levels of the image pyramid.

Scatter plots of the first three PCs are shown in Figure 21. From these plots it seems like PC1 describes the development over time, but with a shift for the two groups (chilled and

non-chilled). It is difficult to say anything specific about the second and third PC.

By a statistical analysis of each of the first three PCs we can to some extend establish whether this feature is descriptive of a potential texture difference between the non-chilled and chilled samples. Again we find a general linear model by a stepwise selection method from the model in (10), and obtain an ANOVA for each principal component. The identified significant effects give rise to the following models describing each PC:

$$Y_1(t) = \begin{cases} \alpha_0 \ + \beta_0 t + \gamma t^2, & c = 0 \\ \alpha_1 + \beta_1 t + \gamma t^2, & c = 1 \end{cases} \tag{30}$$

$$Y_2(t) = \begin{cases} \alpha_0 \ + \beta_0 t, & c = 0 \\ \alpha_1 + \beta_1 t, & c = 1 \end{cases} \tag{31}$$

$$Y_3(t) = \begin{cases} \alpha_0 + \beta t + \gamma t^2, & c = 0 \\ \alpha_1 + \beta t + \gamma t^2, & c = 1. \end{cases} \tag{32}$$

The fits are seen in Figure 22. The models reflect that the first PC describes the difference in chilled and non-chilled samples. It is possible to put the model in (**??**) on the form in (14). The parameter estimation showed that the time difference of the chilled and non-chilled samples were 13 days, which seems unreasonable. The results clearly indicate that there is a statistical difference in the texture features of the chilled and non-chilled samples. Just as for the artificial meat color scale it is though hard to quantify the structural change.

The features extracted from the multispectral images showed that the chilled and non-chilled samples do differentiate from each other. The individual analyses of the features showed statistical differences. In the case of the width of the salami it was possible to quantify the difference in days of fermentation, whereas the color difference was translated to the CIELAB space and quantified by the ΔE^*_{ab} value to identify if there was a visual difference. A texture difference was also observed, but hard to relate to the any sensory or physical parameter.

4 Conclusion

The study showed that the multispectral images and the image image analysis tools are applicable in the study of fermented sausages. In this study the features revealed a statistical difference for the chilled and non-chilled samples. At the same time it was possible to relate the image information to physical parameters that would possible be detectable by a sensory panel. The study shows the efficiency of a vision system in detection of even

small differences, in this case for chilled and non-chilled samples. It offers a reliable and objective measure of the product properties.

5 Aknowledgement

This work has been financed by the Center for Imaging Food Quality, a project funded by the Danish Council for Strategic Research (contract no 09-067039) within the Program Commission on Health, Food and Welfare. The experiments were conducted in collaboration with laboratory technicians at DuPont Nutrition Biosciences ApS.

References

Dennis J. Beal. Information criteria methods in sas for multiple linear regression models. *SESUG Proceedings. Paper SA05. Raleigh, NC: North Carolina State University*, 2007.

Marta Chmiel, Mirosław Słowiński, and Krzysztof Dasiewicz. Lightness of the color measured by computer image analysis as a factor for assessing the quality of pork meat. *Meat science*, 88(3):566–570, 2011.

Bjørn Skovlund Dissing, Olga S. Papadopoulou, Chrysoula Tassou, Bjarne Kjær Ersbøll, Jens Michael Carstensen, Efstathios Z. Panagou, and George-John Nychas. Using multispectral imaging for spoilage detection of pork meat. *Food and Bioprocess Technology*, 6(9):2268–2279, 2013.

L. Elden, L. Wittmeyer-Koch, and H. Bruun Nielsen. *Introduction to numerical computation - analysis and MATLAB illustrations*. Studentlitteratur, 2004. ISBN 9789144037271.

R.E. Larraín, D.M. Schaefer, and J.D. Reed. Use of Digital Images to Estimate CIE Color Coordinates of Beef. *Food Research International*, 41(4):380–385, 2008.

Frédéric Leroy and Luc De Vuyst. Lactic acid bacteria as functional starter cultures for the food fermentation industry. *Trends in Food Science & Technology*, 15(2):67–78, 2004.

Frédéric Leroy, Jurgen Verluyten, and Luc De Vuyst. Functional meat starter cultures for improved sausage fermentation. *International journal of food microbiology*, 106(3): 270–285, 2006.

DavidG. Lowe. Distinctive image features from scale-invariant keypoints. *International Journal of Computer Vision*, 60(2):91–110, 2004. ISSN 0920-5691.

Fernando Mendoza and José M. Aguilera. Application of image analysis for classification of ripening bananas. *Journal of food science*, 69(9):E471–E477, 2004.

Fernando Mendoza, Petr Dejmek, and José M. Aguilera. Calibrated color measurements of agricultural foods using image analysis. *Postharvest Biology and Technology*, 41(3): 285–295, 2006.

Fernando Mendoza, Nektarios A. Valous, Paul Allen, Tony A. Kenny, Paddy Ward, and Da-Wen Sun. Analysis and classification of commercial ham slice images using directional fractal dimension features. *Meat science*, 81(2):313–320, 2009.

Flemming Møller, Rasmus Larsen, and Jens Michael Carstensen. *Imaging Food Quality*. IMM-PHD-2012. Technical University of Denmark, 2012.

Sara Sharifzadeh, Line Harder Clemmensen, Hanne Løje, and Bjarne Kjær Ersbøll. *Statistical Quality Assessment of Pre-fried Carrots Using Multispectral Imaging*, pages 620–629. Lecture Notes in Computer Science. Springer, 2013.

V. Steinmetz, J.M. Roger, E. Molt , and J. Blasco. On-line fusion of colour camera and spectrophotometer for sugar content prediction of apples. *Journal of Agricultural Engineering Research*, 73(2):207 – 216, 1999.

Da-Wen Sun and Tadhg Brosnan. Pizza quality evaluation using computer vision – part 2: Pizza topping analysis. *Journal of Food Engineering*, 57(1):91–95, 2003.

Camilla H. Trinderup, Anders Dahl, Kirsten Jensen, Jens Michael Carstensen, and Knut Conradsen. Comparison of a multispectral vision system and a colorimeter for the assessment of meat color. *Meat Science*, 102(0):1 – 7, 2015. ISSN 0309-1740.

Nektarios A. Valous, Fernando Mendoza, Da-Wen Sun, and Paul Allen. Colour calibration of a laboratory computer vision system for quality evaluation of pre-sliced hams. *Meat science*, 81(1):132–141, 2009.

E. van Kleef, HCM van Trijp, and P. Luning. Consumer research in the early stages of new product development: a critical review of methods and techniques. *FOOD QUALITY AND PREFERENCE*, 16(3):181–201, 2005.

Juan Xing and Josse De Baerdemaeker. Bruise detection on jonagold apples using hyperspectral imaging. *Postharvest Biology and Technology*, 37(2):152–162, 2005.

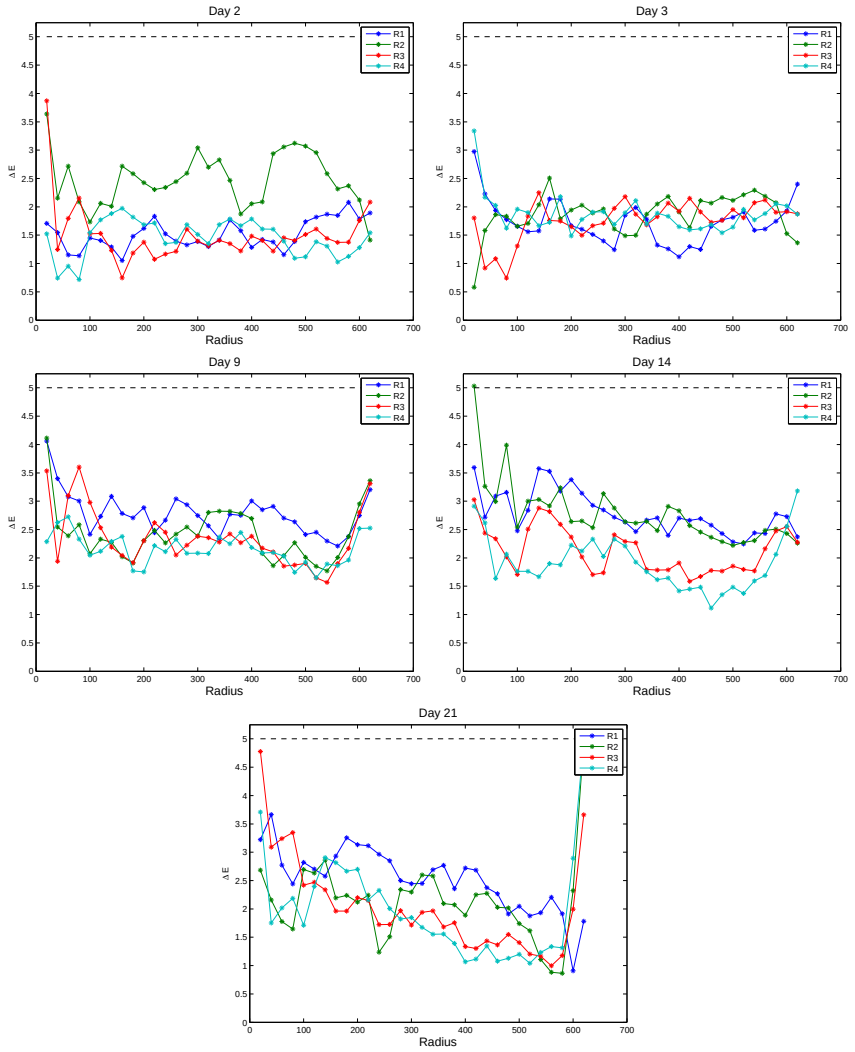

Figure 19: ΔE^*_{ab} values for each observation day. The graps express differences for chilled and non-chilled samples with the specified recipes.

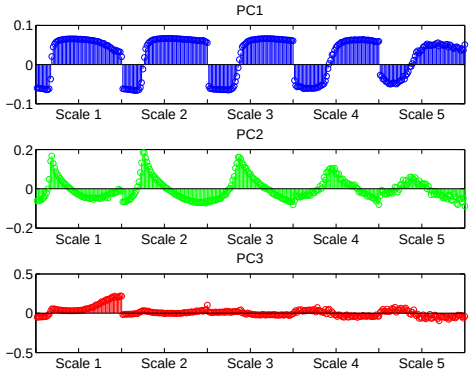

Figure 20: PC loadings for the first three principal components of the histogram data.

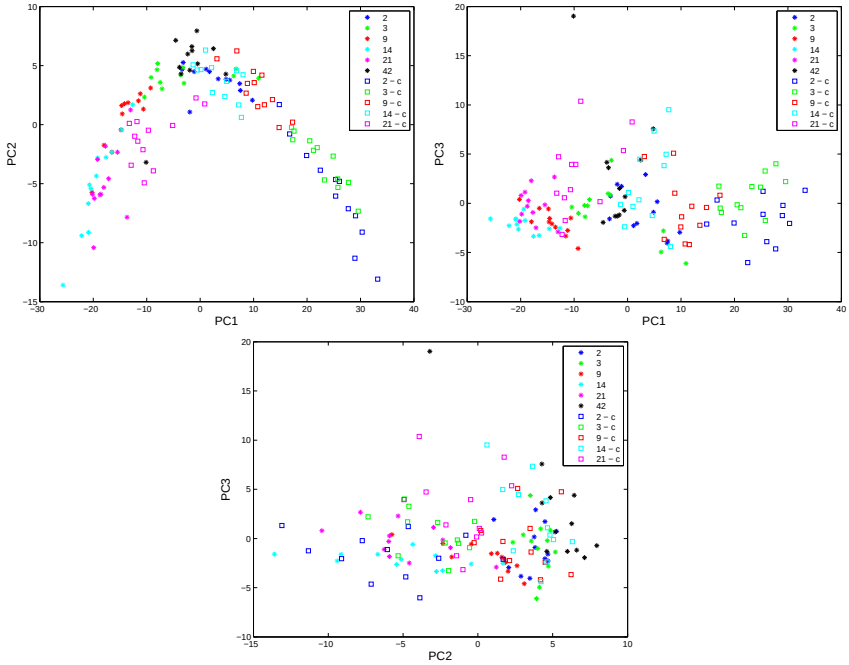

Figure 21: Scatter plots of PCs with days of fermentation as indicator split for non-chilled (x) and chilled (□)

.

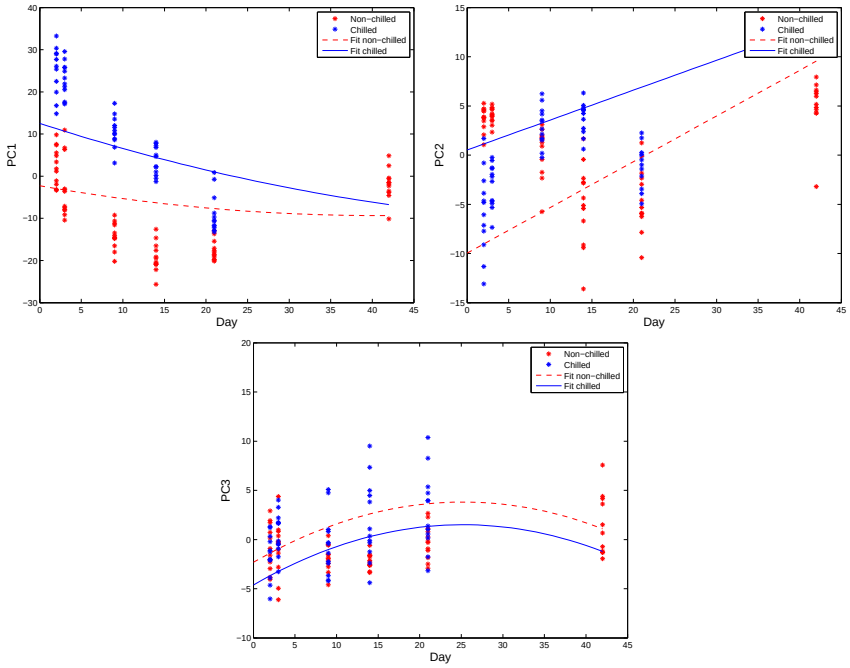

Figure 22: Fit of models for principal components for the texture features.

Appendix E

Identifying Boar Taint with a Hyperspectral Imaging System

Identifying Boar Taint with a Hyperspectral Imaging System

Camilla Himmelstrup Trinderup, Anders Bjorholm Dahl, Knut Conradsen

December 23, 2014

Abstract

In a couple of year's time it will be prohibited to castrate the male piglets in the European Union due to animal welfare. The downside of this is that the male piglets will when growing up, develop the hormone compounds skatole and androstenone. When the meat from these boars is cooked the hormones will give rise to an unpleasant odor, commonly known as boar taint. It will be advantageous to be capable of measuring the level of skatole and androstenone in a non-invasive and rapid manner. This can determine the appropriate use of the animal. This study aims at an optical method for predicting the level of the chemical compounds skatole and androstenone from boars. More specifically a hyper spectral imaging system employing static light scattering has been investigated. The results of the analysis that involved feature extraction from the images, showed that the system is not capable of prediction the level of the chemical compounds.

1 Introduction

In a couple of year's time it will no longer be legal to castrate piglets. When the male piglets grow without their reproductive organs intact, hormones will develop and influence their muscles. Two components giving rise to the unpleasant odor known as boar taint is androstenone and skatole. Androstenone is a hormone, also called a stesticular steroid, that develops as the male pig reaches sexual maturity. Skatole is a product originating from a microbial breakdown. Zammerini et al. (2012) describes how alterations of the boars' feed can lead to less bad smell. Several studies (Aluwé et al., 2009; Hansen et al., 2006) has had the same focus and showing the same tendency. But

the solution to the problem is not solved only by means of changing the diet of the pigs, and it will therefore be advantageous to have a method that can determine if the skatole level in a certain piece of lard is mostly suited for cold or warm consumed products.

A number of samples of lard from organic boars that have been fed in different ways are available. Chemical analysis of their fatty acid composition has been carried out to establish the level of skatole and androstenone. The aim of this study is to investigate the use of a hyper spectral subsurface light scattering (SLS) system to distinguish between the different fatty acid compositions. The SLS system delivers hyper spectral images at visible wavelengths. A preliminary study has shown that by using the image data from the SLS system with lard from different animals as subjects, it is possible to distinguish between the samples by deriving a slope parameter from the images of the scattering. This study will concern both classification of skatole and androstenone level from features extracted from the SLS images. The statistical analysis of the image features will involve unsupervised principal component analysis (PCA), analysis of variance (ANOVA), traditional classification methods and newer sparse versions appropriate for hyper spectral data.

It is important to note that the imaging system has only previously been used to discriminate between lards from different animals, which most likely have different structural properties, and therefore also different scattering properties. This study concerns samples of lard from pigs, and the difference in the samples arise from skatole and androstenone level. An extensive literature search have not revealed any former studies implying that the two chemical compounds actually influence the physical appearance of the samples. This means that the image features being extracted in this study are justified because of their previous performance in prediction tasks - mainly within yoghurt and milk products. Moreover, it is also relevant that the skatole and androstenone level are not correlated, so an increase in one does not necessarily mean an increase of the other.

2 Materials and Methods

This section will briefly describe the samples of investigation and the imaging system. The steps of the image analysis and the following statistical tools used for classification and regression analyses will be described more specific.

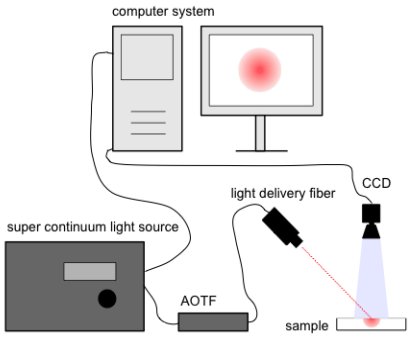

Figure 1: Illustration of the SLS system.

2.1 Imaging system

The imaging system employed in this study is denoted a static light scattering (SLS) system. The system set-up is illustrated in Figure 1. It shows how a laser with an acuusto optical tunable filter (AOTF) shines onto the sample. The reflection of the laser is captured by a camera mounted vertically above the incident point of the laser. The system details are described further by Skytte et al. (2012) The advantage gained by using hyper spectral imaging, is that the reflectance we see from the camera can be related to both the chemical compounds of the sample under investigation, but also the texture of the sample due to absorption and scattering respectively. In this study the spectral range is 440 nm to 990 nm with 10 nm intervals, which give 56 spectral bands. In Figure 2 an example of the data achieved is shown. For illustration, the image show the logarithm of the original data intensities.

2.2 Samples

47 lard samples from organic boars are under investigation. Each sample has a side with skin and one with lard. Three measurements are performed on the lard side of the sample. Lard is a structured material, so by acquiring three images of each with the laser at different incident points, we attempt to eliminate the factor of structure.

In order to achieve ground truth, a chemical analysis (HPLC) has been performed for each sample to establish the amounts of skatole and androstenone present in each sample. The amount of skatole in the samples ranges from

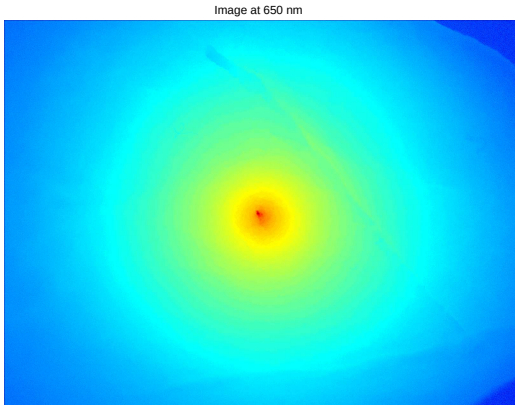

Figure 2: Example of image data. This is at 650 nm.

0.03 to 0.703 ppm, whereas androstenone accounts for 0.03 to 9.44 ppm. The amount of the two compounds does not necessarily follow each other. The scheme in Table 1 shows the results of the chemical analysis that was performed in order to reach the ground truth about the amount of skatole and androstenone in the samples ..

2.3 Principal component analysis

As a last method for analyzing the image data, we use a principal component analysis on the raw spectral data. The principal component analysis (PCA) is a tool to express what the sources contributing to variation are. Moreover the first principal component will reflect the average image across the spectral bands. Hence the first and second principal component (PC) will be subject to a Fourier analysis.

Since the resolution of the images are fairly high, the PCA is build from a 100×100 pixels patch around the incident point. This is justified, since the majority of the variation in the image is close to the incident point. In Figure 5 the original data is seen in the leftmost column. The second and third column are the logarithm of the first and second principal component (PC), whereas the two rightmost columns are images of the Fourier transform of the first and second PCs (logarithmic scale) respectively. From this schematic illustration we see that the first principal component reflects the diffuse scattering happening in the sample. The second PC only reflects variation close to the incident

Animal	Weight (kg)	Skatole (ppm)	Androstenone (ppm)
11	86.2	0.039	0.68
18	89.5	0.050	1.02
12	88.9	0.030	1.07
10	83.2	0.086	0.36
2	78.7	0.095	0.63
4	77.7	0.057	1.51
8	80.3	0.116	1.24
30		0.119	0.48
78	83.3	0.140	1.54
49	82.6	0.143	0.44
22	79	0.046	2.09
15	82	0.153	0.82
13	79.7	0.169	1.07
68	77.9	0.174	1.15
45	79.6	0.181	1.19
44	83.9	0.196	1.08
39	76.4	0.195	1.00
7	75.0	0.200	0.73
63	81.2	0.203	0.03
19	72.8	0.042	3.03
42	98.2	0.230	1.00
67	75.7	0.234	1.61
79	83.9	0.242	3.13
55	85.4	0.257	1.53
52	87.4	0.259	1.73
53	84.2	0.263	0.52
51	81.4	0.264	0.34
35	85.9	0.267	1.96
54	82.3	0.285	0.94
43	81.7	0.287	1.81
46	81.2	0.290	1.52
65	77.1	0.343	0.03
62	83.1	0.344	1.33
14	80.5	0.353	0.78
38	76.0	0.373	2.18
48	85.7	0.397	0.25
76	81.1	0.162	5.51
47	81.8	0.471	0.43
77	88.3	0.470	1.97
41	98.2	0.472	0.64
66	76.0	0.529	1.89
74	84.2	0.540	5.88
58	75.6	0.668	3.49
75	85.5	0.688	2.91
37	124.0	0.288	9.44
50	79.2	0.703	1.72

Table 1: Ground truth data from boars

point of the laser. From these data we will extract information about the eccentricity of the signal at specified distances from the incident point. This will be done from the FFT spectra of the first principal component. To locate any anisotropic behavior in the FFTs we extract average pixel information from circles/donuts at certain distances from the center, and also divided by polar angle. This feature extraction is illustrated in Figure 3. We will consider 25 equidistant radii from the center of the FFT, and angles at 30° intervals starting from 0. With the first feature being the center circle, this gives a total of 301 features for each sample. The replication of measurements on each sample is handled by averaging the features extracted for the three replicates.

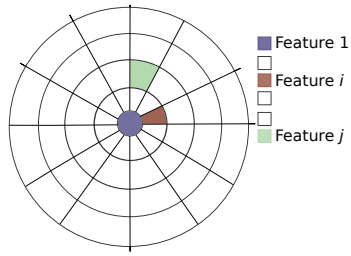

Figure 3: Feature extraction strategy for detection of anisotropy.

The last feature that will be extracted from the FFT image of the first PC, will be a feature describing at what distance from the center the maximum average is found. This is done by extracting the average pixel information in circles, just as was done in Figure 3. The position, or distance from the center of the image, of the maximum value will be extracted as a feature. In Figure 4 the procedure is illustrated.

The feature extraction of this section will therefore consist of features reflecting the nature of the FFT of the first principal component.

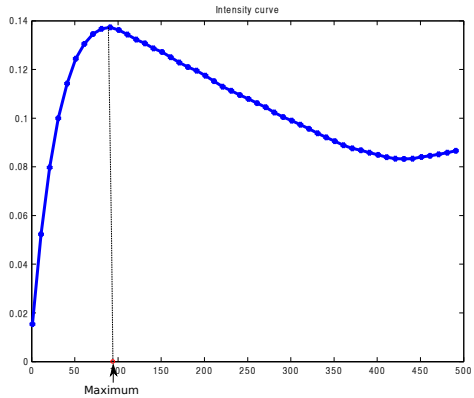

Figure 4: The position of the maximum values of the FFT image is found from curves like this one.

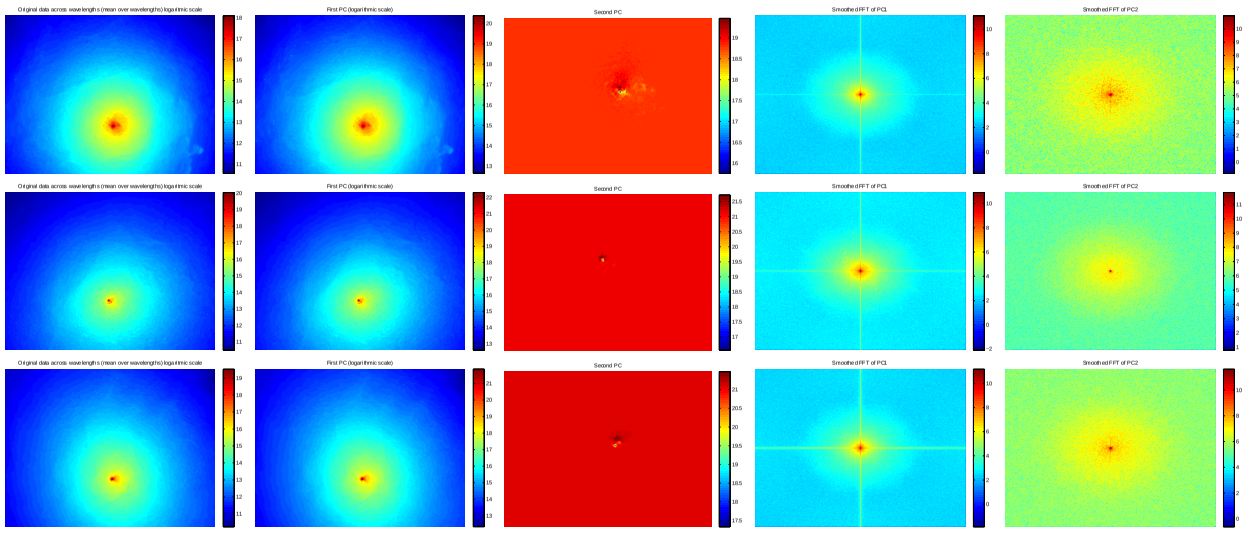

Figure 5: 1st column: Logarithm of average image across spectral bands. 2nd and 3rd column: Logarithm of first and second PC. 4th and 5th column: Fourier transform of the two PCs.

3 Results

3.1 Principal Component Analysis and Fourier Analysis

As described in Section 2.3 we extract several features from the Fourier spectra of the first PC. In Figure 6 examples of the anisotropy features are seen. A logarithmic scale has been applied for illustration purpose. The sort of stair-like behavior of the features originates from the feature sampling. Every 'step' represents all 12 angles at a specific radii from the center of the Fourier domain.

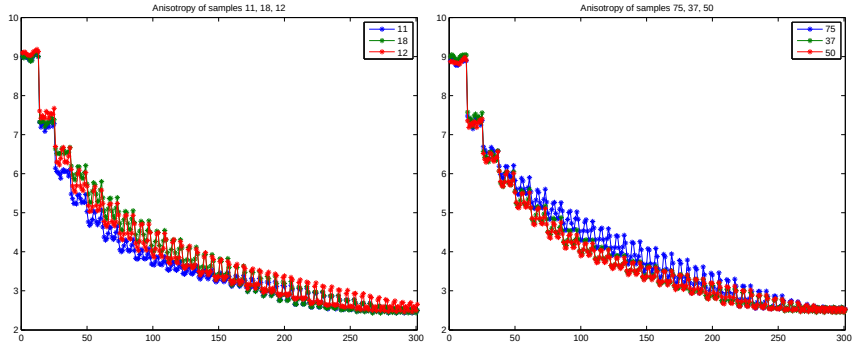

Figure 6: Anisotropy features at logarithmic scale for the three samples with lowest (left) and the three samples with the highest (right) skatole-androstenone level.

The plots of the anisotropy features in Figure 7 clearly shows how the features at the different polar angles are decreasing in value with the radius. From these plots it is not possible to say if the extracted features are capable of discriminating the boar samples.

The eccentricity features extracted are illustrated in Figure 8. The first impression of the eccentricity features are that they differ much more between samples than the anisotropy features above.

Finally the Fourier spectra was analyzed by extracting average pixel value in circles at defined radii from the center of the Fourier image. This only

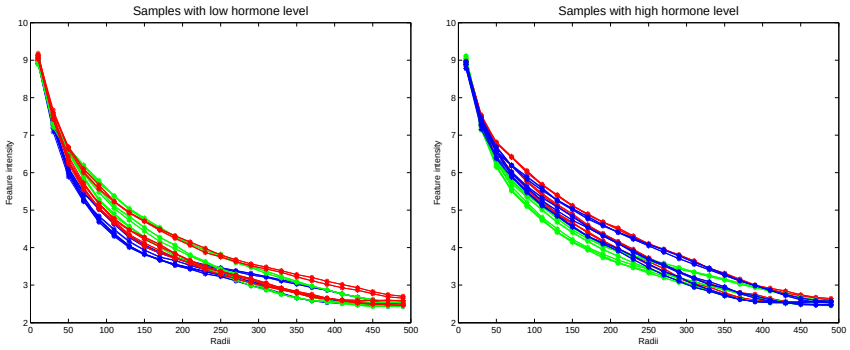

Figure 7: Anisotropy features at logarithmic scale for the three samples with lowest (left) and the three samples with highest (right) skatole-androstenone level. Here shown dependent on the radius, so several curves for each sample.

results in one feature per sample, which is illustrated in Figure 9. The x-axis represents the samples of increasing skatole and androstenone level, as seen in Table 1. No straightforward correlation seems to be found between the skatole and androstenone level and the distance at which the maximum value can be found at.

4 Statistical Analysis

Even though none of the features extracted from the image seem to have any clear relation to the level of skatole or androstenone, they have still been subject to statistical analysis. Regression method were considered for skatole and androstenone level individually with both ridge regression and lasso (Hastie, 2009), also split for the individual features. These investigations did not show any good results, except for some over fitting, that could easily be identified by cross validation.

To simplify the problem, a threshold value were set for both skatole and androstenone, and the problem then had discrimination nature instead of the continuous nature of the original skatole and androstenone levels. Both classical linear discriminant analysis (LDA) and sparse LDA (Clemmensen et al., 2011) was investigated for the discriminations. Unfortunately it was again not possible to show any good relations between the features extracted from the FFT of the first and second PC.

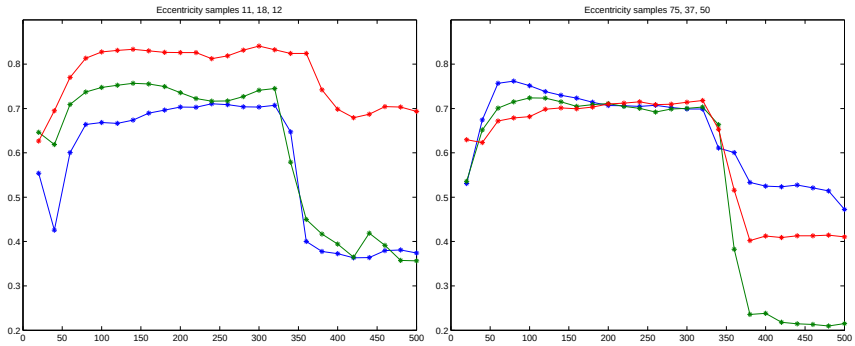

Figure 8: Eccentricity features for the three samples with lowest (left) and the three samples with highest (right) skatole-androstenone level.

5 Conclusion

The features extracted in this study from the SLS images of lard from boars showed that it was not possible to predict the levels of skatole, androstenone or a combined level of these. Advanced models were applied, but the amount of variables and the random nature of the levels of the chemical compounds leads to over fitting and models with no prediction power.

6 Aknowledgement

This work has been financed by the Center for Imaging Food Quality, a project funded by the Danish Council for Strategic Research (contract no 09-067039) within the Program Commission on Health, Food and Welfare. Thanks to Lene Meinert at the Danish Meat Research Institute for providing the samples for the experiment.

References

Aluwé, M., Millet, S., Nijs, G., Tuyttens, F., Verheyden, K., Brabander, H. D., Brabander, D. D., and Oeckel, M. V. (2009). Absence of an effect of dietary fibre or clinoptilolite on boar taint in entire male pigs fed practical diets. *Meat Science*, 82(3):346–352.

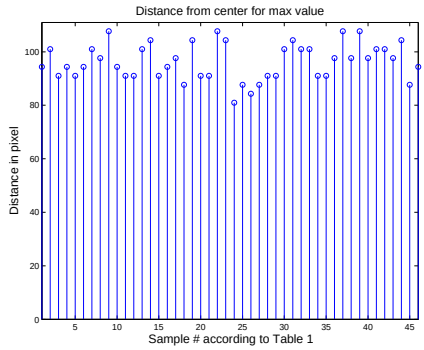

Figure 9: Distance from center of Fourier spectra to maximum value.

Clemmensen, L., Hastie, T., Witten, D., and Ersbøll, B. (2011). Sparse discriminant analysis. *Technometrics*, 53(4):406–413.

Hansen, L. L., Mejer, H., Thamsborg, S. M., Byrne, D. V., Roepstorff, A., Karlsson, A. H., and Hansen-Møller, J. (2006). Influence of chicory roots (chicorium intybus l) on boar taint in entire male and female pigs. *Animal Science*, 82:359 – 368.

Hastie, T. (2009). *The elements of statistical learning : data mining, inference, and predication*. Springer.

Skytte, J., Andersen, U., ller, F. M., Nielsen, O., Carstensen, J., Dahl, A., and Larsen, R. (2012). *Monitoring structure development in milk acidification using diffuse reflectance profiles*. University of Copenhagen.

Zammerini, D., Wood, J., Whittington, F., Nute, G., Hughes, S., Hazzledine, M., and Matthews, K. (2012). Effect of dietary chicory on boar taint. *Meat Science*, 91(4):396–401.

Appendix F

Food Quality Assessment from Multi-scale Structured Light.

Food Quality Assessment from Multi-scale Structured Light

Anders Bjorholm Dahl Camilla Himmelstrup Trinderup Rasmus Larsen
Knut Conradsen

December 22, 2014

Abstract

Computer vision systems including controlled illumination can be helpful in assessing food quality in an objective and repeatable manner. Advantages include the possibility of automating inspection, remote measurements with no contamination risk, measurement of large surface areas, etc. Light-food interaction is determined by the light spectrum and the chemical and structural properties of the food. One problem is that light reflected from a food item is not uniquely related to the properties of the food, such that samples with different properties may reflect the same light pattern. Additionally, there can be glossy surfaces resulting in specular highlights that corrupts the image data. To overcome these limitations we propose a computer vision system based on structured light, which can separate the reflected light into a direct and a global component. Additionally we propose a multi-scale acquisition technique that enables us to further separate the global component according to the subsurface path length in the sample. This enables a rich and precise characterization, which can easily be extended with a wavelength specific illumination. We demonstrate the concept of the system through an experimental validation.

1 Introduction

Visual inspection of food products through computer vision gives an objective assessment of the surface appearance of the product. Both surface reflectance and scattering properties are related to the chemical and structural properties of the food, and therefore visual inspection can act as a valuable instrument for food quality assessment [16]. Structured light has shown effective in separating light directly reflected from the surface of an object, termed the direct component, from the scattered light including subsurface scattering, termed the global component [12]. We have devised an instrument for food quality inspection based on this principle. The novelty of our instrumentation is both in regards to the application for food quality inspection and in an extended multi-scale acquisition technique. We provide a description for acquiring multi-scale images and experimentally investigate how food quality related features can be extracted.

The quality of the inspection is dependent on the image quality, and often glossy surface properties can corrupt the image, resulting in lower quality assessment. Specular highlights can be avoided by using a setup with diffuse sample illumination, e.g. by using an integrating sphere like the VideometerLab[1], by placing a diffuser in front of the light source, or using other illumination geometries. An extensive review for computer vision for food quality assessment is given in [18].

Structured light can be used as an alternative controlled illumination technique, where some properties similar to diffuse illumination is obtained, and in addition a rich characterization of surface reflectance and scattering properties is obtained. Our proposed method is inspired by the work of [12], where the so called direct and global components can be separated. Most specular elements are depicted in the direct component and most scattering and absorption information is retained in the global component, i.e. properties related to food color and structure. Especially colorfull global images are seen in objects with a large degree of subsurface scattering, which includes many food items like meat products.

The structured light method in [12] is based on a shifting checkerboard pattern, where only global components, including subsurface scattering and object intra-reflections, are seen in the unlit checkers. The lit checkers contains both the direct and global component, and through spatial shift the two can be separated. Typically many images are required because the spatial shifts must be small in order to obtain a satisfactory result. An alternative is to use e.g. a sinusoidal pattern, limiting the required number of projections to three or one projection using a high frequency stripe illumination.

Structured light have mainly been used in 3D surface reconstruction for object recognition, estimating properties of materials and visual inspection. The Microsoft Kinnect is a well-known product incorporating structured light for depth sensing, which is used for e.g. human motion detection with a range of applications primarily in the entertainment industry, but also in other vision applications. Earlier applications of structured light include e.g. biomedicine [3, 4]

Spatial frequency domain imaging is used for estimating optical parameters including absorption and scattering parameters using structured light [10]. In spatial frequency domain imaging sinusoidal projection patterns with varying wavelengths are typically used. Study examples include tissue phantoms [14], mouse brains [9] and breast tissue [8]. Multiwavelength systems has also been proposed [11] for projecting 34 band in the range 680 nm to 980 nm using DLP techniques [5].

Separating diffuse and specular components has been investigated by other methods earlier. A review of the specific methods are given in [2]. In general terms there are two different angles towards separation of the specular and diffuse components of an object, either single or multi image methods. The first category establishes the specular component by only a single image. The different methods within this category is either based on color information, neighborhood analysis, ODE approach, image inpainting, or a combination of

[1] `http://videometer.com/`

one or more of these.

The methods of the second category are as the name indicates based on two or more images of the object or scene of interest. In general the methods within these categories are either build on different light settings, such as flash methods, polarizing, or structured light. The principle behind the different methods is an assumption of an additive model for the total reflection with contributions from only a specular and diffuse component.

The advantage of using a single image method is that the acquisition of the image is fast, however precision is lost compared to multi-image methods. Indirect illumination can also be used for separating the global and direct light components [6, 7] using a technique similar to [12]. Hereby some problems relating to highlights might be avoided.

Structured light techniques has been used in food inspection mainly for 3D geometry analysis, e.g. for identifying apple stems and calyxes by taking advantage of the prior knowledge about their convexity [13, 19].

The contribution of our work is an instrumentation for food quality inspection using multi-scale structured light based on the simple principle for separating the global and direct light components.

2 Method

A simple method for separating the global and direct radiance components is described in [12], and our approach extends this work. We start by summarizing their findings and then describe our extension.

In order to separate the radiated light into a global and a direct component Nayar et al. [12] suggest an algorithm based on a model of light radiation where model parameters can be measured by projecting a structured light pattern onto a scene. The light model assumes the light $L(i, c)$ radiated from a scene point i reaching a camera point c is a combination of a direct component $L_d(i, c)$ and a global component $L_g(i, c)$ such that $L(i, c) = L_d(i, c) + L_g(i, c)$. The direct component is due to direct reflection from the scene point i whereas the global component is due to light reflected from all other points in the scene. By projecting a checkerboard patten of high frequency, half of the scene will be in illuminated checkers and the other half will be in shaded checkers. We denote the degree of illumination as α where $\alpha = 0.5$ for the checkerboard pattern. A scene point in an illuminated checker $L^+(i, c)$ will contain a combination of direct and global light whereas the shaded checkers $L^-(i, c)$ will only contain the global light. Shifting the pattern such that all scene points will be in an illuminated checker in one image and a shaded checker in another enables the measurement of illuminated and shaded elements of the image. Two images is enough to obtain this, but in practice satisfactory results require much smaller shifts between images. From a stack of images with shifted checkerboard patterns we get $L^+(i, c) = L_{\max}(i, c)$ and $L^-(i, c) = L_{\min}(i, c)$ as the maximum and minimum pixel

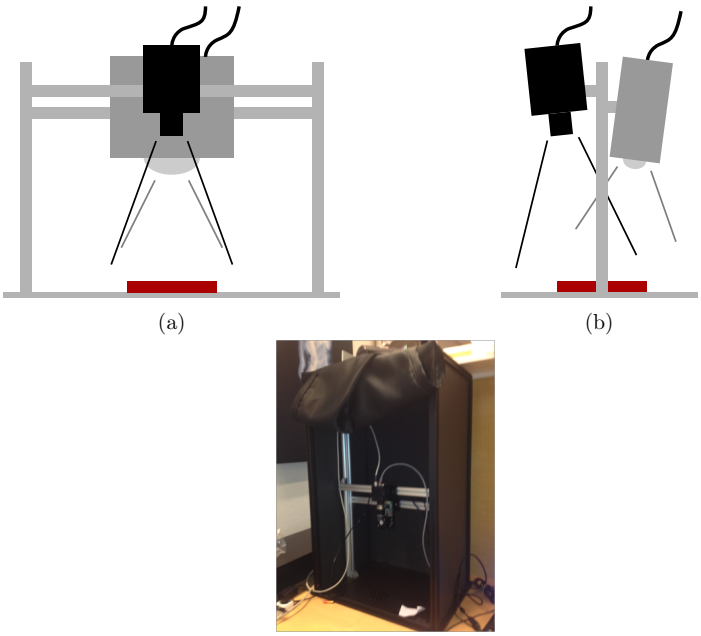

(a) (b)

(c)

Figure 1: Schematic illustration of structured light setup. (a) a camera (black) and a light projector (gray) pointing at a food sample (dark red), (b) the same setup seen from the side. (c) The set-up in it current form.

intensity in the image stack respectively. We obtain

$$L_g(i,c) = \frac{1}{1-\alpha}L^-(i,c) = \frac{1}{2}L^-(i,c) \ , \tag{1}$$

$$L_d(i,c) = L^+(i,c) - \alpha L_g = L^+(i,c) - \frac{1}{2}L_g(i,c) = L^+(i,c) - L^-(i,c) \ . \tag{2}$$

Typically the projector will also emit light in the shaded source elements. If the light contribution in the deactivated source element is b we have

$$L^+(i,c) = L_d(c,i) + \alpha L_g(c,i) + b(1-\alpha)L_g(c,i) \ , \tag{3}$$

$$L^-(i,c) = bL_d(i,c) + (1-\alpha)L_g(c,i) + \alpha b L_g(c,i) \ . \tag{4}$$

Isolating the global and direct components we obtain

$$\begin{aligned} L_g(i,c) &= \left(L^+(i,c) - \frac{1}{b}L^-(i,c)\right)\frac{b}{(b^2-1)(1-\alpha)} \\ &= \left(L^+(i,c) - \frac{1}{b}L^-(i,c)\right)\frac{2b}{b^2-1} \ , \end{aligned} \tag{5}$$

$$\begin{aligned} L_d(i,c) &= L^+(i,c) + \left(\frac{1}{b}L^-(i,c) - L^+(i,c)\right)\frac{b^2(1-\alpha)+b\alpha}{(b^2-1)(1-\alpha)} \\ &= L^+(i,c) + \left(\frac{1}{b}L^-(i,c) - L^+(i,c)\right)\frac{b^2+b}{b^2-1} \ . \end{aligned} \tag{6}$$

Sinusoidal patterns can be used as an alternative to a checkerboard, where only three images are needed in order to separate the direct and global components. We assume that a sinusoidal pattern going from deactivated to fully lit source elements. Using this we measure three illuminations L_1, L_2, and L_3 at scene point i and camera point c with the three unknown parameters being the phase ϕ, the direct component L_d, and the global component L_g.

$$L_1(i,c) = L_d(i,c)\left(\frac{1}{2} + \frac{1}{2}\sin(\phi)\right) + \frac{1}{2}L_g(i,c) \ , \tag{7}$$

$$L_2(i,c) = L_d(i,c)\left(\frac{1}{2} + \frac{1}{2}\sin(\phi + \frac{2}{3}\pi)\right) + \frac{1}{2}L_g(i,c) \ , \tag{8}$$

$$L_3(i,c) = L_d(i,c)\left(\frac{1}{2} + \frac{1}{2}\sin(\phi - \frac{2}{3}\pi)\right) + \frac{1}{2}L_g(i,c) \ . \tag{9}$$

From this we obtain

$$L_1(i,c) + L_2(i,c) + L_3(i,c) = \frac{3}{2}L_d(i,c) + \frac{3}{2}L_g(i,c) \ . \tag{10}$$

Because sine of a sum of two elements is a sum of the product of sine and cosine of the elements we obtain

$$\begin{aligned}
\sin\left(\phi + \frac{3}{2}\pi\right) &= \sin(\phi)\cos\left(\frac{2}{3}\pi\right) + \cos(\phi)\sin\left(\frac{2}{3}\pi\right) && (11)\\
&= \frac{1}{2}\sin(\phi) + \sqrt{\frac{3}{4}}\cos(\phi)\ , && (12)\\
\sin\left(\phi - \frac{3}{2}\pi\right) &= \frac{1}{2}\sin(\phi) - \sqrt{\frac{3}{4}}\cos(\phi)\ . && (13)
\end{aligned}$$

Using this we obtain

$$\begin{aligned}
2L_1(i,c) - L_2(i,c) - L_3(i,c) &= \frac{3}{2}L_d(i,c)\sin(\phi)\ , && (14)\\
L_2(i,c) - L_3(i,c) &= \sqrt{\frac{3}{4}}L_d(i,c)\cos(\phi)\ . && (15)
\end{aligned}$$

Isolating the phase ϕ we get

$$\phi = \arctan\left(\sqrt{\frac{1}{3}}\frac{2L_1(i,c) - L_2(i,c) - L_3(i,c)}{L_2(i,c) - L_3(i,c)}\right)\ . \quad (16)$$

The estimated phase ϕ is in the range $[-\pi/2, \pi/2]$, but in order to account for negative values when estimating the direct component from the difference between L_2 and L_3 we use the absolute value of this difference. Knowing ϕ we obtain the direct and global components as

$$\begin{aligned}
L_d(i,c) &= \frac{1}{\sqrt{3/4}\cos(\phi)}|L_2(i,c) - L_3(i,c)|\ , && (17)\\
L_g(i,c) &= \frac{2}{3}(L_1(i,c) + L_2(i,c) + L_3(i,c)) - L_d(i,c)\ . && (18)
\end{aligned}$$

Precisely recovering L_d and L_g e.g. for artificial illumination requires high frequency patterns. We are however not interested in re-illuminating the depicted objects, but in quantifying quality parameters. In order to measure quality we are interested in quantifying the light interaction with the object, and we obtain an informative characterization by measuring the direct and global components as a function of pattern frequency. Changing the illumination frequencies influences especially the global component as sketched in Figure 2 illustrating the subsurface scattering. Decreasing the source frequency by having larger checkers or lower frequency sine waves increases the minimum length that subsurface scattered photons must travel. In our experimental validation we see a blurring effect in the global component like shown in Figure 3.

Light-sample interactions at a specific scattering distance can be imaged by differenting the global images with respect to scale. When increasing the scale, e.g. by increasing the

size of the checkers in the checkerboard pattern, the subsurface scattered light reaching the center of the unlit checkers, measured as L^-, has on average traveled longer and reached deeper into the sample. The minimum distance that the light has traversed, is from the edge of the illuminated checker to the center of the unlit checker. Subtracting two consecutive global images will depict exactly the light that has traversed a distance from half the checker size in the first image to half the checker size in the other. We estimate the global difference image ΔL_g between scattering distances d_1 and d_2, where $d_1 < d_2$

$$\Delta L_g(i, c, d_1, d_2) = L_g(i, c, d_1) - L_g(i, c, d_2) \ . \tag{19}$$

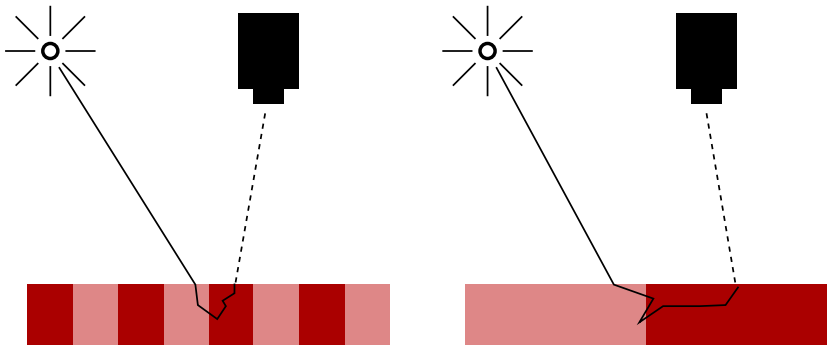

Figure 2: Illustration of the contribution to the global component from subsurface scattering with changing illumination frequencies. (a) shows a high frequency pattern and (b) a low frequency pattern. In the low frequency pattern the average subsurface scattering path becomes longer.

3 Experiments

We have constructed a vision set-up as illustrated in Figure 1 with the camera and projector viewing and illuminating the sample from above. This setup has been used to conduct a number of experiments including the color measurement experiment in [17] based on high frequency illumination patterns. Here we extend this work using multiple scales with decreasing frequency patterns as shown in Figure 3, where a checkerboard pattern is used with checkers of size 4×4, 8×8, 12×12, 16×16, and 20×20 projector pixels respectively. It should be noted that there are some imaging artefacts in the low frequency patterns because we used too few pattern shifts.

Multi-scale projections provides very interesting results for imaging food quality – especially in the global image, because not only surface reflectance is seen but also properties

underneath the surface of depicted food item are revealed. An example of how subsurface patterns become visible is shown in Figure 4.

Difference images are shown in Figure 5, and the difference image between the two smallest checkerboard patters appears similar to the direct image, which is to be expected because this light has only scattered few times. An interesting property of the difference image is that the highly scattering fat parts become apparent in the second image, whereas the red meat colors are visible after more scattering.

In Figure 6 images of salami using sinusoidal patterns are shown, illustrating artefacts by missing camera and projector calibration. In Figure 7 and 8 examples of a carrot and an apple are shown. The direct apple image is overexposed giving imaging artefacts, but still it can be seen that the apple has been bruised, which is seen much more clearly in the direct image compared to the combined image.

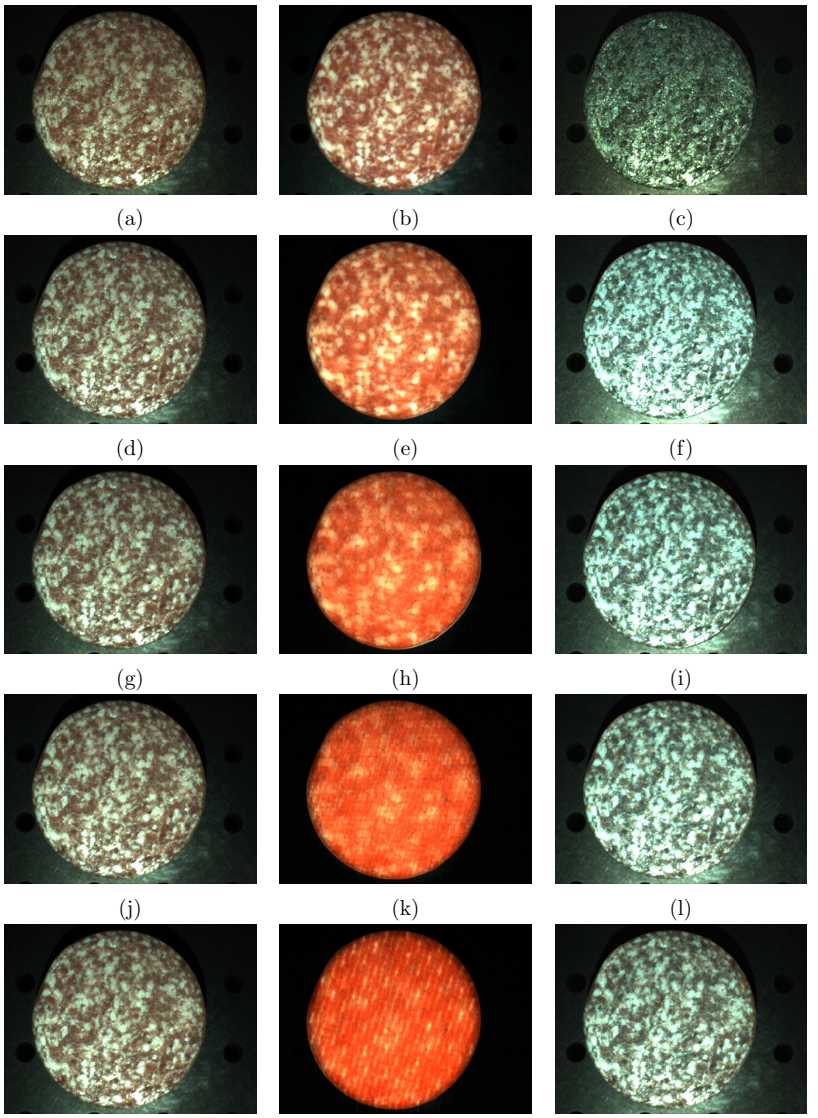

Figure 3: Overview of multi-scale separation of direct and global components of salami slices with increasing scale for each row. Left column is a combination of the direct and global component, middle column is the global component, and right column is the direct component. Images are rescaled for visualization.

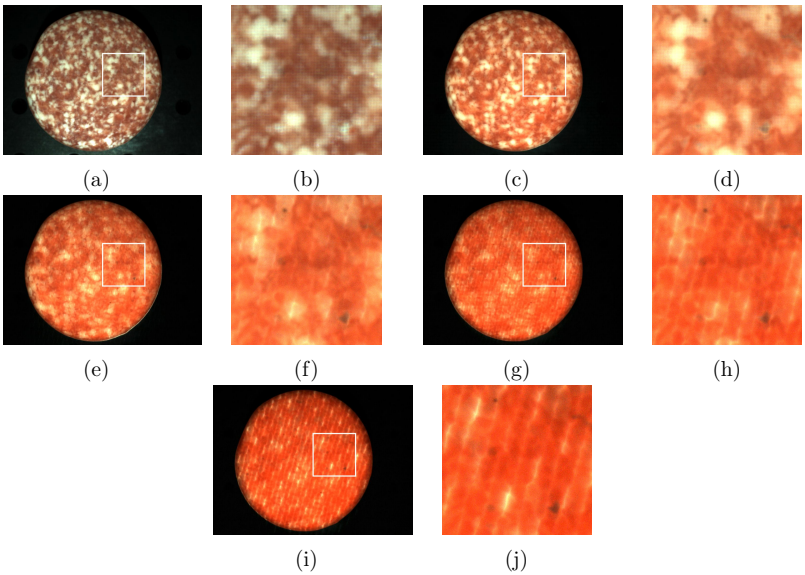

Figure 4: Detail of the global image as a function of pattern frequency. Notice how the dark spots appear with increasing scale where most are not visible in the first image. Furthermore the blurring effect is seen as well as imaging artefacts. Images are rescaled for visualization.

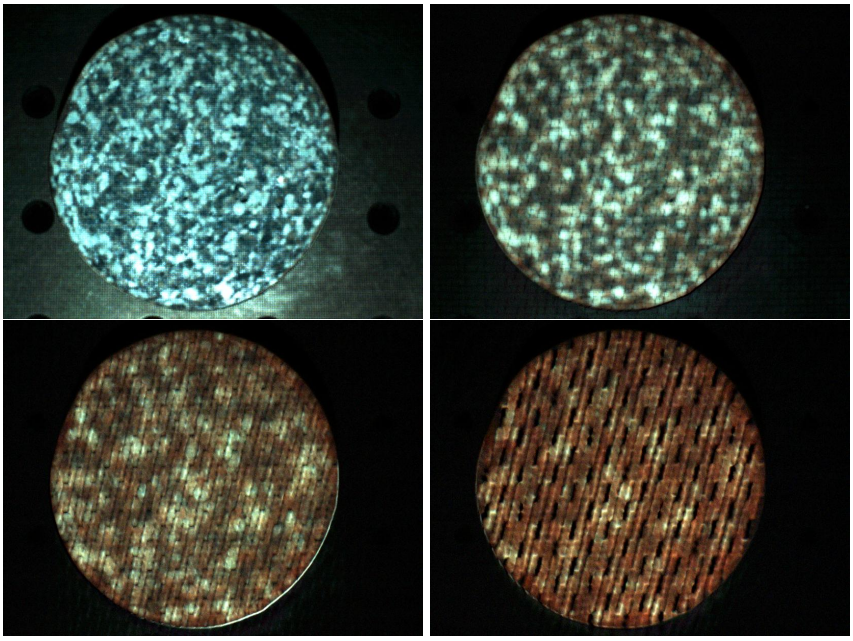

Figure 5: Global difference images obtained as the difference between global illumination images acquired at different scale. Here the imaging artefacts become particularily apparent. Images are rescaled for visualization.

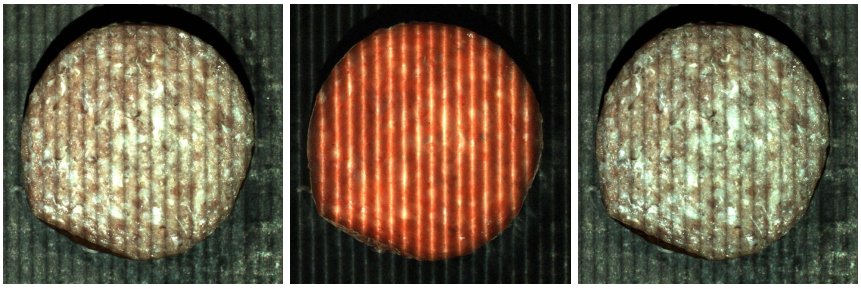

Figure 6: Image of salami using sinusoidal patterns. Left is the combined image, middle the global, and right is the direct component. Images are rescaled for visualization.

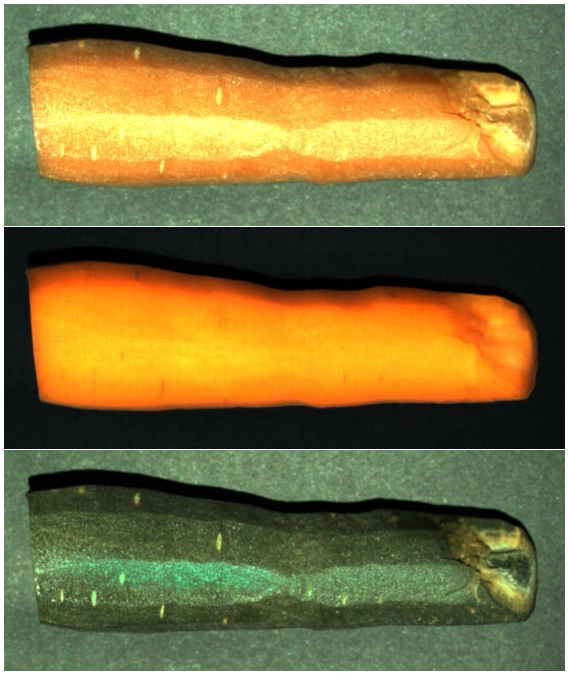

Figure 7: Image of carrot using checkerboard patterns. Left is the combined image, middle the global, and right is the direct component. Images are rescaled for visualization.

Figure 8: Image of carrot using checkerboard patterns. Left is the combined image, middle the global, and right is the direct component. Not how the appear violet in the direct image. Note that the apple has been bruised, which can be seen in the direct images but is almost invisible in the combined image.

4 Discussion and Conclusion

We have demonstrated that the proposed instrumentation and the associated image analysis techniques have great potential for food quality assessment. Using the illumination separation technique described in [12] with our instrumentation showed good results for meat color assessment [17]. Here we show how our multi-scale extension enables detailed analysis of subsurface scattering properties.

Separating the illumination into the global and direct components provides valuable information in visual food analysis due to the scattering properties of such objects. Biological objects have various degrees of translucency, which is revealed in the global illumination component. In our setup the main contribution to the global component is through subsurface scattering, because the simple geometry of the food items that we have considered and because there is only little intra object reflections. Light scattering in food items is closely related to the structural and chemical composition of the food, and by analyzing the scattering properties we will be able obtain information about food quality. This is demonstrated in e.g. [1, 15] using diffuse reflectance for analyzing scattering for food quality inference.

Adding scale to the method enables a more detailed analysis of the scattering properties. Scale is added by decreasing the frequency of the illumination pattern, which mainly affects the global illumination, where the food item is depicted as a function of minimum length that light must travel through the food item. Hereby we obtain scattering information similar to the diffuse reflectance analysis in [1, 15], but here obtained in a full image and not at an illuminated point. It should however be noted that this method requires a much coarser discretization than the diffuse reflectance.

This work is based on physical model for interaction of light and matter, where we focus on obtaining images that are good for quantifying food quality. The physical interpretability of the obtained results is therefore secondary, where we are interested in imaging food quality features, which are good statistical modeling.

Most of our preliminary studies show imaging artefacts, which potentially can corrupt the further analysis and therefore the usage of the system. We believe that these artefacts are caused by either the imaging conditions violating the model assumptions of the imaging model, missing radiometric projector and camera calibration, or too few projection patters.

The model assumptions says that one source element should create a direct component along the line of sight of a single camera pixel, and that the global contribution is a smooth function of the illumination frequency. Mirroring surfaces might violate this assumption especially with intra-object reflections. However, in our setting the geometry is relatively simple and the setup is in a closure surrounded by non-reflective material. So, we expect the model to be sufficiently good.

The projector and camera has not been radiometrically calibrated, so some artefacts will be caused by this. Especially using a sinusoidal projection pattern requires a precise calibration, and such a procedure will be implemented, when developing the instrument

further. Without calibration a vertical stripe pattern will appear as seen in Figure 6.

We believe that the main cause for the artefacts seen in our experiments using the checkerboard pattern is due to not using enough checkers, especially for the large checkers where the most severe artefacts are seen. This results in a repetitive variation of intensities most clearly seen in the global image.

In the future we plan to extend the instrument to include wavelength specific illumination using a multispectral projector. A multispectral projector can be constructed using wavelength specific light emitting diodes. Having a multispectral instrumentation enables an even more detailed analysis of food quality in relation to both structure and chemical composition.

We have demonstrated the principle of multi-scale structured light for separating the global and direct light component. But a range of experiments remains to be conducted, both for instrument optimization and for assessing the quality inspection capabilities of the proposed method. However, given the simplicity of the instrumentation and analysis, and the impressive results obtained despite severe imaging artefacts, we see this system as a valuable addition to vision based instruments for food quality assessment.

5 Acknowledgements

This work has been financed by the Center for Imaging Food Quality, a project funded by the Danish Council for Strategic Research (contract no 09-067039) within the Program Commission on Health, Food and Welfare.

References

[1] Otto Højager Attermann Abildgaard, Anders Bjorholm Dahl, and Rasmus Larsen. *Broadband optical characterization of material properties.* PhD thesis, 2014.

[2] Alessandro Artusi, Francesco Banterle, and Dmitry Chetverikov. A survey of specularity removal methods. In *Computer Graphics Forum*, volume 30, pages 2208–2230. Wiley Online Library, 2011.

[3] M Buendía, R Salvador, R Cibrian, M Laguia, and JM Sotoca. Determination of the object surface function by structured light: application to the study of spinal deformities. *Physics in medicine and biology*, 44(1):75, 1999.

[4] Hansjoerg Gaertner, Jean-François Lavoie, Eric Vermette, and Pascal-Simon Houle. Multiple structured light system for the 3d measurement of feet. In *Electronic Imaging'99*, pages 104–114. International Society for Optics and Photonics, 1999.

[5] Larry J Hornbeck. Digital light processing for high-brightness high-resolution applications. In *Electronic Imaging'97*, pages 27–40. International Society for Optics and Photonics, 1997.

[6] Bruce Lamond, Pieter Peers, and Paul Debevec. Fast image-based separation of diffuse and specular reflections. In *ACM SIGGRAPH 2007 sketches*, page 74. ACM, 2007.

[7] Bruce Lamond, Pieter Peers, Abhijeet Ghosh, and Paul Debevec. Image-based separation of diffuse and specular reflections using environmental structured illumination. In *Computational Photography (ICCP), 2009 IEEE International Conference on*, pages 1–8. IEEE, 2009.

[8] Ashley M Laughney, Venkataramanan Krishnaswamy, Tyler B Rice, David J Cuccia, Richard J Barth, Bruce J Tromberg, Keith D Paulsen, Brian W Pogue, and Wendy A Wells. System analysis of spatial frequency domain imaging for quantitative mapping of surgically resected breast tissues. *Journal of biomedical optics*, 18(3):036012–036012, 2013.

[9] Alexander J Lin, Maya A Koike, Kim N Green, Jae G Kim, Amaan Mazhar, Tyler B Rice, Frank M LaFerla, and Bruce J Tromberg. Spatial frequency domain imaging of intrinsic optical property contrast in a mouse model of alzheimers disease. *Annals of biomedical engineering*, 39(4):1349–1357, 2011.

[10] Alexander J Lin, Adrien Ponticorvo, Soren D Konecky, Haotian Cui, Tyler B Rice, Bernard Choi, Anthony J Durkin, and Bruce J Tromberg. Visible spatial frequency domain imaging with a digital light microprojector. *Journal of biomedical optics*, 18 (9):096007–096007, 2013.

[11] Amaan Mazhar, Steven Dell, David J Cuccia, Sylvain Gioux, Anthony J Durkin, John V Frangioni, and Bruce J Tromberg. Wavelength optimization for rapid chromophore mapping using spatial frequency domain imaging. *Journal of biomedical optics*, 15(6):061716–061716, 2010.

[12] Shree K Nayar, Gurunandan Krishnan, Michael D Grossberg, and Ramesh Raskar. Fast separation of direct and global components of a scene using high frequency illumination. In *ACM Transactions on Graphics (TOG)*, volume 25, pages 935–944. ACM, 2006.

[13] David W Penman. Determination of stem and calyx location on apples using automatic visual inspection. *Computers and electronics in agriculture*, 33:7–18, 2001.

[14] Darren Roblyer, Thomas D OSullivan, Robert V. Warren, and Bruce J Tromberg. Feasibility of direct digital sampling for diffuse optical frequency domain spectroscopy in tissue. *Measurement Science and Technology*, 24(4):045501, 2013.

[15] Jacob Lercke Skytte, Rasmus Larsen, and Anders Bjorholm Dahl. *2D Static Light Scattering for Dairy Based Applications.* PhD thesis, 2014.

[16] Da-Wen Sun. *Computer vision technology for food quality evaluation.* Academic Press, 2011.

[17] Camilla H. Trinderup and Yuan Brad Kim. Fresh meat color evaluation using a structured light imaging system. *Submitted*, 2014.

[18] Di Wu and Da-Wen Sun. Colour measurements by computer vision for food quality control–a review. *Trends in Food Science & Technology*, 29(1):5–20, 2013.

[19] Qingsheng Yang. Apple stem and calyx identification with machine vision. *Journal of agricultural engineering Research*, 63(3):229–236, 1996.

Bibliography

Adams, J. B., Smith, M. O., and Johnson, P. E. (1986). Spectral mixture modeling: A new analysis of rock and soil types at the viking lander 1 site. *Journal of Geophysical Research: Solid Earth (1978–2012)*, 91(B8):8098–8112.

Aluwé, M., Millet, S., Nijs, G., Tuyttens, F., Verheyden, K., Brabander, H. D., Brabander, D. D., and Oeckel, M. V. (2009). Absence of an effect of dietary fibre or clinoptilolite on boar taint in entire male pigs fed practical diets. *Meat Science*, 82(3):346–352.

Artusi, A., Banterle, F., and Chetverikov, D. (2011). A survey of specularity removal methods. In *Computer Graphics Forum*, volume 30, pages 2208–2230. Wiley Online Library.

Babol, J. and Squires, E. J. (1995). Quality of meat from entire male pigs. *Food research international*, 28(3):201–212.

Banon, S., Costa, E., Gil, M., and Garrido, M. (2003). A comparative study of boar taint in cooked and dry-cured meat. *Meat science*, 63(3):381–388.

Belongie, S., Carson, C., Greenspan, H., and Malik, J. (1998). Color-and texture-based image segmentation using em and its application to content-based image retrieval. In *Computer Vision, 1998. Sixth International Conference on*, pages 675–682. IEEE.

Ben-Dor, E., Chabrillat, S., Demattê, J., Taylor, G., Hill, J., Whiting, M., and Sommer, S. (2009). Using imaging spectroscopy to study soil properties. *Remote Sensing of Environment*, 113:S38–S55.

Bonneau, M., Denmat, M. L., Vaudelet, J., Nunes, J. V., Mortensen, A., and Mortensen, H. (1992). Contributions of fat androstenone and skatole to boar taint: Ii. eating quality of cooked hams. *Livestock Production Science*, 32(1):81 – 88.

Breiman, L. (2001). Random forests. *Machine learning*, 45(1):5–32.

Brosnan, T. and Sun, D. (2004). Improving quality inspection of food products by computer vision – a review. *Journal of Food Engineering*, 61(1):3–16.

Burges, C. J. (1998). A tutorial on support vector machines for pattern recognition. *Data mining and knowledge discovery*, 2(2):121–167.

Dahl, A. and Larsen, R. (2011). Learning dictionaries of discriminative image patches. In *Proceedings of the British Machine Vision Conference*. BMVA.

Dalal, N. and Triggs, B. (2005). Histograms of oriented gradients for human detection. In *Computer Vision and Pattern Recognition, 2005. CVPR 2005. IEEE Computer Society Conference on*, volume 1, pages 886–893. IEEE.

Dissing, B. S., Papadopoulou, O. S., Tassou, C., Ersbøll, B. K., Carstensen, J. M., Panagou, E. Z., and Nychas, G.-J. (2013). Using multispectral imaging for spoilage detection of pork meat. *Food and Bioprocess Technology*, 6(9):2268–2279.

Easton, R. L. (2010). *Fourier Methods in Imaging*. John Wiley and Sons.

Elden, L., Wittmeyer-Koch, L., and Bruun Nielsen, H. (2004). *Introduction to numerical computation - analysis and MATLAB illustrations*. Studentlitteratur.

Ersbøll, B. K. and Conradsen, K. (2012). *Multivariate Statistics - An Introduction 8. ed.* DTU Informatics.

European commission (2011). Farming of pigs. european declaration on alternatives to surgical castration of pigs. `http://ec.europa.eu/food/animal/welfare/farm/initiatives_en.htm`. Accessed: 2014-12-18.

Ferman, A. M., Tekalp, A. M., and Mehrotra, R. (2002). Robust color histogram descriptors for video segment retrieval and identification. *Image Processing, IEEE Transactions on*, 11(5):497–508.

Finlayson, G. D. and Drew, M. S. (1997). Constrained least-squares regression in color spaces. *Journal of Electronic Imaging*, 6(4):484–493.

Galwey, N. W. (2007). *Introduction to Mixed Modelling: Beyond Regression and Analysis of Variance*. John Wiley and Sons, Ltd.

Garcia-Regueiro, J. and Diaz, I. (1989). Evaluation of the contribution of skatole, indole, androstenone and androstenols to boar-taint in back fat of pigs by hplc and capillary gas chromatography (cgc). *Meat Science*, 25(4):307–316.

Girolami, A., Napolitano, F., Faraone, D., and Braghieri, A. (2013). Measurement of Meat Color Using a Computer Vision System. *Meat Science*, 93(1):111 – 118.

Goodman, J. W. (1975). Statistical properties of laser speckle patterns. In *Laser speckle and related phenomena*, pages 9–75. Springer.

Gowen, A., ODonnell, C., Cullen, P., and Bell, S. (2008). Recent applications of chemical imaging to pharmaceutical process monitoring and quality control. *European Journal of Pharmaceutics and Biopharmaceutics*, 69(1):10 – 22.

Hansen, L. L., Mejer, H., Thamsborg, S. M., Byrne, D. V., Roepstorff, A., Karlsson, A. H., and Hansen-Møller, J. (2006a). Influence of chicory roots (chicorium intybus l) on boar taint in entire male and female pigs. *Animal Science*, 82:359 – 368.

Hansen, P. C., Nagy, J. G., and O'Leary, D. P. (2006b). *Deblurring images : Matrices, spectra, and filtering*. SIAM.

Haralick, R. M. (1979). Statistical and structural approaches to texture. *Proceedings of the IEEE*, 67(5):786–804.

Hardeberg, J. (2001). *Acquisition and Reproduction of Color Images: Colorimetric and Multispectral Approaches*. Universal-Publishers.

Hastie, T., Tibshirani, R., and Friedman, J. (2009). *The elements of statistical learning : Data mining, inference, and prediction*. Springer.

Hunt, M., Acton, J., Benedict, R., Calkins, C., Cornforth, D., Jeremiah, L., Olson, D., Salm, C., Savell, J., and Shivas, S. (1991). Guidelines for Meat Color Evaluation. In *44th Annual Reciprocal Meat Conference*, pages 9–12.

ISO 11664 - 1 (2007). ISO 11664 - 1: 2007(E)/CIE S 014-1/E: 2006: Joint ISO/CIE Standard: Colorimetry - Part 1: CIE Standard Colorimetric Observers.

ISO 11664 - 2 (1976). IISO 11664-2:2007(E)/CIE S 014-2/E:2006: Joint ISO/CIE Standard: Colorimetry Part 2: CIE Standard Illuminants for Colorimetry.

ISO 11664 - 3 (1976). ISO 11664-3:2012(E)/CIE S 014-3/E:2011: Joint ISO/CIE Standard: Colorimetry Part 3: CIE Tristimulus Values.

ISO/CIE Standard (1976). ISO 11664-4:2008(E)/CIE S 014-4/E:2007: Joint ISO/CIE Standard: Colorimetry - Part 4: CIE 1976 L*a*b* Colour Space.

Johnson, R. A. and Wichern, D. W. (2002). *Applied multivariate statistical analysis*. Pearson Education.

Kim, Y. H., Keeton, J. T., Smith, S., Berghman, L. R., and Savell, J. W. (2009). Role of lactate dehydrogenase in metmyoglobin reduction and color stability of different bovine muscles. *Meat science*, 83(3):376–382.

Landbrug & Fødevarer (2012). Økonomisk analyse – dansk landbrugs- og fødevareeksport. Online `www.lf.dk`. Accessed: 2014-12-17.

Larraín, R., Schaefer, D., and Reed, J. (2008). Use of Digital Images to Estimate CIE Color Coordinates of Beef. *Food Research International*, 41(4):380–385.

Lasarte, M., Vilaseca, M., Pujol, J., and Arjona, M. (2006). Color Measurements with Colorimetric and Multispectral Imaging Systems. In *Proc. SPIE*, volume 6062, pages 0F1–0F11.

Lawrie, R. (1998). Lawrie's meat science, 1998. *Cambridge, England: Woodhead Ltd.*

Leistner, L. (1995). Stable and safe fermented sausages world-wide. In *Fermented meats*, pages 160–175. Springer.

León, K., Mery, D., Pedreschi, F., and León, J. (2006). Color Measurement in L*a*b* Units from RGB Digital Images. *Food Research International*, 39(10):1084 – 1091.

Leroy, F. and De Vuyst, L. (2004). Lactic acid bacteria as functional starter cultures for the food fermentation industry. *Trends in Food Science & Technology*, 15(2):67–78.

Leroy, F., Verluyten, J., and De Vuyst, L. (2006). Functional meat starter cultures for improved sausage fermentation. *International journal of food microbiology*, 106(3):270–285.

Liou, F. W. (2007). *Rapid prototyping and engineering applications : a toolbox for prototype development*. CRC Press.

Ljungqvist, M. G., Ersbøll, B. K., Nielsen, M. E., and Frosch, S. (2012). Multispectral image analysis for astaxanthin coating classification. *Journal of Imaging Science and Technology*, 56(2).

Lowe, D. (2004). Distinctive image features from scale-invariant keypoints. *International Journal of Computer Vision*, 60(2):91–110.

LYNCH, N. M., KASTNER, C. L., and KROPF, D. H. (1986). Consumer acceptance of vacuum packaged ground beef as influenced by product color and educational materials. *Journal of Food Science*, 51(2):253–255.

Ma, H. and Anderson, C. A. (2008). Characterization of pharmaceutical powder blends by nir chemical imaging. *Journal of pharmaceutical sciences*, 97(8):3305–3320.

MacDougall, D. and Hutchings, J. (2002). *Colour in Food - Improving Quality*. Woodhead Publishing.

Martelli, F. (2010). *Light propagation through biological tissue and other diffusive media : theory, solutions, and software*. SPIE.

Mendoza, F., Dejmek, P., and Aguilera, J. (2006). Calibrated Color Measurements of Agricultural Foods Using Image Analysis. *Postharvest Biology and Technology*, 41(3):285 – 295.

Nayar, S. K., Krishnan, G., Grossberg, M. D., and Raskar, R. (2006). Fast separation of direct and global components of a scene using high frequency illumination. In *ACM Transactions on Graphics (TOG)*, volume 25, pages 935–944. ACM.

Nielsen, O. H. A. (2014). *Broadband optical characterization of material properties*. PhD thesis.

Olesen, M. H., Carstensen, J. M., and Boelt, B. (2011). Multispectral imaging as a potential tool for seed health testing of spinach (spinacia oleracea l.). *Seed Science and Technology*, 39(1):140–150.

O'Sullivan, M., Byrne, D., Martens, H., Gidskehaug, L., Andersen, H., and Martens, M. (2003). Evaluation of Pork Colour: Prediction of Visual Sensory Quality of Meat from Instrumental and Computer Vision Methods of Colour Analysis. *Meat science*, 65(2):909–918.

Pal, N. R. and Pal, S. K. (1993). A review on image segmentation techniques. *Pattern recognition*, 26(9):1277–1294.

Piederriere, Y., Le Meur, J., Cariou, J., Abgrall, J. F., and Blouch, M. T. (2004). Particle aggregation monitoring by speckle size measurement; application to blood platelets aggregation. *Optics Express, Opt. Express*, 12(19):4596–4601.

Sharifzadeh, S., Skytte, J. L., Clemmensen, L. K. H., and Ersbøll, B. K. (2013). Dct-based characterization of milk products using diffuse reflectance images. *2013 18th International Conference on Digital Signal Processing (dsp)*, page 6622669.

Skytte, J., Andersen, U., ller, F. M., Nielsen, O., Carstensen, J., Dahl, A., and Larsen, R. (2012). *Monitoring structure development in milk acidification using diffuse reflectance profiles.* University of Copenhagen.

Skytte, J. L. (2014). *2D Static Light Scattering for Dairy Based Applications.* PhD thesis, Technical University of Denmark.

Swatland, H. (2002). Refractometry of pork muscle and beef connective and adipose tissue. *Meat science*, 62(2):225–228.

Swatland, H. (2004). Progress in understanding the paleness of meat with a low ph: keynote address. *South African Journal of Animal Science*, 34(6):1–7.

Tariq, S., Gardner, A., Llamas, I., Jones, A., Debevec, P., Turk, G., and Corporation, N. (2006). Efficient estimation of spatially varying subsurface scattering parameters. *Vision, Modeling, and Visualization (VMV2006)*, pages 129–136.

Valous, N. A., Mendoza, F., Sun, D.-W., and Allen, P. (2009). Colour calibration of a laboratory computer vision system for quality evaluation of pre-sliced hams. *Meat science*, 81(1):132–141.

van Kleef, E., van Trijp, H., and Luning, P. (2005). Consumer research in the early stages of new product development: a critical review of methods and techniques. *FOOD QUALITY AND PREFERENCE*, 16(3):181–201.

Weiler, U., Font i Furnols, M., Fischer, K., Kemmer, H., Oliver, M., Gispert, M., Dobrowolski, A., and Claus, R. (2000). Influence of differences in sensitivity of spanish and german consumers to perceive androstenone on the acceptance of boar meat differing in skatole and androstenone concentrations. *Meat science*, 54(3):297–304.

Wu, D. and Sun, D. (2013). Colour Measurements by Computer Vision for Food Quality Control - A Review. *Trends in Food Science and Technology*, 29(1):5 – 20.

Yagiz, Y., Balaban, M., Kristinsson, H., Welt, B., and Marshall, M. (2009). Comparison of Minolta Colorimeter and Machine Vision System in Measuring Colour of Irradiated Atlantic Salmon. *Journal of the Science of Food and Agriculture*, 89(4):728–730.

Yancey, J. and Kropf, D. (2008). Instrumental reflectance values of fresh pork are dependant on aperture size. *Meat science*, 79(4):734–739.

Zammerini, D., Wood, J., Whittington, F., Nute, G., Hughes, S., Hazzledine, M., and Matthews, K. (2012). Effect of dietary chicory on boar taint. *Meat Science*, 91(4):396–401.

Zou, H., Hastie, T., and Tibshirani, R. (2006). Sparse principal component analysis. *Journal of computational and graphical statistics*, 15(2):265–286.